WARWICK
THE UNIVERSITY OF WARWICK

**A Thesis Submitted for the Degree of PhD at the University of Warwick**

**Permanent WRAP URL:**
http://wrap.warwick.ac.uk/102453/

**Copyright and reuse:**
This thesis is made available online and is protected by original copyright.
Please scroll down to view the document itself.
Please refer to the repository record for this item for information to help you to cite it.
Our policy information is available from the repository home page.

For more information, please contact the WRAP Team at: wrap@warwick.ac.uk

**warwick.ac.uk/lib-publications**

THE UNIVERSITY OF WARWICK

# *Morphological Control in the Solution Crystallisation of Polymeric Nanoparticles*

Maria Inam

*Submitted for the degree of Doctor of Philosophy*

Department of Chemistry

January 2018

***For my Amijee and Abujee***

# *Table of Contents*

**Acknowledgements** ..... XIII

**Declaration of Authorship** ..... XV

**List of Publications** ..... XVI

**Summary** ..... XVIII

**Abbreviations** ..... XIX

**List of Figures** ..... XXVII

**List of Schemes** ..... LIV

**List of Tables** ..... LVIII

**Chapter One – Introduction to polymers, nanoparticles and morphology control** ..... 1

1.1 Morphology in nature ..... 2

1.2 Synthetic polymer building blocks ..... 3

  1.2.1 Free radical polymerisation ..... 4

  1.2.2 Living polymerisation ..... 6

  1.2.3 Reversible-deactivation radical polymerisation ..... 6

    1.2.3.1 Persistent radical effect ..... 7

    1.2.3.2 Degenerative transfer ..... 8

    1.2.3.3 End group modification of RAFT polymers ..... 12

  1.2.4 Ring-opening polymerisation ..... 14

1.2.4.1 Poly(L-lactide) .... 14

1.2.4.2 Poly(ε-caprolactone) .... 16

1.3 Solution self-assembly of amphiphilic block copolymers .... 17

1.3.1 Particle morphology .... 17

1.3.2 Particle self-assembly methods .... 19

1.4 Crystallisation-driven self-assembly .... 21

1.4.1 Polymer crystallisation .... 21

1.4.2 Chain-folding of crystalline-core micelles .... 22

1.4.3 Mechanisms for solution crystallisation of diblock copolymers .... 22

1.4.3.1 Self-nucleation/thermal crystallisation .... 23

1.4.3.2 Living crystallisation .... 24

1.4.3.3 Self-seeding .... 25

1.4.3.4 Morphological transitions .... 27

1.4.4 Observable features of polymer crystals .... 28

1.4.4.1 Polymer crystal habit .... 28

1.4.4.2 Multilayer crystals .... 28

1.4.4.3 Edge and screw dislocations .... 29

1.5 Analysis of nanoparticles .... 31

1.5.1 Transmission electron microscopy .... 32

1.5.2 Atomic force microscopy .... 34

1.5.3 Scattering techniques .... 36

1.5.4 Zeta potential .... 36

1.6 Summary ........ 39

1.7 References ........ 40

## Chapter Two – 1D vs. 2D shape selectivity in the crystallisation-driven self-assembly of poly(L-lactide) block copolymers ........ 48

2.1 Abstract ........ 49

2.2 Introduction ........ 50

  2.2.1 Two-dimensional nanomaterials ........ 50

  2.2.2 Crystallisation-driven self-assembly ........ 50

  2.2.3 Crystallisation-driven self-assembly of poly(L-lactide) ........ 53

  2.2.4 Applications of crystalline nanomaterials ........ 54

  2.2.5 Use of a partition co-efficient ........ 55

2.3 Results and Discussion ........ 57

  2.3.1 Synthesis of a pro-cationic monomer, tert-butyl (2-acrylamido ethyl) carbamate (AEANBoc) ........ 57

  2.3.2 Synthesis and crystallisation-driven self-assembly of PLLA-b-PAEA 59

  2.3.3 Crystallisation-driven self-assembly of PLLA$_{36}$-b-PAEA$_{295}$ ........ 66

  2.3.4 Synthesis of PLLA-b-PDMA block copolymers ........ 73

  2.3.5 Directing self-assembly conditions of PLLA-b-PDMA block copolymers using LogP$_{oct}$ analysis ........ 77

  2.3.6 Exploring the self-assembly conditions of PLLA-b-PDMA block copolymers ........ 79

2.3.7 Understanding the assembly process of PLLA-containing diblock copolymers ... 83

2.3.8 Exploring the versatility of the assembly process with block copolymer blending ... 87

2.3.9 Investigation into different sizes of PLLA-b-PDMA platelets ... 89

2.4 Conclusions ... 92

2.5 Experimental ... 94

2.5.1 Materials ... 94

2.5.2 Instrumentation ... 94

2.5.3 Synthesis of N-Boc-ethylenediamine ... 98

2.5.4 Synthesis of pro-cationic monomer tert-butyl (2-acrylamidoethyl) carbamate (AEANBoc) ... 98

2.5.5 Synthesis of dual-headed ROP initiator and chain transfer agent dodecyl 4-(hydroxymethyl) benzyl carbonotrithioate ... 99

2.5.6 Synthesis of poly(L-lactide)$_{36}$ ... 101

2.5.7 Synthesis of poly(L-lactide)$_{36}$-b-poly(tert-butyl (2-acrylamido ethyl) carbamate)$_{295}$ ... 102

2.5.8 Synthesis of poly(L-lactide)$_{36}$-b-poly(acrylamidoethylamine)$_{295}$ ... 102

2.5.9 Typical self-assembly method of poly(l-lactide)$_{36}$-b-poly(acrylamidoethylamine)$_{295}$ spherical micelles ... 103

2.5.10 Typical crystallisation-driven self-assembly of poly(L-lactide)$_{36}$-b-poly(acrylamidoethylamine)$_{295}$ ... 103

2.5.11 Typical crystallisation-driven self-assembly of poly(L-lactide)$_{36}$-b-poly(acrylamidoethylamine)$_{295}$ in alcoholic solvents .................................... 103

2.5.12 Synthesis of poly(L-lactide)$_{48}$-b-poly(N,N-dimethylacrylamide)$_{150}$ 104

2.5.13 Typical crystallisation-driven self-assembly method for poly(L-lactide)$_{48}$-b-poly(N,N-dimethylacrylamide)$_{m}$ block copolymers .................. 104

2.5.14 Synthesis of tert-butoxy-terminated poly(L-lactide)$_{36}$-b-poly(N,N-dimethylacrylamide)$_{245}$ .................................... 104

2.5.15 Synthesis of carboxylic acid-terminated poly(L-lactide)$_{36}$-b-poly(N,N-dimethylacrylamide)$_{245}$ .................................... 105

2.5.16 Synthesis of amine-terminated poly(L-lactide)$_{48}$-b-poly(N,N-dimethylacrylamide)$_{150}$ .................................... 105

2.6 Acknowledgements .................................... 107

2.7 References .................................... 108

**Chapter Three – Enhancing hydrogel properties with controlled nanoparticle shape .................................... 114**

3.1 Abstract .................................... 115

3.2 Introduction .................................... 116

3.2.1 Hydrogels as biomaterials .................................... 116

3.2.2 Polymer-composite hydrogels .................................... 118

3.2.3 Nanoparticle-composite hydrogels .................................... 119

3.2.4 Adhesion of hydrogels ........ 121

3.2.5 Effect of nanocomposite morphology ........ 122

3.3 Results and Discussion ........ 124

3.3.1 Synthesis of poly(L-lactide)-b-poly(N,N-dimethylaminoethyl methacrylate) block copolymers ........ 124

3.3.2 Self-assembly of poly(L-lactide)-b-poly(dimethylaminoethyl methacrylate) block copolymers to obtain spherical particles ........ 130

3.3.3 Initial crystallisation-driven self-assembly of poly(L-lactide)-b-poly(N,N-dimethylaminoethyl methacrylate) block copolymers ........ 132

3.3.4 Crystallisation-driven self-assembly of poly(L-lactide)-b-poly(N,N-dimethylaminoethyl methacrylate) block copolymers in alcohols ........ 134

3.3.5 Formation of PLLA-b-PDMAEMA platelet particles ........ 136

3.3.6 Synthesis and crystallisation-driven self-assembly of PLLA-b-PAA block copolymers for cylindrical particles ........ 139

3.3.7 Modification of PLLA-b-PAA cylindrical micelles by amidation with a DMAEMA mimic ........ 144

3.3.8 Particles for nanocomposite hydrogels ........ 147

3.3.9 Preparation of calcium alginate hydrogels ........ 148

3.3.10 Preparation of calcium alginate hydrogels with PLLA-b-PAA ........ 152

3.3.11 Preparation of calcium alginate hydrogels with PLLA-b-PAEA ........ 160

3.3.12 Preparation of calcium alginate hydrogels with PLLA-b-DMAEMA particles of different morphologies ........ 164

3.3.13 Adhesion of calcium alginate hydrogels with PLLA-b-PDMAEMA particles of different morphologies ........ 173

3.4 Conclusions ........ 176

3.5 Experimental ........ 177

3.5.1 Materials ........ 177

3.5.2 Instrumentation ........ 177

3.5.3 Synthesis of poly(L-lactide)$_{36}$ using an ethyl-terminated chain transfer agent 181

3.5.4 Synthesis of poly(L-lactide)$_{36}$-b-poly(N,N-dimethylaminoethyl methacrylate)$_{216}$ ........ 181

3.5.5 Typical self-assembly method of poly(L-lactide)$_{36}$-b- poly(N,N-dimethylaminoethyl methacrylate)$_{216}$ spherical micelles ........ 182

3.5.6 Typical crystallisation-driven self-assembly of poly(L-lactide)$_{36}$-b-poly(N,N-dimethylaminoethyl methacrylate)$_{216}$ ........ 182

3.5.7 Typical crystallisation-driven self-assembly of poly(L-lactide)$_{36}$-b-poly(N,N-dimethylaminoethyl methacrylate)$_{216}$ in alcoholic solvents ........ 183

3.5.8 Synthesis of poly(L-lactide)$_{36}$ ........ 183

3.5.9 Synthesis of poly(L-lactide)$_{36}$-b-poly(tetrahydropyran acrylate)$_{400}$ ... 183

3.5.10 Typical preparation of poly(L-lactide)$_{36}$-b-poly(acrylic acid)$_{400}$ cylindrical micelles ........ 184

3.5.11 Typical self-assembly method of poly(L-lactide)$_{36}$-b- poly(acrylic acid)$_{400}$ spherical micelles ........ 184

3.5.12 Modification of poly(L-lactide)$_{36}$-b-poly(acrylic acid)$_{400}$ with a DMAEMA mimic ........ 184

3.5.13 Nanocomposite calcium alginate gel formation ........ 185

3.5.14 Calcium alginate gel adhesion with nanoparticles ........ 185

3.6 Acknowledgements ........ 186

3.7 References ........ 187

**Chapter Four – Controlling the size of 2D polymer platelets for water-in-water emulsifiers ........ 193**

4.1 Abstract ........ 194

4.2 Introduction ........ 195

4.2.1 Pickering emulsions ........ 195

4.2.2 Water-in-water emulsions ........ 195

4.2.3 Control of particle size and morphology ........ 197

4.2.4 Two-dimensional platelets as emulsifiers ........ 198

4.3 Results and Discussion ........ 200

4.3.1 Investigation into size control of PLLA-b-PDMAEMA platelets ........ 200

4.3.2 Investigation of PLLA block length for size control of platelets ........ 203

4.3.3 Investigation of PDMAEMA block length for size control of polymer platelets ........ 209

4.3.4 Size control of polymer platelets with crystallisation-driven self-assembly ........ 217

4.3.5 Effect of polymer platelet size on water-in-water Pickering emulsion stability ........ 221

4.3.6 Understanding the effect of polymer platelet size on water-in-water Pickering emulsion stability ........ 228

4.3.7 Effect of surface chemistry on water-in-water Pickering emulsion stability ........ 232

4.3.8 Understanding the effect of surface chemistry on water-in-water Pickering emulsion stability ........ 238

4.4 Conclusions ........ 244

4.5 Experimental ........ 245

4.5.1 Materials ........ 245

4.5.2 Instrumentation ........ 245

4.5.3 Synthesis of poly(L-lactide)$_{36}$ ........ 249

4.5.4 Example synthesis of poly(L-lactide)$_{36}$-b-poly(N,N-dimethylaminoethyl methacrylate)$_{216}$ ........ 249

4.5.5 Synthesis of poly(L-lactide)$_{90}$ ........ 250

4.5.6 Synthesis of poly(L-lactide)$_{90}$-b-poly(N,N-dimethylaminoethyl methacrylate)$_{300}$ ........ 250

4.5.7 Typical preparation of poly(L-lactide)-b-poly(N,N-dimethylaminoethyl methacrylate) spherical micelles ........ 251

4.5.8 Typical preparation of poly(L-lactide)-b-poly(N,N-dimethylaminoethyl methacrylate) platelets ........ 251

4.5.9 Preparation of Pickering emulsions ........ 252

4.5.10 Measurement and calculation of interfacial tension ....................... 252

4.5.11 Zwitterionic modification of poly(L-lactide)$_{36}$-b-poly(N,N-dimethylaminoethyl methacrylate)$_{216}$ platelets ............................................ 255

4.5.12 Quaternisation of poly(L-lactide)$_{36}$-b-poly(N,N-dimethylaminoethyl methacrylate)$_{216}$ platelets ................................................................ 256

4.5.13 Preparation of RAFT end group removed poly(L-lactide)$_{36}$-b-poly(N,N-dimethylaminoethyl methacrylate)$_{216}$........................................... 256

4.6 Acknowledgements......................................................................... 258

4.7 References...................................................................................... 259

**Chapter Five – Precision epitaxy for aqueous 1D and 2D poly(ε-caprolactone) assemblies.................................................................................................. 264**

5.1 Abstract........................................................................................... 265

5.2 Introduction..................................................................................... 266

5.2.1 Biological importance of particle morphology ................................ 266

5.2.2 Morphological and dimensional control of hierarchical assemblies via living growth......................................................................................... 267

5.2.3 Size-controlled assemblies in aqueous media .................................. 268

5.2.4 Size-controlled assemblies with biocompatible polymers ................ 270

5.3 Results and discussion ..................................................................... 272

5.3.1 Synthesis of PCL$_{50}$-b-PDMA$_{180}$ ....................................................... 272

5.3.2 Crystallisation-driven self-assembly of PCL$_{50}$-b-PDMA$_{180}$ .............. 278

5.3.3 Epitaxial growth of $PCL_{50}$-b-$PDMA_{180}$ cylindrical micelles ............. 284

5.3.4 End group modification of $PCL_{50}$-b-$PDMA_{180}$ ................................. 288

5.3.5 Synthesis of $PCL_{50}$-b-$PMMA_{20}$-b-$PDMA_{180}$ .................................... 290

5.3.6 Crystallisation-driven self-assembly of $PCL_{50}$-b-$PMMA_{20}$-b-$PDMA_{180}$ to form cylindrical micelles ........................................................................ 293

5.3.7 Hydrogels from epitaxial growth of $PCL_{50}$-b-$PMMA_{20}$-b-$PDMA_{180}$ cylindrical micelles ........................................................................ 298

5.3.8 Synthesis of $PCL_{50}$-b-$PDMAEMA_{170}$ ............................................... 302

5.3.9 Crystallisation-driven self-assembly of $PCL_{50}$-b-$PDMAEMA_{170}$ ..... 305

5.3.10 Hierarchical structures using PCL platelet micelles ....................... 308

5.4 Conclusions ........................................................................ 311

5.5 Experimental ........................................................................ 312

5.5.1 Materials ........................................................................ 312

5.5.2 Instrumentation ........................................................................ 312

5.5.3 Synthesis of $PCL_{50}$ ........................................................................ 317

5.5.4 Synthesis of $PCL_{50}$-b-$PDMA_{180}$ ........................................................ 317

5.5.5 Typical crystallisation-driven self-assembly method for the self-nucleation of PCL block copolymers ........................................................ 317

5.5.6 Sonication of $PCL_{50}$-b-$PDMA_{180}$ cylindrical micelles ....................... 318

5.5.7 Typical crystallisation-driven self-assembly method for the epitaxial growth of PCL block copolymers ................................................... 318

5.5.8 End group modification of $PCL_{50}$-b-$PDMA_{180}$ ................................. 319

5.5.9 Synthesis of $PCL_{50}$-b-$PDMAEMA_{170}$ ... 319

5.5.10 Synthesis of $PCL_{50}$-b-$PMMA_{20}$ ... 320

5.5.11 Synthesis of $PCL_{50}$-b-$PMMA_{20}$-b-$PDMA_{200}$ ... 320

5.6 Acknowledgements ... 321

5.7 References ... 322

**Chapter Six – Conclusions and Outlook ... 326**

6.1 Summary ... 327

6.2 Principal conclusions ... 328

6.2.1 Solubility-controlled crystallisation ... 328

6.2.2 The importance of nanoparticle shape ... 329

6.2.3 The importance of nanoparticle size ... 330

6.3 Outlook ... 331

# *Acknowledgements*

Firstly, I would like to give my sincere thanks to my supervisor, Professor Rachel O'Reilly for the opportunity to work in her group in such an amazing field. I am truly grateful for all of your invaluable guidance, advice and continued optimism throughout my PhD studies. I would also like to thank Professor Andrew Dove for all of his support and many useful discussions over the years. Working both of you has allowed me to expand my scientific focus, and I can honestly say that our meetings have been enjoyable and encouraged me to continue on throughout the years.

My whole-hearted thanks goes to both the O'Reilly and Dove group members, past and present, who have not only made my time here more enjoyable, but helped me countless times during my PhD – your numerous suggestions and constructive criticisms have supported me through many challenging days. I would especially like to thank Dr Anaïs Pitto-Barry for being my go-to for any synthetic, self-assembly or even admin-related question I could possibly think to ask. My genuine thanks also goes to Dr Mathew Robin, Dr Rebecca Williams, Dr Marianne Rolph and Dr Lewis Blackman for fielding many a question over the years, Dr Elena Lestini for being my own personal cheerleader and Mr Robert Keogh and Mr Zachary Coe for making the lab a more entertaining place to work. I would also like to give a special thanks to Dr Graeme Cambridge for sharing his knowledge in all things crystallisation, which was undoubtedly crucial in transforming my work into a diamond-shaped success story.

I would also like to thank those who I have had the opportunity to work with on joint projects and journal papers; in particular, I would like to thank Dr Maria Chiara

Arno, Dr Joseph Jones and Mr Wei Yu – by working together, we have achieved much more than anything I could have accomplished alone.

I would also like to acknowledge EPRSC for funding and the University of Warwick for the use of their facilities. I am also very grateful to all of the technical staff in the Department of Chemistry and the Microscopy Group for their assistance, especially for their continued support in running endless amounts of transmission electron microscopy.

Finally, I cannot thank enough the most important people in my life; my Amijee, Abujee, Api and Bhaijan Bestie, for their love, care and encouragement, not to mention filling my suitcase with more than I could ever need and the never-ending phone calls that have kept me sane these past few years. I'm sure you have no idea what I am talking about most of the time, but you always listen to me chatter on and on, and for that you have done more for me than you'll ever know.

جَزَاكَ اللهُ خَيْرًا

# *Declaration of Authorship*

This thesis is submitted to the University of Warwick in support for the degree of Doctor of Philosophy. It has been composed by myself and has not been submitted in any previous application for any degree.

The work presented (including data generated and data analysis) was carried out by the author except in the cases clearly stated in the *Acknowledgments* section of each chapter.

Parts of this thesis have been published by the author.

# *List of Publications*

1. *Enhancing hydrogel properties and adhesion with controlled nanoparticle shape*

   M. Inam,[§] M. C. Arno,[§] A. C. Weems, A. L. A. Binch, S. Richardson, J. A. Hoyland, R. K. O'Reilly, A. P. Dove, *Manuscript in preparation*.
2. *Self-healing, stretchable thiol-yne interpenetrating networks through utilizing the properties of natural polymers*

   L. J. Macdougall, M. M. Pérez-Madrigal, M. Inam, R. K. O'Reilly, A. P. Dove, *Manuscript in preparation.*
3. *2D Platelet size effects on antimicrobial activity*

   M. Inam, J. Gao, Y. Hong, Z. Coe, J. Du, A. P. Dove, R. K. O'Reilly, *Manuscript in preparation.*
4. *Palladium-polymer nanoreactors for the aqueous asymmetric synthesis of therapeutic flavonoids*

   E. Lestini, L. D. Blackman, C. M. Zammit, T. Chen, R. J. Williams, M. Inam, B. Couturaud, R. K. O'Reilly, *Polym. Chem.*, 2018, **9**, 820-823.
5. *Controlling the size of 2D polymer platelets for water-in-water emulsifiers*

   M. Inam, J. P. Jones, M. M. Pérez-Madrigal, M. C. Arno, A. P. Dove, R. K. O'Reilly, *ACS Cent. Sci.*, 2018, **4**, 63-70.
6. *Precision epitaxy for aqueous 1D and 2D poly(ε-caprolactone) assemblies*

   M. C. Arno,[§] M. Inam,[§] Z. Coe, G. Cambridge, L. Macdougall, R. Keogh, A. P. Dove, R. K. O'Reilly, *J. Am. Chem. Soc.*, 2017, **139**, 16980-16985.
7. *The application of blocked isocyanate chemistry in the development of tunable thermoresponsive crosslinkers*

   M. Rolph, M. Inam, R. K. O'Reilly, *Polym. Chem.*, 2017, **8**, 7229-7239.

---

[§] These authors contributed equally.

8. *Understanding the CDSA of poly(lactide) containing triblock copolymers*

   W. Yu, M. Inam, J. R. Jones, A. P. Dove, R. K. O’Reilly, *Polym. Chem.*, 2017, **8**, 5504-5512.

9. *1D vs. 2D shape selectivity in the crystallization-driven self-assembly of polylactide block copolymers*

   M. Inam, G. Cambridge, A. Pitto-Barry, Z. P. L. Laker, N. R. Wilson, R. T. Mathers, A. P. Dove, R. K. O'Reilly, *Chem. Sci.*, 2017, **8**, 4223-4230.

10. *Core functionalization of semi-crystalline polymeric cylindrical nanoparticles using photo-initiated thiol-ene radical reactions*

    L. Sun, A. Pitto-Barry, A. W. Thomas, M. Inam, K. Doncom, A. P. Dove, R. K. O’Reilly, *Polym. Chem.*, 2016, **7**, 2337-2341.

# Summary

**Chapter One** gives a broad introduction to the research described herein, initially discussing the reasons for morphology control, polymerisation techniques and self-assembly methods. A general introduction to solution crystallisation of polymers is given, with a focus on block copolymers with a crystalline core-forming block.

**Chapter Two** discusses the use of various poly(L-lactide) based amphiphiles to propose a unimer solubility-based shape selectivity mechanism for the formation of 1D and 2D nanostructures, leading to a single component solution phase protocol for the preparation of uniform diamond-shaped platelets.

**Chapter Three** considers the use of three different morphologies, namely spheres, cylinders and platelets, as nanocomposites in calcium alginate hydrogels, where a greater shear strength is measured for platelet-composite hydrogels.

**Chapter Four** utilises the proposed unimer solubility approach to create 2D diamond-shaped platelets of controlled size and shape. The use of different size platelets as water-in-water Pickering emulsifiers is explored, where larger plates are shown to give more stable emulsions.

**Chapter Five** employs the use of a poly(ε-caprolactone) crystallisable core-forming block for the preparation of 1D cylindrical structures of controlled length and dispersity. Direct epitaxial growth in water is shown, leading to the preparation of strong hydrogel materials.

**Chapter Six** summarises the research presented, giving general conclusions as well as discussing the scope for future investigations in this area of research.

# Abbreviations

| | |
|---|---|
| 1D | One-dimensional |
| 2D | Two-dimensional |
| 3D | Three-dimensional |
| $\gamma$ | Interfacial tension |
| $\delta$ | Chemical shift |
| $\delta_{\mathrm{h}}$ | Hildebrand solubility parameter |
| $\varepsilon_0$ | Permittivity of free space |
| $\varepsilon_r$ | Dielectric constant |
| $\sigma$ | Standard deviation |
| $\zeta$-potential | Zeta potential |
| $\eta$ | Dynamic viscosity |
| $\eta_d$ | Viscosity of a dispersed phase |
| $\eta_m$ | Viscosity of a matrix or continuous phase |
| $\theta$ | Angle |
| $\lambda$ | Wavelength |
| $\lambda_{\mathrm{Em.}}$ | Wavelength of emission |
| $\lambda_{\mathrm{Ex.}}$ | Wavelength of excitation |
| $\mu_e$ | Electrophoretic mobility |
| µg | Microgram(s) |
| µL | Microlitre(s) |
| µmol | Micromole(s) |
| $\tau$ | Relaxation time |
| $\tau_{Ca}$ | Capillary time |

| | |
|---|---|
| $\omega$ | Angular frequency |
| Å | Angstrom(s) |
| $a_0$ | Optimal area of the interface |
| ABM | Aminobromomaleimide |
| AEA | Acrylamidoethylamine |
| AEANBoc | *tert*-Butyl (2-acrylamidoethyl) carbamate |
| AFM | Atomic force microscopy |
| AIBN | 2,2-Azobis(2-methylpropionitrile) |
| AM | Acrylamide |
| AN | Acrylonitrile |
| Ar | Aromatic |
| ATRP | Atom transfer radical polymerisation |
| br | Broad |
| BCP | Block copolymer |
| Boc | *tert*-Butoxycarbonyl |
| *c* | Concentration |
| *ca.* | Circa |
| CDSA | Crystallisation-driven self-assembly |
| Cryo | Cryogenic |
| CSIRO | Commonwealth Scientific and Industrial Research Organisation |
| CTA | Chain transfer agent |
| *d* | Deuterium labelled |
| *d* | Diameter |
| d | Doublet |
| *D* | Diffusion co-efficient |

| | |
|---|---|
| $D_{app}$ | Apparent diffusion co-efficient |
| DCM | Dichloromethane |
| DCTB | Trans-2-[3-(4-*tert*-butylphenyl)-2-methyl-2-propylidene] malonitrile |
| dd | Doublet of doublets |
| $D_{\mathrm{h}}$ | Hydrodynamic diameter |
| DLS | Dynamic light scattering |
| $Đ_{\mathrm{M}}$ | Molar-mass dispersity |
| DMA | *N*,*N*-Dimethlyacrylamide |
| DMAc | *N*,*N*-Dimethylacetyl amide |
| DMAEMA | 2-(Dimethylamino)ethyl methacrylate |
| DMF | *N*,*N*-Dimethyl formamide |
| DMSO | Dimethylsulfoxide |
| DN | Double network |
| DP | Number average degree of polymerisation |
| DPP | Diphenyl phosphate |
| DSC | Differential scanning calorimetry |
| $E$ | Electric field strength |
| ECM | Extracellular matrix |
| EDC.HCl | 1-Ethyl-3-(3-dimethylaminopropyl)carbodiimide hydrochloride |
| eq. | Equivalents |
| EtOH | Ethanol |
| eV | Electron volts |
| exp | Exponential |
| FDA | Food and Drug Administration |
| FITC | Fluorescein isothiocyanate |

| | |
|---|---|
| FTIR | Fourier transform infrared |
| $G'$ | Storage modulus |
| $G''$ | Loss modulus |
| GO | Graphene oxide |
| HPMA | 2-Hydroxypropyl methacrylate |
| I | Initiator |
| IPN | Interpenetrating network |
| IR | Infrared |
| J | Coupling constant in NMR spectroscopy |
| $k$ | Rate constant |
| $K$ | Viscosity ratio |
| kDa | Kilodaltons |
| $l$ | Thickness |
| L | Length of a deformed droplet on the longest axis |
| $L_0$ | Length of a relaxed droplet |
| $L_i$ | Length of each counted particle |
| $L_n$ | Number-average length |
| $L_w$ | Weight-average length |
| LAM | Less activated monomer |
| $l_c$ | Length of a hydrophobic block |
| $\mathrm{Log}P_{oct}$ | Octanol-water partition co-efficient |
| m | Multiplet |
| M | Monomer |
| m/z | Mass to charge ratio |
| MA | Methyl acrylate |

| | |
|---|---|
| MADIX | Macromolecular design *via* the interchange of xanthates |
| MALDI-ToF | Matrix-assisted laser desorption ionisation – time of flight |
| MAM | More activated monomer |
| MeOH | Methanol |
| mg | Milligram(s) |
| mL | Millilitre(s) |
| MMA | Methyl methacrylate |
| mmol | Millimole(s) |
| $M_n$ | Number average molecular weight |
| mol | Mole(s) |
| MS | Mass spectrometry |
| mV | Millivolt(s) |
| $M_w$ | Weight average molecular weight |
| MWCO | Molecular weight cut off |
| NaCl | Sodium chloride |
| NC | Nanocomposite |
| $N_i$ | Number of micelles of length $L_i$ |
| NMR | Nuclear magnetic resonance |
| NMP | Nitroxide-mediated polymerisation |
| NVC | *N*-vinyl carbazole |
| NVP | *N*-vinyl pyrrolidone |
| $p$ | Packing parameter |
| P4AM | Poly(4-acryloyl morpholine) |
| Pa | Pascal |
| PAA | Poly(acrylic acid) |

| | |
|---|---|
| PAEA | Poly(acrylamidoethylamine) |
| PAEANBoc | Poly(*tert*-butyl (2-acrylamidoethyl) carbamate) |
| PAN | Poly(acrylonitrile) |
| PBS | Phosphate-buffered saline |
| PCL | Poly(ε-caprolactone) |
| PD | Polydispersity in DLS analysis |
| PDLA | Poly(D-lactide) |
| PDMA | Poly(*N*,*N*-dimethlyacrylamide) |
| PDMAEMA | Poly(2-(dimethylamino)ethyl methacrylate) |
| PDMS | Poly(dimethylsiloxane) |
| PE | Poly(ethylene) |
| PEG | Poly(ethylene glycol) |
| PEO | Poly(ethylene oxide) |
| PET | Poly(ethylene terephthalate) |
| PFS | Poly(ferrocenyldimethylsilane) |
| PGMA | Poly(glycerol monomethacrylate) |
| PHPMA | Poly(2-hydroxypropyl methacrylate) |
| PISA | Polymerisation-induced self-assembly |
| PLA | Poly(lactide) |
| PLLA | Poly(L-lactide) |
| PMMA | Poly(methyl methacrylate) |
| $P_n$ | Polymer with a degree of polymerisation of n |
| PP | Poly(propylene) |
| ppm | Parts per million |
| $P(q)$ | Scattering form factor |

| | |
|---|---|
| PRINT | Particle replication in non-wetting templates |
| PS | Poly(styrene) |
| PTA | Phosphotungstic acid |
| PVA | Poly(vinyl alcohol) |
| q | Quartet |
| $r_0$ | Radius of a relaxed droplet |
| RAFT | Reversible addition-fragmentation chain transfer |
| RDRP | Reversible deactivation radical polymerisation |
| $R_\mathrm{g}$ | Radius of gyration |
| RI | Refractive index |
| ROP | Ring-opening polymerisation |
| RT | Room temperature |
| s | Singlet |
| SA | Surface area |
| SAED | Selected area electron diffraction |
| SANS | Small-angle neutron scattering |
| SAXS | Small-angle X-ray scattering |
| SEC | Size exclusion chromatography |
| SEM | Scanning electron microscopy |
| Semi-IPN | Semi-interpenetrating network |
| SLS | Static light scattering |
| St | Styrene |
| Sulfo-NHS | *N*-Hydroxysulfosuccinimide sodium salt |
| $t$ | Time |
| t | Triplet |

| | |
|---|---|
| $T_{\mathrm{Agg}}$ | Aggregation temperature |
| $T_{\mathrm{c}}$ | Crystallisation temperature |
| TCEP.HCl | Tris(2-carboxyethyl)phosphine hydrochloride |
| TEA | Triethylamine |
| TEG | Triethylene glycol |
| TEM | Transmission electron microscopy |
| TFA | Trifluoroacetic acid |
| $T_{\mathrm{g}}$ | Glass transition temperature |
| $T_{\mathrm{m}}$ | Melting temperature |
| THF | Tetrahydrofuran |
| Thiourea | 1-[3,5-bis(trifluoromethyl)phenyl]-3-cyclohexylthiourea |
| THPA | Tetrahydropyran acrylate |
| TMS | Trimethylsilane |
| UA | Uranyl acetate |
| UV | Ultraviolet |
| $v$ | Volume |
| $v_e$ | Electrophoretic velocity |
| VAc | Vinyl acetate |
| WAXS | Wide angle X-ray scattering |
| wt. % | Weight percent |

# *List of Figures*

**Figure 1.1** The main components of a polymer which can be used to change the resultant properties of the material, where blue and red indicate different monomers.3

**Figure 1.2** Example of a RAFT polymer using a generic RAFT CTA, indicating the Z group at the ω-end and the R group at the α-end. .................................................. 9

**Figure 1.3** Classes of chain transfer agent used in RAFT polymerisation; (a) dithioester, (b) dithiocarbamate, (c) trithiocarbonate and (d) xanthate. .................... 10

**Figure 1.4** General guidelines for RAFT agent Z group selection. Addition rates decrease from left to right (fragmentation rates increase). Dashed lines indicate partial control.[22] ........................................................................................ 11

**Figure 1.5** General guidelines for RAFT agent R group selection. Fragmentation rate decreases from left to right. Dashed lines indicate partial control.[22] ........................ 12

**Figure 1.6** Ring-opening polymerisation of L-lactide using a thiourea/(-)-sparteine organocatalytic system. ........................................................................................ 15

**Figure 1.7** Ring-opening polymerisation of ε-caprolactone using DPP as a catalyst. ...................................................................................................................... 16

**Figure 1.8** Different morphologies obtained by targeting different packing parameters in a hydrophilic solvent, where v is the volume of the hydrophobic block, lc is the length of the hydrophobic block and a0 is the optimal area of the interface. Structures in red represent hydrophobic blocks and structures in blue represent hydrophilic blocks. [64] ........................................................................................ 18

**Figure 1.9** TEM micrographs of PGMA-*b*-PHPMA pure phase spheres, worms and vesicles prepared using PISA, where the phases are obtained using different block ratios or solids contents as stated.[72] ........................................................................ 20

**Figure 1.10** Comparison of a random amorphous polymer chain with a regularly folded semi-crystalline polymer chain. ..................................................................... 21

**Figure 1.11** High and low tethering density of diblock copolymers with a semi-crystalline core block given by low and high chain folding numbers, respectively. Corona chains are only shown on one side for clarity. ............................................. 22

**Figure 1.12** TEM micrographs of crystalline PFS (a) cylindrical multi-blocks and (b) scarf-like structures. Scale bar = 500 nm. ........................................................... 25

**Figure 1.13** (a) Amorphous molecular ties connecting lamellae to form multilayer crystals. (b) TEM micrograph of a PLLA crystal prepared by Chen and co-workers showing multi-layers.[120] ............................................................................. 29

**Figure 1.14** (a) Multi-layer crystal showing a screw dislocation defect, where the crystal continues to spiral upward. (b) TEM micrograph of a PLLA crystal prepared by Chen and co-workers showing the screw dislocation defect.[120] ........................... 30

**Figure 1.15** TEM micrographs of poly(ε-caprolactone)-based nanostructures stained using uranyl actate (1 wt. % in 18.2 MΩ·cm water) showing (a) negative stain, (b) positive stain and (c) excess positive staining. ......................................................... 33

**Figure 1.16** Diagram of AFM convolution effects, where the size of the tip causes particles to appear larger in size, but has no noted effect on particle height in the measured profile. ........................................................................................... 35

**Figure 1.17** Graph showing how zeta potential can vary with pH, indicating how the desired pH of more stable particles can be identified by the magnitude of zeta potential measurements. ........................................................................... 38

**Figure 2.1** Growth of 2D platelet micelles by sequential additions of functional unimers with a core-corona block ratio of ≥1:1.[31] .................................................... 51

**Figure 2.2** Morphological transformation of poly(ethylene oxide) (PEO)-*b*-PCL block copolymer crystalline assemblies induced by the incorporation of $PCL_{10}$ homopolymer. Scale bar = 2 µm.[33] ............ 52

**Figure 2.3** TEM micrograph of PLLA-*b*-PAA cylindrical micelles (stained with phosphotungstic acid). Scale bar = 500 nm.[35] ............ 53

**Figure 2.4** $^1H$ NMR spectrum ($CDCl_3$, 400 MHz) of *N*-Boc-ethylenediamine. ............ 58

**Figure 2.5** $^1H$ NMR spectrum ($CDCl_3$, 400 MHz) of AEANBoc. ............ 59

**Figure 2.6** $^1H$ NMR spectrum ($CDCl_3$, 400 MHz) of $PLLA_{36}$. ............ 61

**Figure 2.7** Overlaid RI and UV ($\lambda$ = 309 nm) SEC chromatograms of $PLLA_{36}$ using DMF with 0.1% LiBr as an eluent with PMMA standards. ............ 62

**Figure 2.8** MALDI-ToF mass spectrum of $PLLA_{36}$ showing a m/z difference of 144.13 equivalent to one PLLA unit and therefore minimal transesterification. ............ 62

**Figure 2.9** DSC thermogram of $PLLA_{36}$ measured at a heating rate of 2 °C per minute. ............ 63

**Figure 2.10** $^1H$ NMR spectrum ($(CD_3)_2SO$, 400 MHz) of $PLLA_{36}$-*b*-$PAEANBoc_{295}$. ............ 64

**Figure 2.11** Overlaid RI and UV ($\lambda$ = 309 nm) SEC chromatograms of $PLLA_{36}$-*b*-$PAEANBoc_{295}$ in comparison with $PLLA_{36}$ homopolymer using DMF with 0.1% LiBr as an eluent with PMMA standards. ............ 65

**Figure 2.12** Overlaid $^1H$ NMR spectrum ($(CD_3)_2SO$, 400 MHz) of $PLLA_{36}$-*b*-$PAEANBoc_{295}$ and $PLLA_{36}$-*b*-$PAEA_{295}$ showing the disappearance of the *tert*-butoxycarbonyl (Boc) peak after reaction with trifluoroacetic acid in $CH_2Cl_2$. ............ 66

**Figure 2.13** (a) DLS analysis with correlation function (inset) and (b) TEM micrograph of $PLLA_{36}$-*b*-$PAEA_{295}$ spherical micelles at pH 6.5 in water. Samples were stained with 1 wt. % uranyl acetate in water. Scale bar = 100 nm. ............ 67

**Figure 2.14** TEM micrographs of $PLLA_{36}$-*b*-$PAEA_{295}$ self-assemblies prepared in a 1:1 DMF:$H_2O$ solution and heated at 65 °C for (a) 30 hours, (b) 100 hours and (c) 200 hours. Samples were stained with 1 wt. % uranyl acetate in water. Scale bar = 100 nm. 69

**Figure 2.15** WAXD diffractogram of a $PLLA_{36}$-*b*-$PAEA_{295}$ self-assembly prepared in a 1:1 DMF:$H_2O$ solution and heated at 65 °C for 200 hours (**Figure 2.14c**). The assembly was exhaustively dialysed against 18.2 MΩ·cm water and lyophilised before WAXD analysis. 69

**Figure 2.16** TEM micrographs of $PLLA_{36}$-*b*-$PAEA_{295}$ self-assemblies prepared in a 1:1 DMF:$H_2O$ solution at a concentration of 5 mg $mL^{-1}$ and heated at (a) 65 °C and (b) 80 °C for 30 hours. (c) TEM micrograph of a $PLLA_{36}$-*b*-$PAEA_{295}$ self-assembly prepared in a 1:1 DMF:$H_2O$ solution at a concentration of 1 mg $mL^{-1}$ and heated at 90 °C for 30 hours. Samples were stained with 1 wt. % uranyl acetate in water. Scale bar = 500 nm. 70

**Figure 2.17** WAXD diffractogram of a $PLLA_{36}$-*b*-$PAEA_{295}$ self-assembly prepared in a 1:1 DMF:$H_2O$ solution at a concentration of 1 mg $mL^{-1}$ and heated at 90 °C for 30 hours (**Figure 2.16c**), showing a peak at 16°, characteristic of crystalline PLLA. The assembly was exhaustively dialysed against 18.2 MΩ·cm water and lyophilised before WAXD analysis. 70

**Figure 2.18** TEM micrographs of $PLLA_{36}$-*b*-$PAEA_{295}$ self-assemblies prepared at 5 mg $mL^{-1}$ in (a) ethanol and (b) *n*-propanol heated at 65 °C for 60 hours. Samples were stained with 1 wt. % uranyl acetate in water. Scale bar = 100 nm. 71

**Figure 2.19** TEM micrographs of $PLLA_{36}$-*b*-$PAEA_{295}$ self-assemblies prepared at 5 mg $mL^{-1}$ in (a) ethanol, (b) *n*-propanol and (c) *n*-butanol heated at 90 °C for 2 hours. Samples were stained with 1 wt. % uranyl acetate in water. Scale bar = 500 nm. ..... 72

**Figure 2.20** WAXD diffractogram of a PLLA$_{36}$-*b*-PAEA$_{295}$ self-assembly prepared at 5 mg mL$^{-1}$ in ethanol heated at 90 °C for 2 hours (**Figure 2.19a**), showing a peak at 16°, characteristic of crystalline PLLA. The assembly was cooled to room temperature and dried before WAXD analysis. ..... 72

**Figure 2.21** Log$P_{oct}$ hydrophobicity calculations of various polymers compared to ethanol, showing a much greater hydrophobicity mismatch with PAEA in comparison to PAA and PDMA.[§] ..... 73

**Figure 2.22** Overlaid $^1$H NMR spectra (CHCl$_3$, 400 MHz) of PLLA$_{48}$-*b*-PDMA$_m$ block copolymers with different block ratios. ..... 75

**Figure 2.23** Overlaid RI SEC chromatograms of PLLA$_{48}$-*b*-PDMA$_m$ block copolymers with different block ratios in comparison with PLLA$_{48}$ homopolymer using DMF with 0.1% LiBr as an eluent with PMMA standards. ..... 76

**Figure 2.24** DOSY NMR spectrum (500 MHz, CDCl$_3$) of PLLA$_{48}$-*b*-PDMA$_{1000}$. ..... 76

**Figure 2.25** Structure of hexameric models based on poly(L-lactide) (PLLA) and poly(*N*,*N*-dimethylacrylamide) (PDMA). ..... 77

**Figure 2.26** Log$P_{oct}$ hydrophobicity calculations (violet) and Hildebrand solubility parameters (red)[58] of PLLA and PDMA compared to *n*-butanol, *n*-propanol, ethanol and methanol. Log$P_{oct}$ hydrophobicity calculations noted a similar trend with oligomeric models composed of octamers. PLLA incorporated a MeO initiator with an OH end-group. PDMA was hydrogen terminated. ..... 78

**Figure 2.27** TEM micrographs of 1:12.5 core-to-corona ratio PLLA$_{48}$-*b*-PDMA$_{600}$ self-assembled in (a) ethanol, (b) *n*-propanol and (c) *n*-butanol at 65 °C for 18 hours and cooled to room temperature. Samples were stained with uranyl acetate. Scale bar = 1 μm.[§] ........................................................................................................ 79

**Figure 2.28** TEM micrographs of core-to-corona ratio 1:20 PLLA$_{48}$-*b*-PDMA$_{1000}$ self-assembled in ethanol at 90 °C for (a) 2 hours, (b) 4 hours, (c) 6 hours and (d) 8 hours before cooling to room temperature. Samples were stained with uranyl acetate. Scale bar = 1 μm. (e) Schematic of the kinetics of diamond-shaped platelet formation. ........................................................................................................ 80

**Figure 2.29** (a) AFM image and (b) height profile of core-to-corona ratio 1:20 PLLA$_{48}$-*b*-PDMA$_{1000}$ self-assembled in ethanol at 90 °C for 8 hours. Scale bar = 2 μm. ........................................................................................................ 80

**Figure 2.30** TEM micrographs of a series of PLLA$_{48}$-*b*-PDMA$_{m}$ block copolymers of core-to-corona ratios of (a) 1:20 (m = 1000), (b) 1:12.5 (m = 600), (c) 1:5 (m = 250) and (d) 1:3 (m = 150). Samples were self-assembled in ethanol at 90 °C for 8 hours and cooled to room temperature. Samples were stained with 1 wt. % uranyl acetate in water. Scale bar = 1 μm.................................................................................... 81

**Figure 2.31** TEM micrographs of PLLA$_{48}$-*b*-PDMA block copolymers of core-to-corona ratios of (a) 1:5 and (b) 1:3. Samples were self-assembled in ethanol at 90 °C for 18 hours and cooled to room temperature. Samples were stained with 1 wt. % uranyl acetate in water. Scale bar = 1 μm. ............................................................... 82

**Figure 2.32** (a) SAED analysis[§] and (b) WAXD diffractogram showing the 2$\theta$ peak at 16° (characteristic of crystalline PLLA) of 1:20 core-to-corona ratio PLLA$_{48}$-*b*-PDMA$_{1000}$ diamond platelets. The WAXD broad background signal can be attributed to the large, amorphous PDMA block for this 1:20 ratio block copolymer............... 83

**Figure 2.33** Overlaid RI and UV ($\lambda$ = 309 nm) SEC chromatograms of PLLA$_{36}$-*b*-PDMA$_{245}$ end group modified with acrylic acid using DMF with 0.1% LiBr as an eluent with PMMA standards. ........ 86

**Figure 2.34** TEM micrographs of cylinder-forming (1:3 core-to-corona ratio) PLLA$_{48}$-*b*-PDMA$_{150}$ block copolymers (a) unmodified and (b) modified with a carboxylic acid group or (c) modified with an amine group. Samples were self-assembled in ethanol at 90 °C for 8 hours and cooled to room temperature. Samples were stained with 1 wt. % uranyl acetate in water. Scale bar = 1 μm. ........ 87

**Figure 2.35** TEM micrographs of PLLA$_{48}$-*b*-PDMA$_m$ blends of block ratios 1:20 (m = 1000) and 1:3 (m = 150), at blending ratios of (a) 25:75, (b) 50:50 and (c) 75:25, self-assembled in ethanol at 90 °C for 8 hours and cooled to room temperature. Samples were stained with 1 wt. % uranyl acetate in water. Scale bar = 1 μm. ........ 88

**Figure 2.36** TEM micrographs of PLLA$_{48}$-*b*-PDMA$_m$ blends of block ratios 1:20 (m = 1000) and 1:3 (m = 150) at a blending ratio of 50:50, self-assembled in ethanol at 90 °C for 8 hours and cooled to room temperature for (a) 5 minutes, (b) 10 minutes, (c) 20 minutes, (d) 30 minutes, (e) 40 minutes and (f) 50 minutes before being crash cooled in liquid nitrogen. Samples were stained with uranyl acetate. Scale bar = 1 μm. ........ 90

**Figure 2.37** TEM micrographs of PLLA$_{48}$-*b*-PDMA$_{1000}$ block copolymer self-assembled in (a) 95% ethanol with 5% water and (b) 90% ethanol with 10% water at 90 °C for 8 hours and cooled to room temperature. Samples were stained with 1 wt. % uranyl acetate in water. Scale bar = 1 μm. ........ 91

**Figure 2.38** $^1$H NMR spectrum ($CDCl_3$, 400 MHz) of dual-headed ROP initiator and chain transfer agent dodecyl 4-(hydroxymethyl) benzyl carbonotrithioate. ........ 100

**Figure 2.39** $^{13}$C NMR spectrum ($CDCl_3$, 150 MHz) of dual-headed ROP initiator and chain transfer agent dodecyl 4-(hydroxymethyl) benzyl carbonotrithioate. ..... 101

**Figure 3.1** Diagram of a simple crosslinked hydrogel using one monomer type in a single polymer network in comparison to a hybrid gel copolymerising two monomer types and both IPN and semi-IPN DN hydrogels incorporating a second polymer network. ........ 119

**Figure 3.2** (a) Polymer-nanoparticle hydrogel showing release of drug cargo. (b) Step-strain measurements of the polymer-nanoparticle hydrogel showing self-healing behaviour over three cycles ($\omega$ = 10 rad $s^{-1}$).[32] ........ 120

**Figure 3.3** Adhesion of polymer networks by numerous sites of adsorption of the network chains to the surface of the nanoparticles, where the black arrows indicate the pressure applied adhere the gel layers together.[55] ........ 122

**Figure 3.4** $^{1}$H NMR spectrum ($CDCl_3$, 400 MHz) of $PLLA_{36}$ prepared with an ethyl-terminated chain transfer agent. ........ 126

**Figure 3.5** Overlaid RI and UV ($\lambda$ = 309 nm) SEC chromatograms of $PLLA_{36}$ prepared with an ethyl-terminated chain transfer agent using *N*,*N*-dimethyl formamide (DMF) with 0.1% LiBr as an eluent with PMMA standards................ 127

**Figure 3.6** MALDI-ToF of $PLLA_{36}$ prepared with an ethyl-terminated chain transfer agent showing a m/z difference of 144.13 equivalent to one PLLA unit and therefore minimal transesterification. ........ 127

**Figure 3.7** Differential scanning calorimetry thermogram of $PLLA_{36}$ prepared with an ethyl-terminated chain transfer agent measured at a heating rate of 2 °C per minute. Additional features may be due to residual solvent during a first heating cycle. ........ 128

**Figure 3.8** $^{1}$H NMR spectrum ($CDCl_3$, 400 MHz) of $PLLA_{36}$-*b*-$PDMAEMA_{216}$... 129

**Figure 3.9** Overlaid RI and UV ($\lambda$ = 309 nm) SEC chromatograms of PLLA$_{36}$-*b*-PDMAEMA$_{216}$ in comparison with PLLA$_{36}$ homopolymer using DMF with 0.1% LiBr as an eluent with PMMA standards. ............................................ 130

**Figure 3.10** TEM micrographs and DLS analysis of PLLA$_{36}$-*b*-PDMAEMA$_{216}$ particles prepared *via* solvent switch using (a) acetonitrile, (b) DMF, (c) THF and (d) 1,4-dioxane as a common solvent. Samples were stained with 1 wt. % uranyl acetate in water. Scale bar = 100 nm........................................................................ 131

**Figure 3.11** TEM micrographs of PLLA$_{36}$-*b*-PDMAEMA$_{216}$ self-assemblies prepared in 1:1 DMF:$H_2O$ heated at (a) 65 °C, (b) 90 °C, (c) 55 °C and (d) 60 °C for 30 hours. Samples were stained with 1 wt. % uranyl acetate in water. Scale bar = 100 nm......................................................................................................... 133

**Figure 3.12** WAXD diffractogram of a PLLA$_{36}$-*b*-PDMAEMA$_{216}$ self-assembly heated at 55 °C for 30 hours, showing a peak at 16°, characteristic of crystalline PLLA The assembly was dialysed against 18.2 MΩ·cm water and lyophilised before analysis. ........................................................................................................ 133

**Figure 3.13** TEM micrographs of PLLA$_{36}$-*b*-PDMAEMA$_{216}$ self-assemblies prepared at 5 mg mL$^{-1}$ in (a) ethanol and heated at 65 °C for 60 hours, (b) 95% ethanol/5% THF and heated at 65 °C for 30 hours and (c) 80% Ethanol/20% THF and heated at 65 °C for 30 hours. Samples were stained with 1 wt. % uranyl acetate in water. Scale bar = 100 nm........................................................................ 135

**Figure 3.14** TEM micrographs of PLLA$_{36}$-*b*-PDMAEMA$_{216}$ self-assemblies prepared at 5 mg mL$^{-1}$ in (a) 95% *n*-butanol/5% THF and heated at 65 °C, (b) 80% *n*-Butanol/20% THF and heated at 65 °C and (c) 95% *n*-Butanol/5% THF and heated at 55 °C for 30 hours. Samples were stained with 1 wt. % uranyl acetate in water. Scale bar = 100 nm........................................................................................ 136

**Figure 3.15** TEM micrographs and DLS analysis of $PLLA_{36}$-*b*-$PDMAEMA_{216}$ assembled in (a) ethanol and (b) *n*-butanol at 90 °C for 2 hours. TEM micrographs and DLS analysis of $PLLA_{36}$-*b*-$PDMAEMA_{315}$ assembled in (a) ethanol and (b) n-butanol at 90 °C for 2 hours. Samples were stained with 1 wt. % uranyl acetate in water. Scale bar = 1000 nm. ........ 137

**Figure 3.16** WAXD diffractogram of $PLLA_{36}$-*b*-$PDMAEMA_{216}$ assembled in ethanol at 90 °C for 2 hours, showing a strong peak at 16°, characteristic of highly crystalline PLLA. The assembly was cooled to room temperature and dried before WAXD analysis. ........ 138

**Figure 3.17** (a) Atomic force micrograph and (b) height profile of $PLLA_{36}$-*b*-$PDMAEMA_{216}$ assembled in ethanol at 90 °C for 2 hours and cooled to room temperature. ........ 138

**Figure 3.18** $^1$H NMR spectrum ($CDCl_3$, 400 MHz) of $PLLA_{36}$-*b*-$PTHPA_{400}$. ....... 141

**Figure 3.19** Overlaid RI and UV ($\lambda$ = 309 nm) SEC chromatograms of $PLLA_{36}$-*b*-$PTHPA_{400}$ in comparison with $PLLA_{36}$ homopolymer using DMF with 0.1% LiBr as an eluent with PMMA standards ........ 141

**Figure 3.20** (a) TEM micrograph on a graphene oxide (GO) substrate and (b) WAXD diffractogram of $PLLA_{36}$-*b*-$PAA_{400}$ cylindrical micelles. Scale bar = 500 nm. ........ 142

**Figure 3.21** IR spectra of $PLLA_{36}$-*b*-$PTHPA_{400}$ in comparison with $PLLA_{36}$-*b*-$PAA_{400}$ showing the evolution of the acid peak at 1715 $cm^{-1}$. ........ 143

**Figure 3.22** DLS analysis with correlation function (inset) and (b) TEM micrograph of $PLLA_{36}$-*b*-$PAA_{400}$ spherical micelles at pH 6.5 in water. Samples were stained with 1 wt. % uranyl acetate in water. Scale bar = 200 nm. ........ 144

**Figure 3.23** $^{1}$H NMR spectrum ($CDCl_3$, 400 MHz) of $PLLA_{36}$-*b*-$PAA_{400}$ modified with dimethylethylenediamine. ............ 146

**Figure 3.24** IR spectra of $PLLA_{36}$-*b*-$PAA_{400}$ modified with dimethylethylenediamine in comparison to $PLLA_{36}$-*b*-$PAA_{400}$ showing the presence of a new peak at 1647 $cm^{-1}$ corresponding to the new amide bond. ............ 146

**Figure 3.25** TEM micrographs of $PLLA_{36}$-*b*-$PAA_{400}$ cylindrical micelles (a) before and (b) after modification with dimethylethylenediamine. Samples were stained with 1 wt. % uranyl acetate in water. Scale bar = 1000 nm. ............ 147

**Figure 3.26** Dynamic oscillatory frequency sweeps of alginate hydrogels with different equivalents of calcium carbonate where $G'$ indicates the storage modulus and $G''$ indicates the loss modulus. ............ 151

**Figure 3.27** Strain-dependent oscillatory rheology measurements of alginate hydrogels with different equivalents of calcium carbonate where $G'$ indicates the storage modulus and $G''$ indicates the loss modulus. ............ 151

**Figure 3.28** (a) Strain-dependent oscillatory rheology and (b) dynamic oscillatory frequency sweeps of calcium alginate hydrogels at 0.36 eq. calcium with 0.5 wt. % and 1.5 wt. % $PLLA_{36}$-*b*-$PAA_{400}$ spheres. ............ 154

**Figure 3.29** (a) Strain-dependent oscillatory rheology and (b) dynamic oscillatory frequency sweeps of calcium alginate hydrogels at 0.70 eq. calcium with 0.5 wt. % and 1.5 wt. % $PLLA_{36}$-*b*-$PAA_{400}$ spheres. ............ 155

**Figure 3.30** (a) Strain-dependent oscillatory rheology and (b) dynamic oscillatory frequency sweeps of calcium alginate hydrogels at 0.36 eq. calcium with 0.5 wt. % and 1.5 wt. % $PLLA_{36}$-*b*-$PAA_{400}$ spheres. ............ 155

**Figure 3.31** (a) Strain-dependent oscillatory rheology and (b) dynamic oscillatory frequency sweeps of calcium alginate hydrogels at 0.70 eq. calcium with 0.5 wt. % and 1.5 wt. % PLLA$_{36}$-*b*-PAA$_{400}$ spheres. .......... 156

**Figure 3.32** (a) Strain-dependent oscillatory rheology and (b) dynamic oscillatory frequency sweeps of calcium alginate hydrogels at 0.80 eq. calcium with 0.5 wt. % PLLA$_{36}$-*b*-PAA$_{400}$ spheres. .......... 156

**Figure 3.33** (a) Strain-dependent oscillatory rheology and (b) dynamic oscillatory frequency sweeps of calcium alginate hydrogels at 0.50 eq. calcium with 0.5 wt. % and 1.5 wt. % PLLA$_{36}$-*b*-PAA$_{400}$ spheres. .......... 157

**Figure 3.34** (a) Strain-dependent oscillatory rheology and (b) dynamic oscillatory frequency sweeps of calcium alginate hydrogels at 0.5 wt. % sodium alginate and 0.36 eq. calcium with 0.5 wt. % PLLA$_{36}$-*b*-PAA$_{400}$ spheres. .......... 157

**Figure 3.35** (a) Strain-dependent oscillatory rheology and (b) dynamic oscillatory frequency sweeps of calcium alginate hydrogels at 0.5 wt. % sodium alginate and 0.50 eq. calcium with 0.5 wt. % PLLA$_{36}$-*b*-PAA$_{400}$ spheres. .......... 158

**Figure 3.36** (a) Strain-dependent oscillatory rheology and (b) dynamic oscillatory frequency sweeps of calcium alginate hydrogels at 0.50 eq. calcium with 0.1 wt. %, 0.3 wt. % and 0.5 wt. % PLLA$_{36}$-*b*-PAA$_{400}$ spheres. .......... 158

**Figure 3.37** (a) Strain-dependent oscillatory rheology and (b) dynamic oscillatory frequency sweeps of calcium alginate hydrogels at 0.50 eq. calcium with 0.1 wt. %, 0.3 wt. % and 0.5 wt. % PLLA$_{36}$-*b*-PAA$_{400}$ cylinders. .......... 159

**Figure 3.38** (a) Strain-dependent oscillatory rheology and (b) dynamic oscillatory frequency sweeps of calcium alginate hydrogels at 0.70 eq. calcium with 0.1 wt. %, 0.3 wt. % and 0.5 wt. % PLLA$_{36}$-*b*-PAA$_{400}$ spheres. .......... 159

**Figure 3.39** (a) Strain-dependent oscillatory rheology and (b) dynamic oscillatory frequency sweeps of calcium alginate hydrogels at 0.70 eq. calcium with 0.1 wt. %, 0.3 wt. % and 0.5 wt. % PLLA$_{36}$-*b*-PAA$_{400}$ cylinders. .......................................... 160

**Figure 3.40** Strain-dependent oscillatory rheology of calcium alginate hydrogels at (a) 0.50 eq. calcium and (b) 0.70 eq. calcium with 0.1 wt. %, 0.3 wt. % and 0.5 wt. % PLLA$_{36}$-*b*-PAEA$_{295}$ spheres. ..................................................................... 162

**Figure 3.41** (a) Strain-dependent oscillatory rheology and (b) dynamic oscillatory frequency sweeps of calcium alginate hydrogels at 0.50 eq. calcium with 0.04 wt. %, 0.06 wt. % and 0.08 wt. % PLLA$_{36}$-*b*-PAEA$_{295}$ spheres. ...................................... 163

**Figure 3.42** (a) Strain-dependent oscillatory rheology and (b) dynamic oscillatory frequency sweeps of calcium alginate hydrogels at 0.70 eq. calcium with 0.04 wt. %, 0.06 wt. % and 0.08 wt. % PLLA$_{36}$-*b*-PAEA$_{295}$ spheres. ...................................... 163

**Figure 3.43** (a) Strain-dependent oscillatory rheology and (b) dynamic oscillatory frequency sweeps of calcium alginate hydrogels at 0.50 eq. calcium with 0.1 wt. %, 0.3 wt. % and 0.5 wt. % PLLA$_{36}$-*b*-PDMAEMA$_{216}$ spheres.................................. 165

**Figure 3.44** (a) Strain-dependent oscillatory rheology and (b) dynamic oscillatory frequency sweeps of calcium alginate hydrogels at 0.70 eq. calcium with 0.1 wt. %, 0.3 wt. % and 0.5 wt. % PLLA$_{36}$-*b*-PDMAEMA$_{216}$ spheres.................................. 165

**Figure 3.45** (a) Strain-dependent oscillatory rheology and (b) dynamic oscillatory frequency sweeps of calcium alginate hydrogels at 0.50 eq. calcium with 0.1 wt. %, 0.3 wt. % and 0.5 wt. % PLLA-*b*-PDMAEMA mimic cylinders, prepared *via* amidation of PLLA$_{36}$-b-PAA$_{400}$ cylinders. ........................................................... 166

**Figure 3.46** (a) Strain-dependent oscillatory rheology and (b) dynamic oscillatory frequency sweeps of calcium alginate hydrogels at 0.50 eq. calcium with 0.1 wt. % and 0.3 wt. % PLLA$_{36}$-*b*-PDMAEMA$_{216}$ platelets................................................. 166

**Figure 3.47** (a) Step-strain measurements of nanocomposite calcium-alginate (0.5 eq. and 1.0 eq. respectively) containing PLLA$_{36}$-*b*-PDMAEMA$_{216}$ diamond-shaped nanoparticles (0.12 wt. %) over three cycles ($\omega = 10$ rad s$^{-1}$) and (b) overlayed zoom of the recovery of the material properties after each cycle. .................................... 169

**Figure 3.48** Comparison of (a) G′ and (b) strain at the flow point for different shape PLLA$_{36}$-*b*-PDMAEMA$_{216}$ nanoparticles at different wt. % incorporations. Error bars indicate standard deviation over three measurements. ............................................ 169

**Figure 3.49** (a) Strain-dependent oscillatory rheology and (b) dynamic oscillatory frequency sweeps of calcium alginate hydrogels at 0.50 eq. calcium with 0.04, 0.06, 0.08, 0.10, and 0.12 wt. % PLLA$_{36}$-*b*-PDMAEMA$_{216}$ platelets. $G'$ indicates the storage modulus and $G''$ indicates the loss modulus. ............................................. 170

**Figure 3.50** (a) Strain-dependent oscillatory rheology and (b) dynamic oscillatory frequency sweeps of calcium alginate hydrogels at 0.50 eq. calcium with 0.04, 0.06, 0.08, 0.10, and 0.12 wt. % PLLA$_{36}$-*b*-PDMAEMA$_{216}$ cylinders. $G'$ indicates the storage modulus and $G''$ indicates the loss modulus. ............................................. 171

**Figure 3.51** (a) Strain-dependent oscillatory rheology and (b) dynamic oscillatory frequency sweeps of calcium alginate hydrogels at 0.50 eq. calcium with 0.04, 0.06, 0.08, 0.10, and 0.12 wt. % PLLA$_{36}$-*b*-PDMAEMA$_{216}$ spheres. $G'$ indicates the storage modulus and $G''$ indicates the loss modulus. ............................................. 172

**Figure 3.52** Photographs of blocks of calcium alginate (0.5 eq. and 1.0 eq. respectively) hydrogel blocks glued together with PLLA$_{36}$-*b*-PDMAEMA$_{216}$ diamond platelets (a) suspended horizontally and (b) held vertically. Food colouring added to the initial alginate solution was used to visualise the different gel blocks. ......................................................................................................................... 174

**Figure 3.53** Bulk shear stress behaviour comparing representative interfacial stresses of two calcium alginate identical gel blocks adhered with PLLA$_{36}$-*b*-PDMAEMA$_{216}$ diamond platelets and spherical micelles against a water-only control. .................. 175

**Figure 4.1** Dextran/gelatin water-in-water emulsion stabilised by Gibbsite nanoplates. ........................................................................................................ 196

**Figure 4.2** TEM micrographs of PLLA$_{36}$-*b*-PDMAEMA$_{216}$ diamond-shaped platelets after sonication using a sonication bath in ethanol for (a) 10 minutes, (b) 30 minutes and (c) 60 minutes. Samples were stained with 1 wt. % uranyl acetate in water. Scale bar = 1000 nm. ...................................................................................................... 201

**Figure 4.3** TEM micrographs of PLLA$_{36}$-*b*-PDMAEMA$_{216}$ diamond-shaped platelets after sonication using a sonic probe in ethanol for (a) 10 minutes and (b) 20 minutes. Samples were stained with 1 wt. % uranyl acetate in water. Scale bar = 1000 nm. 201

**Figure 4.4** TEM micrographs of PLLA$_{36}$-*b*-PDMAEMA$_{216}$ diamond-shaped platelets after sonication in 90% ethanol/10% THF for (a) 10 minutes, (b) 20 minutes, (c) 40 minutes and (d) 60 minutes. TEM micrographs of PLLA$_{36}$-*b*-PDMAEMA$_{216}$ diamond-shaped platelets after sonication in 80% ethanol/20% THF for (e) 20 minutes and (f) 60 minutes. Samples were stained with 1 wt. % uranyl acetate in water. Scale bar = 1000 nm. ...................................................................... 202

**Figure 4.5** TEM micrographs of PLLA$_{36}$-*b*-PDMAEMA$_{216}$ platelets assembled in ethanol at a concentration of (a) 1 mg mL$^{-1}$, (b) 20 mg mL$^{-1}$ and (c) 50 mg mL$^{-1}$ at 90 °C for 2 hours and cooled to room temperature. Samples were stained with 1 wt. % uranyl acetate in water. Scale bar = 1000 nm. .................................................. 203

**Figure 4.6** $^{1}$H NMR spectrum (CDCl$_3$, 400 MHz) of PLLA$_{90}$. ............................... 205

**Figure 4.7** Overlaid RI and UV ($\lambda$ = 309 nm) SEC chromatograms of PLLA$_{90}$ using DMF with 0.1% LiBr as an eluent with poly(methyl methacrylate) (PMMA) standards. 206

**Figure 4.8** MALDI-ToF mass spectrum of PLLA$_{90}$ showing a m/z difference of 144.13 equivalent to one PLLA unit and therefore minimal transesterification. 206

**Figure 4.9** $^1$H NMR spectrum (CDCl$_3$, 400 MHz) of PLLA$_{90}$-*b*-PDMAEMA$_{300}$ 207

**Figure 4.10** Overlaid RI and UV ($\lambda$ = 309 nm) SEC chromatograms of PLLA$_{90}$-*b*-PDMAEMA$_{300}$ in comparison with PLLA$_{90}$ homopolymer using DMF with 0.1% LiBr as an eluent with PMMA standards. 208

**Figure 4.11** TEM micrographs of PLLA$_{90}$-*b*-PDMAEMA$_{300}$ platelets assembled in ethanol at a concentration of (a) 5 mg mL$^{-1}$ and (b) 20 mg mL$^{-1}$ at 90 °C for 2 hours and cooled to room temperature. Samples were stained with 1 wt% uranyl acetate in water. Scale bar = 1000 nm. 208

**Figure 4.12** Overlaid $^1$H NMR spectra (CDCl$_3$, 400 MHz) of different block ratios; PLLA$_{36}$-*b*-PDMAEMA$_{35}$, PLLA$_{36}$-*b*-PDMAEMA$_{57}$, PLLA$_{36}$-*b*-PDMAEMA$_{216}$ and PLLA$_{36}$-*b*-PDMAEMA$_{315}$. 210

**Figure 4.13** Overlaid RI (solid line) and UV (dashed line, $\lambda$ = 309 nm) SEC chromatograms of PLLA$_{36}$-*b*-PDMAEMA$_n$ in comparison with PLLA$_{36}$ homopolymer using DMF with 0.1% LiBr as an eluent with PMMA standards. 210

**Figure 4.14** TEM micrographs of (a) PLLA$_{36}$-*b*-PDMAEMA$_{315}$, (b) PLLA$_{36}$-*b*-PDMAEMA$_{216}$, (c) PLLA$_{36}$-*b*-PDMAEMA$_{57}$, and (d) PLLA$_{36}$-*b*-PDMAEMA$_{35}$ diamond platelets. Samples were self-assembled at 90 °C for 4 h, cooled to room temperature and aged for 1 day. Samples were stained with uranyl acetate. Scale bar = 1 µm. 211

**Figure 4.15** Jitter box plot and average height data showing the negligible difference in area (as determined by TEM) and height of diamond nanoplates (as determined by AFM) regardless of block ratio. .......... 212

**Figure 4.16** Jitter box plot showing the negligible difference in length on the longest axis of the particles (as determined by TEM) regardless of block ratio. .......... 213

**Figure 4.17** Atomic force microscopy of PLLA$_{36}$-*b*-PDMAEMA$_n$ diamond nanoplatelets with a core-to-corona ratio of (a) 1:9 (n = 315) (b) 1:6 (n = 216), (c) 1:2 (n = 57) and (d) 1:1 (n = 35). Samples were self-assembled in ethanol at 90 °C for 4 h and cooled to room temperature and aged for 1 day. Scale bar = 500 nm. .......... 214

**Figure 4.18** Wide-angle X-ray scattering analysis of PLLA$_{36}$-*b*-PDMAEMA$_{315}$ diamond platelets showing the characteristic PLLA crystalline peak at 16.6° 2θ at room temperature. The broad peak from 14-22° 2θ can be assigned to the amorphous PDMAEMA block. .......... 215

**Figure 4.19** Weighted fits of the simulated form factor, P($q$), to the empirical SLS data recorded for PLLA$_{36}$-*b*-PDMAEMA$_{57}$ and PLLA$_{36}$-*b*-PDMAEMA$_{315}$ showing the approximately equal mass average particle size. The evident discrepancy between the empirical data and the model at small scattering angles is attributable to the particle size dispersity. .......... 216

**Figure 4.20** Height profile and AFM image of nanoplatelets prepared with 12% THF. Scale bar = 5 μm. .......... 217

**Figure 4.21** TEM micrographs of nanoplatelets prepared in ethanol with (b) 2%, (c) 4%, (d) 6%, (e) 8%, (f) 10% and (g) 12% THF. Samples were self-assembled at 90 °C for 4 h and cooled to room temperature. Samples were stained with 1 wt. % uranyl acetate in water. Scale bar = 1 μm. .......... 218

**Figure 4.22** Jitter box plot and average height data showing the exponential increase in $PLLA_{36}$-*b*-$PDMAEMA_{216}$ diamond nanoplatelet area (as determined by TEM) with increasing THF content with a negligible difference in height (as determined by AFM). ........ 219

**Figure 4.23** TEM micrographs of 1:6 core-to-corona ratio $PLLA_{36}$-*b*-$PDMAEMA_{216}$ nanoplatelets prepared using 10% THF in ethanol at 90 °C for (a) 4 hours and (b) 8 hours and aged for 1 day. Samples were stained with uranyl acetate. Scale bar = 1 µm. ........ 219

**Figure 4.24** Atomic force microscopy of $PLLA_{36}$-*b*-$PDMAEMA_{216}$ diamond platelets prepared in ethanol with (a) 2%, (b) 4%, (c) 6%, (d) 8%, (e) 10% and (f) 12% THF. Samples were self-assembled at 90 °C for 4 h and cooled to room temperature and then aged for 1 day. Scale bar = 1000 nm. ........ 220

**Figure 4.25** TEM micrograph of $PLLA_{36}$-*b*-$PDMAEMA_{216}$ nanoplatelets *ca.* 9.5 µm in length (longest axis) prepared using 14% THF in ethanol at 90 °C for 4 hours, followed by cooling to room temperature and ageing for 1 day. Sample was stained with 1 wt. % uranyl acetate in water. Scale bar = 10 µm. ........ 221

**Figure 4.26** Fluorescence microscopy images of emulsion droplets prepared with large (left) and small (right) diamond platelets after 60 minutes at 0.5 wt. % using 0.01 wt. % fluorescein-labelled dextran, where the green colour indicates the dextran-rich phase. Note that the use of dyes produces a larger droplet size, hence non-dye tagged polymers were used for the reported calculations. Scale bar = 200 µm. ........ 223

**Figure 4.27** Overlaid refractive index SEC chromatograms (using 80:20 water:methanol as the eluent) for dextran and FITC-dextran polymers.[§] ........ 223

**Figure 4.28** Emulsion droplet diameter using (a) large diamond platelets (prepared with 12% THF) and (b) small diamond platelets (prepared with 0% THF) as a function of time. 225

**Figure 4.29** Optical microscopy images of Pickering emulsions at different time points using small diamond platelets (prepared with 0% THF) at (a) 0.05, (b) 0.1, (c) 0.2, (d) 0.3, (e) 0.4 and (f) 0.5 wt. %. Scale bar = 100 µm. 226

**Figure 4.30** Optical microscopy images of Pickering emulsions at different time points using large diamond platelets (prepared with 12% THF) at (a) 0.05, (b) 0.1, (c) 0.2 and (d) 0.3 wt. %. Scale bar = 100 µm. 227

**Figure 4.31** TEM micrograph of $PLLA_{36}$-*b*-$PDMAEMA_{216}$ spherical micelles. Samples were stained with 1 wt. % uranyl acetate in water. Scale bar = 1 µm. 227

**Figure 4.32** Optical microscopy images of Pickering emulsions at different time points prepared using spherical micelles at 3 wt. %. Scale bar = 100 µm. 228

**Figure 4.33** Optical microscopy images of Pickering emulsions at different time points using large diamond platelets (prepared with 12% THF) at (a) 0.4 and (b) 0.5 wt. %. Scale bar = 100 µm. 230

**Figure 4.34** Plot showing the decrease in emulsion droplet diameter with increasing concentration using large diamond platelets at 5, 10 and 15 minutes. Effect of small and large platelets on particle coverage of the droplets. Error bars indicate the standard deviation in droplet diameter when counting *ca.* 100 droplets. 231

**Figure 4.35** Optical microscopy images of Pickering emulsions at different time points using small diamond platelets (prepared with 0% THF) at a higher loading of 1 wt. %. Scale bar = 100 µm. 232

**Figure 4.36** Optical microscopy images of Pickering emulsions (10% dextran, 2% PEG for a PEG in dextran emulsion) at different time points using large diamond platelets (prepared with 12% THF) at 0.5 wt. %. Scale bar = 100 µm. .................. 232

**Figure 4.37** $^1$H NMR spectra (400 MHz, $D_2O$) of the quaternised polymer in comparison to the original $PLLA_{36}$-*b*-$PDMAEMA_{216}$. .......................................... 234

**Figure 4.38** $^1$H NMR spectra (400 MHz, $CDCl_3$) of the zwitterionic-modified polymer in comparison to the original $PLLA_{36}$-*b*-$PDMAEMA_{216}$. ......................... 234

**Figure 4.39** TEM micrographs of $PLLA_{36}$-*b*-$PDMAEMA_{216}$ quaternised platelets prepared using (a) 0% THF and (b) 12% THF and modified $PLLA_{36}$-*b*-$PDMAEMA_{216}$ zwitterionic platelets prepared using (c) 0% THF and (d) 12% THF. Differences in image contrast can be accounted for differences in staining with 1 wt. % uranyl acetate in water. Scale bar = 1 µm. ......................................................... 235

**Figure 4.40** Optical microscopy images of Pickering emulsions at different time points using diamond nanoplatelets prepared with (a) small and (b) large quaternised $PLLA_{36}$-*b*-$PDMAEMA_{216}$ and (c) small and (d) large zwitterionic modified $PLLA_{36}$-*b*-$PDMAEMA_{216}$ at 0.3 wt. %. Scale bar = 100 µm. ................................ 236

**Figure 4.41** Optical microscopy images of Pickering emulsions at different time points using diamond nanoplatelets prepared with (a) small and (b) large quaternised $PLLA_{36}$-*b*-$PDMAEMA_{216}$ and (c) small and (d) large zwitterionic modified $PLLA_{36}$-*b*-$PDMAEMA_{216}$ at 0.5 wt. %. Scale bar = 100 µm. (e) Plot comparing emulsion droplet diameter using large quaternised, zwitterionic and neutral platelets at 0.5 wt. % loading. Error bars indicate the standard deviation in measured droplet diameter when counting *ca.* 50 droplets. ................................................................ 237

**Figure 4.42** Photograph of phase-separated Pickering emulsions using large quaternised $PLLA_{36}$-*b*-$PDMAEMA_{216}$ platelets (left) and large neutral platelets (right), indicating the upper PEG-rich phase and the lower dextran-rich phase. The cloudy, blue phases indicate the presence of the platelets, where the quaternised platelets reside in the dextran-rich phase and the neutral platelets reside in the PEG-rich phase. ........ 240

**Figure 4.43** SEC chromatogram of PLLA$_{36}$-*b*-PDMAEMA$_{216}$ modified by removing the RAFT end group using DMF with 0.1% LiBr as an eluent with PMMA standards. ........ 241

**Figure 4.44** TEM micrographs of PLLA$_{36}$-*b*-PDMAEMA$_{216}$ platelets modified by removing the RAFT-end group prepared using (a) 12% THF and (b) 10% THF. Differences in image contrast can be accounted for by differences in sample staining with 1 wt. % uranyl acetate in water. Scale bar = 1 µm........ 242

**Figure 4.45** Optical microscopy images of Pickering emulsions at different time points using 0.5 wt. % diamond nanoplatelets prepared with RAFT end group removed PLLA$_{36}$-*b*-PDMAEMA$_{216}$. Scale bar = 100 µm........ 242

**Figure 4.46** Photograph of phase-separated Pickering emulsions using large end-group removed PLLA$_{36}$-*b*-PDMAEMA$_{216}$ platelets (left) and large neutral platelets (right), indicating the upper PEG-rich phase and the lower dextran-rich phase. The cloudy blue phases indicate the presence of the platelets, where the end-group removed platelets reside in the dextran-rich phase and the neutral platelets reside in the PEG-rich phase. ........ 243

**Figure 4.47** Equilibrium flow curves of PEG-rich and dextran-rich phases, prepared at 4% PEG and 5% dextran in water, shaken for two minutes and allowed to phase separate........ 253

**Figure 4.48** Comparison of the relative change in length, L, (of the longest axis) of deformed droplets of PEG/dextran emulsions using (a) no platelets, (b) large platelets (prepared with 12 % THF) and (c) small platelets (prepared with (0% THF)). The deformation of three droplets was measured and recorded for each emulsion. ....... 254

**Figure 4.49** Comparison of the relative change in length, L, (of the longest axis) of deformed droplets of PEG/dextran emulsions using large zwitterionic platelets (prepared with 12 % THF). The deformation of three droplets was measured and recorded. ........ 254

**Figure 5.1** Effect of nanoparticle morphology on the likelihood of cellular uptake by contact with the blood vessel walls.[11] ........ 266

**Figure 5.2** Examples of hierarchical structures by Manners and co-workers. (a) Scarf-like micelles,[28] (b) branched micelles,[27] (c) multi-arm micelles[29] and (d) platelet micelles.[23] ........ 268

**Figure 5.3** (a) Method for the preparation of water-stable cylindrical micelles, where the cylindrical micelles are first prepared in DMF/tetrahydrofuran (THF), followed by sonication in DMF to form seed micelles and subsequent growth to form monodisperse cylinders before dialysis into water. (b) Plot showing the linear dependence of cylinder length on the unimer to seed ratio. (b) Structure of the PFS-*b*-poly(allyl glycidyl ether) block copolymer grafted with TEG.[18] ........ 269

**Figure 5.4** Growth regimes and time-scales for the preparation of PEO-*b*-PCL cylinders *via* fast unimer addition and slow end-to-end coupling.[49] ........ 271

**Figure 5.5** $^1$H NMR spectrum ($CDCl_3$, 400 MHz) of $PCL_{50}$. ........ 273

**Figure 5.6** Overlaid RI and UV ($\lambda$ = 309 nm) SEC chromatograms of $PCL_{50}$ using DMF with 0.1% LiBr as an eluent with poly(methyl methacrylate) (PMMA) standards. ........ 274

**Figure 5.7** MALDI-ToF mass spectrum of $PCL_{50}$, showing a m/z difference of 114.14 equivalent to one PCL unit and therefore minimal transesterification. ....... 275

**Figure 5.8** Differential scanning calorimetry thermograms of $PCL_{50}$ measured at a heating and cooling rate of 2 °C per minute. ........................................................ 276

**Figure 5.9** $^1$H NMR spectrum ($CDCl_3$, 400 MHz) of $PCL_{50}$-*b*-$PDMA_{180}$. ............ 277

**Figure 5.10** Overlaid RI and UV ($\lambda$ = 309 nm) SEC chromatograms of $PCL_{50}$-*b*-$PDMA_{180}$ in comparison with $PCL_{50}$ homopolymer using DMF with 0.1% LiBr as an eluent with PMMA standards. ............................................................ 277

**Figure 5.11** DOSY NMR spectrum (500 MHz, $CDCl_3$) of $PCL_{50}$-*b*-$PDMA_{180}$...... 278

**Figure 5.12** TEM micrographs of cylindrical micelles prepared using $PCL_{50}$-*b*-$PDMA_{180}$ by self-nucleation in ethanol, heating at 70 ˚C for 3 hours and subsequently cooling down to room temperature. (a) Cylinders aged for 1 day, stained with 1 wt. % uranyl acetate in water. Scale bar = 1 µm. (b), (c) Cylinders aged for 5 days, (b) stained with 1 wt. % uranyl acetate in water. Scale bar = 2 µm. (c) Imaged on a GO grid. Scale bar = 1 µm. ......................................................... 279

**Figure 5.13** (a) Selected area electron diffraction (SAED) pattern$^§$ of a single $PCL_{50}$-*b*-$PDMA_{180}$ cylinder. The crystal structure measured from the diffraction patterns has lattice parameters 0.37 ± 0.01 nm by 0.56 ± 0.01 nm, with a lattice angle of 124.1 ± 0.1˚. (b) Wide angle X-ray diffractogram of $PCL_{50}$-*b*-$PDMA_{180}$ cylinders showing the $2\theta$ peaks at *ca.* 21˚ and 24˚ characteristic of crystalline PCL. .......................... 279

**Figure 5.14** TEM micrographs of $PCL_{50}$-*b*-$PDMA_{180}$ cylinders assembled in ethanol after sonication at 0 °C using an ultrasound bath. Cylinders were sonicated for (a) 10, (b) 20, (c) 40 and (d) 60 minutes without ageing and imaged on a GO grid. Scale bar = 1000 nm. Cylinders were sonicated for (e) 10, (f) 20, (g) 40 and (h) 60 minutes and aged for 7 days. Samples were stained with uranyl acetate. Scale bar = 1000 nm. . 281

**Figure 5.15** Histograms of cylinder length at 20 minutes and 60 minutes sonication using an ice water ultrasound bath after ageing for 7 days. .................................... 281

**Figure 5.16** TEM micrographs of PCL$_{50}$-*b*-PDMA$_{180}$ cylinders assembled in ethanol after sonication at 0 °C using a sonic probe at (a) 1, (b) 3, (c) 5, (d) 10, (e) 15 and (d) 20 minutes. 1% uranyl acetate was used as negative stain. Scale bar = 1000 nm. .. 282

**Figure 5.17** Histogram showing the length distribution of sonicated cylinders, obtained after 10, 15 and 20 minutes of sonication at 0 °C using a sonic probe and a jitter box plot of the length distribution of seed micelles obtained after 20 minutes of sonication (inset). ........ 283

**Figure 5.18** Overlaid RI SEC chromatograms of PCL$_{50}$-*b*-PDMA$_{180}$ before self-assembly (solid black line), after heating at 70˚C for 3 hours (dashed blue line) and after sonication of the cylindrical micelles for 20 minutes at 0˚C using a sonic probe (dashed red line) using DMF with 0.1% LiBr as an eluent with PMMA standards. 284

**Figure 5.19** Photograph of dispersed cylindrical micelles at different unimer to seed ratios, at the same concentration in ethanol, epitaxially grown from seed micelles, showing an increase in turbidity due to the presence of increasingly larger structures. ........ 285

**Figure 5.20** TEM micrographs of cylindrical micelles epitaxially grown from seed micelles with a unimer/seed ratio of (b) 1, (c) 2, (d) 3, (e) 5, (f) 7 and (g) 9. 1% uranyl acetate was used as negative stain. Scale bar = 1000 nm. ........ 286

**Figure 5.21** Plot showing a linear epitaxial growth regime of PCL$_{50}$-*b*-PDMA$_{180}$ cylinders with narrow length dispersities (error bars represent the standard deviation, σ, of the length distribution) in comparison to the theoretical length (dashed line) Cylinders were grown from *ca.* 50 nm seeds. ........ 286

**Figure 5.22** Overlaid RI and UV ($\lambda$ = 309 nm) SEC chromatograms of PCL$_{50}$-*b*-PDMA$_{180}$ end group modified with acrylic acid using DMF with 0.1% LiBr as an eluent with PMMA standards. ........ 289

**Figure 5.23** TEM micrograph of end-group modified PCL$_{50}$-*b*-PDMA$_{180}$ heated at 70 ˚C for 3 hours and subsequently cooled down to room temperature. Stained with uranyl acetate. Scale bar = 1000 nm. ...................................................................... 290

**Figure 5.24** $^1$H NMR spectrum (CDCl$_3$, 400 MHz) of PCL$_{50}$-*b*-PMMA$_{20}$. ............ 291

**Figure 5.25** $^1$H NMR spectrum (CDCl$_3$, 400 MHz) of PCL$_{50}$-*b*- PMMA$_{20}$-*b*-PDMA$_{200}$. ........................................................................................................ 292

**Figure 5.26** Overlaid RI SEC chromatograms of PCL$_{50}$, PCL$_{50}$-*b*-PMMA$_{20}$ and PCL$_{50}$-*b*-PMMA$_{20}$-*b*-PDMA$_{200}$ using DMF with 0.1% LiBr as an eluent with PMMA standards.......................................................................................................... 292

**Figure 5.27** DOSY NMR spectrum (500 MHz, CDCl$_3$) of PCL$_{50}$-*b*-PMMA$_{20}$-*b*-PDMA$_{200}$. ........................................................................................................ 293

**Figure 5.28** TEM micrograph of cylindrical micelles prepared using PCL$_{50}$-*b*-PMMA$_{20}$-*b*-PDMA$_{200}$ by self-nucleation in (a) ethanol and (b) from THF into water, heated at 70 ˚C for 3 hours and subsequently cooled down to room temperature. Sample was aged 2 weeks. (c) TEM micrograph of PCL$_{50}$-*b*-PMMA$_{20}$-*b*-PDMA$_{200}$.cylinders sonicated in water for 5 minutes to produce seed micelles. 1% uranyl acetate was used as negative stain. Scale bar = 1000 nm.§ .......................... 294

**Figure 5.29** Wide angle X-ray diffractogram of PCL$_{50}$-*b*-PDMA$_{180}$ cylinders showing the 2$\theta$ peaks at *ca.* 21˚ and 24˚ characteristic of crystalline PCL. ............ 295

**Figure 5.30** Cryo-TEM micrographs of PCL$_{50}$-*b*-PMMA$_{20}$-*b*-PDMA$_{200}$ cylindrical micelles (a) before and (b) after sonication. (c) Diameter distribution of sonicated micelles. Scale bar = 200 nm.§ ...................................................................... 295

**Figure 5.31** TEM micrographs of cylindrical micelles epitaxially grown from seed micelles in water with a unimer/seed ratio of (a) 1, (b) 5, (c) 9, (d) 15, using graphene oxide TEM grids. Scale bar = 1000 nm.§ ................................................................ 296

**Figure 5.32** Plot showing a linear epitaxial growth regime of $PCL_{50}$-*b*-$PMMA_{20}$-*b*-$PDMA_{180}$ cylinders with narrow length dispersities (error bars represent the σ of the length distribution) in comparison to the theoretical length (dashed line). .............. 297

**Figure 5.33** Viability over 24 and 72 hours of (a) MC3T3 and (b) A549 using concentrations of $PCL_{50}$-*b*-$PMMA_{20}$-*b*-$PDMA_{200}$ from 0 to 5 mg $mL^{-1}$.[§] .............. 298

**Figure 5.34** Strain-dependent oscillatory rheology of the cylinder hydrogel at 293 K and a constant frequency of 10 rad $s^{-1}$. .............. 299

**Figure 5.35** (a) Step-strain measurements of cylinder hydrogel over three cycles (ω = 10 rad $s^{-1}$) with (b) close up of the recovery of the material properties after each cycle. .............. 300

**Figure 5.36** (a) TEM micrograph of $PCL_{50}$-*b*-$PMMA_{20}$-*b*-$PDMA_{200}$ hydrogel freeze dried on a TEM grid. Scale bar = 1000 nm. (b) Cryo-SEM image of the cylinder hydrogel (scale bar = 2 μm) with a photograph of the hydrogel (inset). .............. 300

**Figure 5.37** TEM micrograph of $PCL_{50}$-*b*-$PMMA_{20}$-*b*-$PDMA_{200}$ fragmented cylinders obtained by re-suspension of the cylinder hydrogel in water, imaged using a graphene oxide (GO) grid. Scale bar = 2 μm. .............. 301

**Figure 5.38** Confocal microscopy images of (a) MC3T3 and (b) A549 cells after 4 days encapsulation in a $PCL_{50}$-*b*-$PMMA_{20}$-*b*-$PDMA_{200}$ hydrogel. Cells were stained with live/dead viability kit, where green indicates live cells and red indicates dead cells. Scale bar = 200 μm.[§] .............. 302

**Figure 5.39** $^1H$ NMR spectrum ($CDCl_3$, 400 MHz) of $PCL_{50}$-*b*-$PDMAEMA_{170}$. .. 304

**Figure 5.40** Overlaid RI and UV ($\lambda$ = 309 nm) SEC chromatograms of $PCL_{50}$-*b*-$PDMAEMA_{170}$ in comparison with $PCL_{50}$ homopolymer using DMF with 0.1% LiBr as an eluent with PMMA standards. .............. 304

**Figure 5.41** Self nucleation of PCL$_{50}$-*b*-PDMAEMA$_{170}$ by heating at 90 °C for 4 hours in (a) *n*-propanol and (b) *n*-butanol at 5 mg mL$^{-1}$ and (c) ethanol at 1 mg mL$^{-1}$. Samples were stained with uranyl acetate. Scale bar = 1000 nm. .......................... 305

**Figure 5.42** TEM micrographs of PCL$_{50}$-*b*-PDMAEMA$_{170}$ platelet micelles epitaxially grown from PCL$_{50}$-*b*-PDMA$_{180}$ seed micelles with a unimer/seed ratio of (a) 5, (b) 10 and (c) 20. 1% uranyl acetate was used as negative stain. Scale bar = 1000 nm. .......................... 306

**Figure 5.43** Plot showing a linear epitaxial growth regime of PCL$_{50}$-*b*-PMMA$_{20}$-*b*-PDMA$_{180}$ cylinders with narrow length dispersities (error bars represent the standard deviation σ of the length distribution) in comparison to the theoretical length (dashed line). .......................... 307

**Figure 5.44** WAXD diffractogram of a PCL$_{50}$-*b*-PDMAEMA$_{170}$ platelets, showing the 2$\theta$ peaks at *ca.* 21° and 24° characteristic of crystalline PCL. .......................... 307

**Figure 5.45** Confocal microscopy images of fluorescent ABM ring platelet micelles with (a) one ABM unimer addition and (b) two ABM unimer additions. Scale bar = 1000 nm.§ .......................... 308

**Figure 5.46** TEM micrographs of PCL$_{50}$-*b*-PDMAEMA$_{170}$ platelet micelles (a) before and (b) after addition of PCL$_{50}$-*b*-PDMA$_{180}$ unimers in THF to form hybrid micelles. Samples were stained with uranyl acetate. Scale bar = 1000 nm. .......................... 309

**Figure 5.47** TEM micrograph of pure platelet micelles prepared by addition of PDMA$_{250}$-*b*-PCL$_{60}$-*b*-PDMA$_{250}$ unimers to PCL$_{50}$-*b*-PDMAEMA$_{170}$ platelet micelles. Samples were stained with uranyl acetate. Scale bar = 1000 nm.§ .......................... 310

# *List of Schemes*

**Scheme 1.1** Schematic of the key mechanistic steps in free radical polymerisation... 5

**Scheme 1.2** Schematic of the key activation/deactivation step by a transition metal complex in ATRP, where M represents a transition metal complex, X represents a halide and M represents a monomer species. ........................................................... 8

**Scheme 1.3** Schematic of the key activation/deactivation step by a nitroxide in NMP. ....................................................................................................................... 8

**Scheme 1.4** Mechanism of RAFT polymerisation. ................................................. 10

**Scheme 1.5** Schematic of a typical end group modification process of a trithiocarbonate with an acrylate. .................................................................... 13

**Scheme 1.6** A typical self-nucleation process, where a polymer is heated to form molecularly dissolved unimers and cooled to form assembled structures. ................ 23

**Scheme 1.7** A typical epitaxial growth process, where molecularly dissolved unimers are added to pre-formed crystalline seeds to grow the assembled structures. ........... 24

**Scheme 1.8** A typical self-seeding process, where a polymer is heated until few crystalline regions remain and cooled to form assembled structures. ........................ 26

**Scheme 1.9** An example of a morphological transition, where a change in conditions allows a change from spherical to cylindrical assembled structures. ......................... 27

**Scheme 2.1** Two-step synthesis of the pro-cationic monomer, AEANBoc. ............. 57

**Scheme 2.2** Synthesis of PLLA homopolymer, followed by PLLA-*b*-PAEANBoc diblock copolymer and subsequent deprotection to form PLLA-*b*-PAEA using a dual-functional ROP initiator and RAFT chain transfer agent. ................................ 60

**Scheme 2.3** Synthesis of PLLA homopolymer, followed by PLLA-*b*-PDMA diblock copolymer using a dual-functional ROP initiator and RAFT chain transfer agent.... 75

**Scheme 2.4** Solvation-driven shape selectivity mechanism (using an arbitrary scale to represent sequential processes on cooling from 90 °C to 20 °C) for PLLA$_{48}$-*b*-PDMA$_{m}$ block copolymers of block ratios 1:20 (platelet-forming, m = 1000) and 1:3 (cylinder-forming, m = 150), where $T_{\mathrm{Agg1:3}}$ represents aggregation of the 1:3 block ratio cylinder-forming block copolymer. ................................................................ 84

**Scheme 2.5** Modifications of the RAFT end group of a PLLA$_{36}$-*b*-PDMA$_{245}$ block copolymer to form either amine-functionalised or acid-functionalised polymers. .... 85

**Scheme 2.6** Solvation-driven shape selectivity mechanism (using an arbitrary scale to represent sequential processes on cooling from 90 °C to 20 °C) for PLLA$_{48}$-*b*-PDMA$_{m}$ block copolymers of block ratios (a) 1:20 (platelet-forming, m = 1000); (b) a mixture of 1:20 and 1:3 and (c) 1:3 (cylinder-forming, m = 150), where $T_{\mathrm{Agg1:3}}$ represents aggregation of the 1:3 block ratio cylinder-forming block copolymer. .... 88

**Scheme 3.1** Physical cross-linking of alginate polymer chains with divalent calcium ions to form a crosslinked hydrogel structure. ....................................................... 117

**Scheme 3.2** Synthesis of PLLA-*b*-PDMAEMA using the ethyl-terminated chain transfer agent suitable for polymerising methacrylates. ......................................... 125

**Scheme 3.3** Synthesis and crystallisation-driven self-assembly of PLLA-*b*-PTHPA block copolymers to form PLLA-*b*-PAA cylindrical micelles. .............................. 139

**Scheme 3.4** Amidation of PLLA$_{36}$-*b*-PAA$_{400}$ cylindrical micelles in water to form pseudo PLLA$_{36}$-*b*-PDMAEA$_{400}$ cylindrical micelles. Note that the reaction forms an acrylamide corona. ........................................................................................ 145

**Scheme 3.5** Hydrolysis of GDL and subsequent reactions with $CaCO_3$. ................ 149

**Scheme 3.6** Preparation of nanocomposite hydrogels using spherical, cylindrical and diamond-platelet composite materials.................................................................. 152

**Scheme 3.7** Representation of alginate gel block adhesion with diamond-platelet nanoparticles as an adhesive. .................... 173

**Scheme 4.1** Synthesis of PLLA homopolymer by ROP, followed by RAFT polymerisation of DMAEMA to form a PLLA-*b*-PDMAEMA diblock copolymer using a dual-functional ROP initiator and chain transfer agent. .................... 204

**Scheme 4.2** A crystallised PLLA-*b*-PDMAEMA polymer chain within a diamond-shaped platelet, showing an arbitrary representation of the chain-folded core block and the spacing of the corona chain. .................... 216

**Scheme 4.3** (a) Quaternisation and (b) zwitterionic functionalisation of PLLA$_{36}$-*b*-PDMAEMA$_{216}$. .................... 233

**Scheme 4.4** Removal of the RAFT end group of PLLA$_{36}$-*b*-PDMAEMA$_{216}$ to produce a hydrogen-terminated polymer before self-assembly into diamond-shaped platelets. .................... 240

**Scheme 5.1** Synthesis of PCL$_{50}$-*b*-PDMA$_{180}$ block copolymer by ROP and RAFT polymerisation. .................... 272

**Scheme 5.2** Schematic of self-nucleation of PCL$_{50}$-*b*-PDMA$_{180}$ diblock copolymer at 5 mg mL$^{-1}$ in ethanol, heating at 70 °C for 3 hours, followed by sonication of polydisperse cylinders to form uniform seed micelles. .................... 280

**Scheme 5.3** Schematic of epitaxial growth of PCL$_{50}$-*b*-PDMA$_{180}$ cylindrical micelles in ethanol from *ca.* 50 nm seeds. Seeds were used at 0.01 mg mL$^{-1}$ in ethanol, with addition of unimers at 10 mg mL$^{-1}$ in THF. .................... 285

**Scheme 5.4** Modification of the RAFT end group of a PCL$_{50}$-*b*-PDMA$_{180}$ block copolymer with a single carboxylic acid group. .................... 288

**Scheme 5.5** Schematic of epitaxial growth of PCL$_{50}$-*b*-PMMA$_{20}$-*b*-PDMA$_{180}$ cylindrical micelles in water from seed micelles. .................... 296

**Scheme 5.6** Schematic of hydrogel formation *via* direct epitaxial growth of PCL$_{50}$-*b*-PMMA$_{20}$-*b*-PDMA$_{200}$ cylinders in water. ........ 299

**Scheme 5.7** Synthesis of PCL$_{50}$-*b*-PDMAEMA$_{170}$ block copolymer by ROP and RAFT polymerisation. ........ 303

**Scheme 5.8** Schematic of epitaxial growth of PCL$_{50}$-*b*-PDMAEMA$_{170}$ platelet micelles in ethanol from 50 nm PCL$_{50}$-*b*-PDMA$_{180}$ seeds. ........ 306

**Scheme 5.9** (a) Structure of the PCL$_{50}$-*b*-PDMAEMA$_{170}$ polymer prepared using an ABM chain transfer agent. (b) Schematic diagram representing concentric growth of the ABM polymer (yellow interface with purple corona) from a PCL$_{50}$-*b*-PDMA$_{180}$ seed (blue corona), where the ABM lies at the core-corona interface, obtained by an epitaxial growth mechanism.§ ........ 308

**Scheme 5.10** Epitaxial growth starting from seed micelles to form platelets, followed by cylinder growth from the platelets to form hybrid micelles. ........ 309

**Scheme 5.11** Epitaxial growth starting from seed micelles to form platelets, followed by platelet growth using triblock copolymers. ........ 310

# List of Tables

**Table 2.1** Characterisation of PLLA polymers. ........................................................ 60

**Table 2.2** Characterisation of $PLLA_{36}$-*b*-$PAEA_{295}$ spherical micelles. ..................... 67

**Table 2.3** Attempts at crystallisation-driven self-assembly of $PLLA_{36}$-*b*-$PAEA_{295}$ in 1:1 DMF/$H_2O$ mixtures. ........................................................................................ 68

**Table 2.4** Characterisation of $PLLA_{48}$-*b*-$PDMA_n$ polymers. .................................... 74

**Table 2.5** Characterisation of attached cylindrical micelles within hierarchical structures. ........................................................................................................ 89

**Table 3.1** Characterisation of PLLA polymers. ...................................................... 125

**Table 3.2** Characterisation of $PLLA_{36}$-*b*-$PDMAEMA_{216}$ micelles. ........................ 132

**Table 3.3** Attempts at crystallisation-driven self-assembly of $PLLA_{36}$-*b*-$PDMAEMA_{216}$ in a 1:1 DMF:$H_2O$ mixture at 1 mg $mL^{-1}$. ..................................... 133

**Table 3.4** Crystallisation-driven self-assembly of $PLLA_{36}$-*b*-$PDMAEMA_{216}$ in alcoholic solvents at a total concentration of 5 mg $mL^{-1}$. ....................................... 134

**Table 3.5** Characterisation of PLLA polymers. ...................................................... 140

**Table 3.6** Zeta potential measurements of $PLLA_{36}$-*b*-$PAA_{400}$ cylindrical micelles before and after amidation. .......................................................................... 145

**Table 3.7** Summary of the particles used as composites in alginate hydrogels. ..... 148

**Table 3.8** Calcium alginate gel formulations at 1.5 wt. % sodium alginate in water. ......................................................................................................... 150

**Table 3.9** Calcium alginate gel formulations with $PLLA_{36}$-*b*-$PAA_{400}$ at 1.5 wt. % sodium alginate in water. ............................................................................ 153

**Table 3.10** Calcium alginate gel formulations with $PLLA_{36}$-*b*-$PAEA_{295}$ at 1.5 wt. % sodium alginate in water. ............................................................................ 161

**Table 3.11** Initial calcium alginate gel formulations with PLLA$_{36}$-*b*-PDMAEMA$_{216}$ at 1.5 wt. % sodium alginate in water. .................................................................... 164

**Table 3.12** Revised calcium alginate gel formulations with PLLA$_{36}$-*b*-PDMAEMA$_{216}$ at 1.5 wt. % sodium alginate in water. .......................................... 167

**Table 4.1** Characterisation of PLLA$_{90}$ polymers. ................................................. 204

**Table 4.2** Characterisation of PLLA-*b*-PDMAEMA diblock copolymers. ............ 209

**Table 4.3** Zeta potentials of diamond platelets measured in water at pH 6.5.......... 213

**Table 4.4** Adsorption of PEG and dextran on PLLA$_{36}$-*b*-PDMAEMA$_{216}$ platelets (prepared with 0% THF) dispersed in water. Average values are reported along with the standard deviation of five measurements. ......................................................... 222

**Table 4.5** Average interfacial tension, γ, of PEG/dextran phases using PLLA$_{36}$-*b*-PDMAEMA$_{216}$ small nanoplatelets (prepared with 0% THF) and large platelets (prepared with 12% THF) as emulsifiers. ................................................ 229

**Table 4.6** Zeta potentials of PLLA$_{36}$-*b*-PDMAEMA$_{216}$ diamond platelets. ............ 235

**Table 4.7** Average interfacial tension, γ, of PEG/dextran phases emulsified using PLLA$_{36}$-*b*-PDMAEMA$_{216}$ large nanoplatelets (prepared with 12% THF) modified to exhibit a zwitterionic corona. ....................................................................... 238

**Table 4.8** Adsorption of PEG and dextran on quaternised and zwitterionic PLLA$_{36}$-*b*-PDMAEMA$_{216}$ platelets (prepared with 0% THF) dispersed in water. Average values are reported along with the standard deviation of five measurements. ........................................................................................................................ 239

**Table 4.9** Parameters calculated for interfacial tension, γ, of PEG/dextran phases using PLLA$_{36}$-*b*-PDMAEMA$_{216}$ small nanoplatelets (prepared with 0% THF) and large platelets (prepared with 12% THF) using droplet relaxation time and capillary time. ....................................................................................................... 255

**Table 5.1** Characterisation of PCL polymers. ........................................................ 273

**Table 5.2** Length distribution for cylinders formed upon sonication of $PCL_{50}$-*b*-$PDMA_{180}$ cylindrical micelles at 0 °C using a sonic probe. .................................... 283

**Table 5.3** Length dispersity of cylinders formed upon epitaxial growth of $PCL_{50}$-*b*-$PDMA_{180}$ cylindrical micelles. .................................................................. 287

**Table 5.4** Length dispersity of cylinders formed upon epitaxial growth of $PCL_{50}$-*b*-$PMMA_{20}$-*b*-$PDMA_{180}$ cylindrical micelles. ............................................................ 297

**Table 5.5** Characterisation of PCL polymers. ........................................................ 303

**Table 5.6** Calculations for epitaxial growth of $PCL_{50}$-*b*-$PDMA_{180}$ cylindrical micelles (2.5 mg) in ethanol (2 mL), adding unimers in a constant amount of THF (0.05 mL). ........................................................................................................ 318

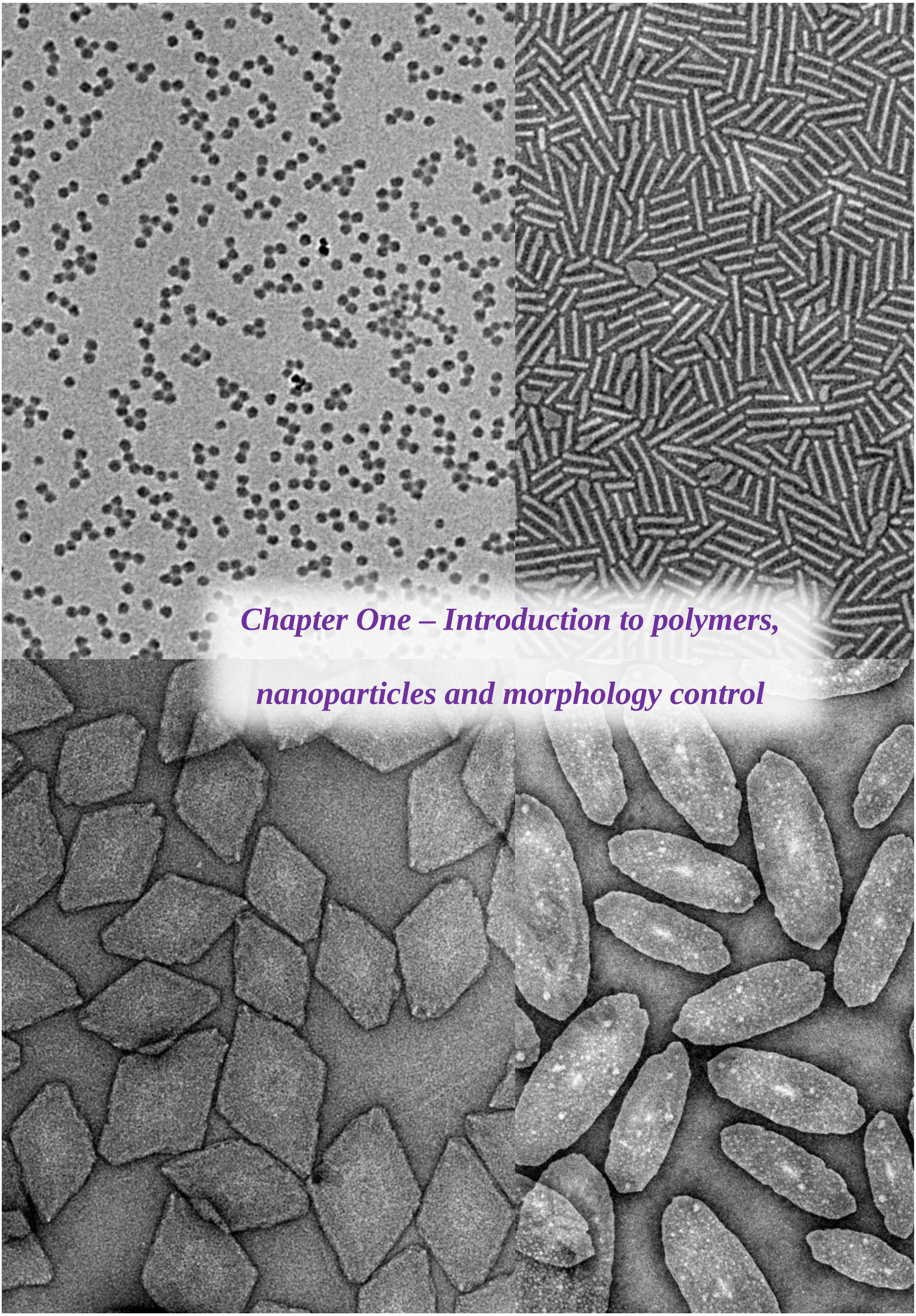

# Chapter One – Introduction to polymers, nanoparticles and morphology control

## *1.1 Morphology in nature*

In natural nanomaterials, shape is a key factor in enabling a range of highly complex functionalities with an exquisite degree of selectivity, precision and efficiency. Perhaps most notably is the three-dimensional structure of a folded protein, which is vital in creating highly specific active sites which allow particular functions to take place. On a larger scale, unique morphologies are often displayed by natural pathogens, from icosahedral *Hepatitis A virions*, to micron-sized, worm-shaped *Ebola virions* and the unique head-tail structure of bacteriophages. Such geometries can dictate their ability to infect specific cell types and may alter their residence time inside the cell. Nature has designed these nanostructures with the utmost complexity, where the combination of shape, size and composition is crucial in mediating their specific interactions and functions.

Soft nanomaterials offer great potential in the desire to emulate such properties through synthetic tailoring of nanoparticle constructs.[1] Achieving the same degree of control over a combination of both composition and morphology is an interesting challenge that has been of particular interest over recent years.[2-4] In order to engineer these highly complex materials with the desired functionality, each hierarchical level of synthetic modification can be considered, from the synthetic preparation and modification of macromolecular species to the design of new and innovative assembly methods.[5] These macromolecules can encompass natural building blocks, such as nucleic acids, where the high specificity of Watson-Crick base pairing interactions can be exploited for the formation of nanoscale assemblies, or synthetic building blocks, such as polymers, which use a wide array of interactions and functionalities to fabricate assemblies from the nano- to macro-scale and beyond.

## 1.2 *Synthetic polymer building blocks*

Synthetic polymers offer an ever-expanding range of functional materials with many variables that must be considered in order to produce reliable constructs. In addition to monomer type, the way the monomers are connected and the overall topology of the polymer are important attributes of the resultant material. Overall, the functionality, architecture and composition, comprising sequence, tacticity and molecular weight, form the main components which can be modulated to impart a wide range of desired properties to the fabricated construct (**Figure 1.1**).[6]

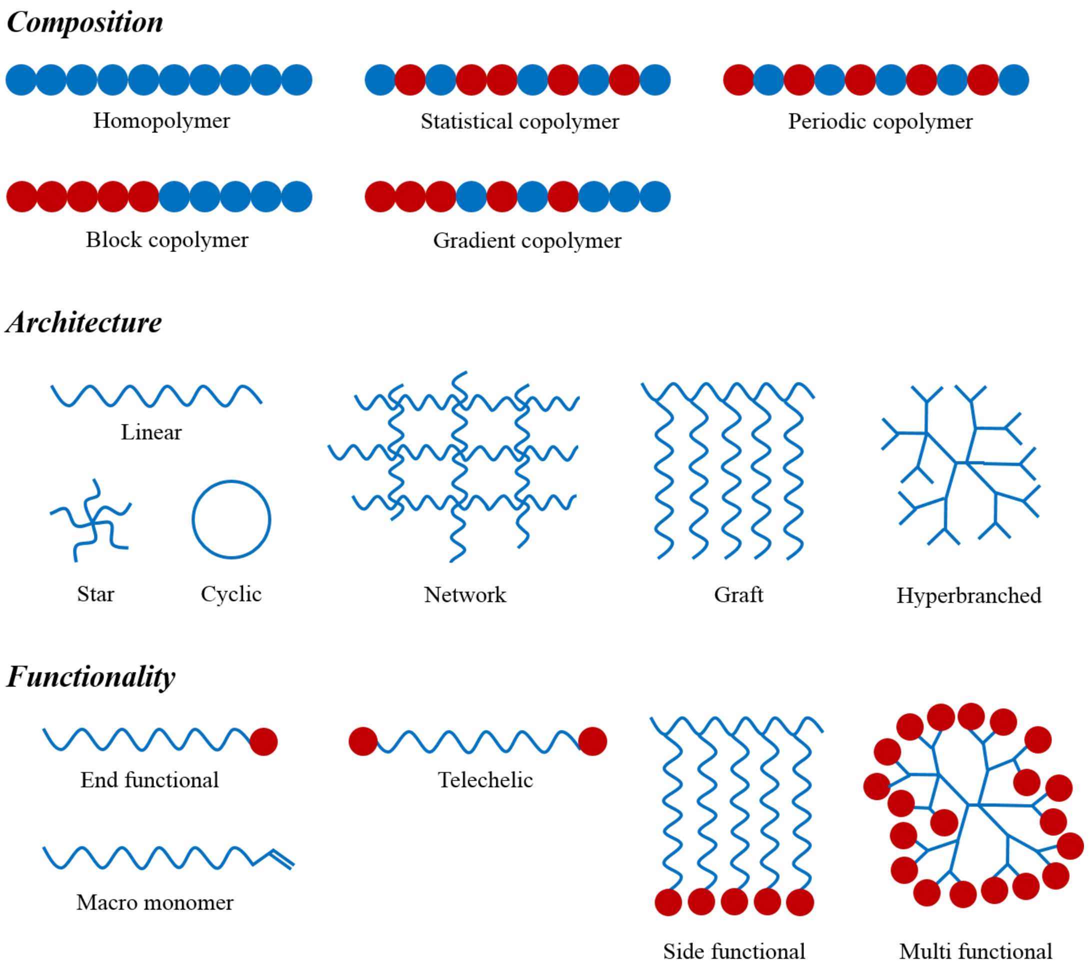
Composition
Homopolymer
Statistical copolymer
Periodic copolymer
Block copolymer
Gradient copolymer
Architecture
Linear
Star
Cyclic
Network
Graft
Hyperbranched
Functionality
End functional
Telechelic
Macro monomer
Side functional
Multi functional

**Figure 1.1** The main components of a polymer which can be used to change the resultant properties of the material, where blue and red indicate different monomers.

Polymer architecture can be controlled by careful choice of the method of polymerisation, however, precise control over polymer composition is principally targeted using living polymerisation and reversible-deactivation radical polymerisation mechanisms.

### *1.2.1 Free radical polymerisation*

Currently, one of the most predominant methods in the industrial synthesis of polymers is free radical polymerisation. Largely, this is due to the ability of free radical polymerisation to incorporate a wide range of unprotected functional groups using comparatively mild reaction conditions, leading to a relatively simple and inexpensive technique.[7] The mechanism of free radical polymerisation can be described by four principal steps; initiation, propagation, chain transfer and termination. Initiation describes the formation of free radicals by decomposition of an initiator molecule by, for example, thermal or radiative processes. The initiator fragment reacts with the monomer to begin the conversion to a polymer, followed by successive monomer additions in the propagation step. Chain transfer denotes a process where the radical species can be transferred from one polymer chain to, for example, another polymer chain, often leading to the formation of branched architectures. The radical species may also transfer to a monomer, the solvent or an added chain transfer agent, such as a thiol. Termination describes the removal of a radical species through an irreversible reaction. This can occur through recombination, where two active radicals couple together to deactivate polymer growth; or disproportionation, where, for example, a hydrogen atom is abstracted from one polymer chain, resulting in terminal unsaturation in the second polymer chain. In both instances, so-called dead polymer chains ($P_{n+m}$, $P_n$, $P_m$) are produced, however, an unsaturated chain end of a polymer may undergo further reaction as a macromonomer (**Scheme 1.1**).

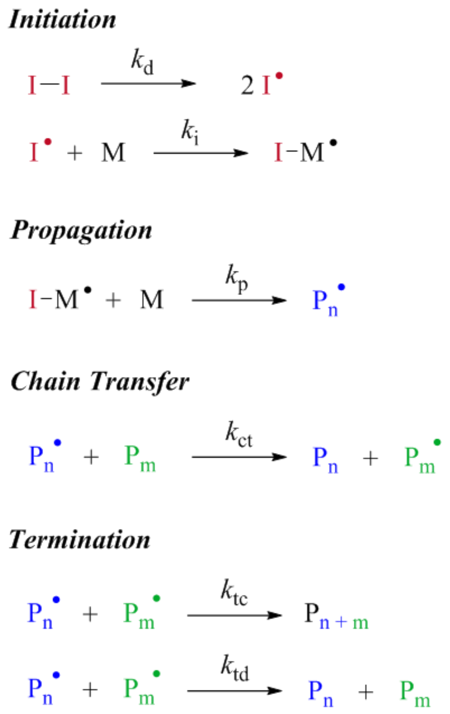

$$I{-}I \xrightarrow{k_d} 2\,I^{\bullet}$$
$$I^{\bullet} + M \xrightarrow{k_i} I{-}M^{\bullet}$$
$$I{-}M^{\bullet} + M \xrightarrow{k_p} P_n^{\bullet}$$
$$P_n^{\bullet} + P_m \xrightarrow{k_{ct}} P_n + P_m^{\bullet}$$
$$P_n^{\bullet} + P_m^{\bullet} \xrightarrow{k_{tc}} P_{n+m}$$
$$P_n^{\bullet} + P_m^{\bullet} \xrightarrow{k_{td}} P_n + P_m$$

**Scheme 1.1** Schematic of the key mechanistic steps in free radical polymerisation.

This conventional free radical polymerisation process has several considerations which must be taken into account. Firstly, due to the highly reactive nature of the radical species, the rate of termination is high. As a consequence, many chains terminate before complete conversion to a polymer strand, leading to a short lifetime of propagating radicals. Secondly, the propagation step is faster than initiation, which results in significant growth for some polymer chains whilst others are still initiating. Finally, control over the polymerisation process is hindered further by chain transfer events, where the radical species can transfer to the monomer, the solvent and other polymer chains. This may alter the site of the growing polymer, thereby resulting in irregular or branched architectures. These limitations lead to uncontrolled polymer chain growth, resulting in unpredictable molecular weights and broad molecular weight distributions, and a lack of control over the composition in the preparation of more complex structures, including block copolymers. Evidently, the degree of control over the polymerisation can therefore be vastly improved by minimising chain transfer and termination processes.[8]

### 1.2.2 Living polymerisation

A living polymerisation is a chain-growth polymerisation in which chain transfer and chain termination processes are absent, the former promoting the formation of linear polymers.[9] The polymerisation proceeds until all of the monomer has been consumed, and further addition of the monomer results in continued polymerisation. During a living polymerisation, the number average degree of polymerisation (DP) is a linear function of conversion, where the DP can be controlled by the ratio of monomer to initiator. A fast initiation step results in polymers with narrow molecular weight distributions, where the sequence can be controlled by the order in which different monomers are added to the growing polymer. This allows for the preparation of well-defined polymer chains with blocks of different monomers, so called block copolymers (**Figure 1.1**).

However, the absence of chain transfer and termination processes demands extremely stringent reaction conditions.[10] For instance, living ionic polymerisation of vinyl monomers requires complete exclusion of oxygen and water from the reaction system in order for the polymerisation to be successful.[11] This has limited the accessibility of such methods, leading to the development of alternative polymerisation techniques.

### 1.2.3 Reversible-deactivation radical polymerisation

Reversible-deactivation radical polymerisation (RDRP) establishes a mechanism whereby chain transfer and termination processes proceed at an undetectable level. As such, this is often denoted as a “quasi-living” or “pseudo-living” process. This is achieved through a dynamic equilibrium between propagating radicals and a dormant species, which results in a reduction in the concentration of radicals, thereby reducing the rate of termination and chain transfer, whilst significantly increasing the lifetime of propagating radicals. This dynamic equilibrium can be achieved either through systems exploiting a persistent radical effect or a degenerative transfer process.[12-15]

### *1.2.3.1 Persistent radical effect*

Persistent radicals cannot self-terminate, i.e. react with one another, and so they only participate in cross-coupling reactions with the polymeric propagating radicals. Termination reactions are, therefore, significantly reduced alongside a build-up of persistent radicals and a reduced concentration of propagating radicals.

Both atom-transfer radical polymerisation (ATRP) and nitroxide-mediated polymerisation (NMP) rely on a persistent radical effect to achieve controlled polymerisation. In ATRP, the persistent radical takes the form of a transition metal complex in a higher oxidation state, formed by a reversible redox reaction with an organic halide. This produces a radical species which can initiate a radical polymerisation with a vinyl monomer, allowing propagation until the growing polymer chain is deactivated again by the halide from the transition metal complex, re-gaining its lower oxidation state (**Scheme 1.2**). The dynamic equilibrium is such that a low concentration of radicals is maintained, with the majority of polymer chains remaining dormant. [16-18]

In NMP, historically the first developed RDRP technique, the persistent radical is a stable nitroxide which can be used to thermally activate and deactivate the growing polymer chains (**Scheme 1.3**). Similarly, the majority of polymer chains are dormant when capped by the mediating nitroxide, leading to a low concentration of radicals and minimisation of termination events.[14, 19]

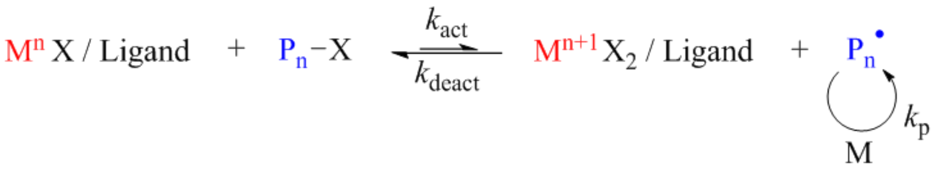

**Scheme 1.2** Schematic of the key activation/deactivation step by a transition metal complex in ATRP, where M represents a transition metal complex, X represents a halide and M represents a monomer species.

A further advantage of both ATRP and NMP lies in the retention of the radical mediating group, where the halide and nitroxide group, respectively, can be exploited in further polymerisation reactions to prepare block copolymers.

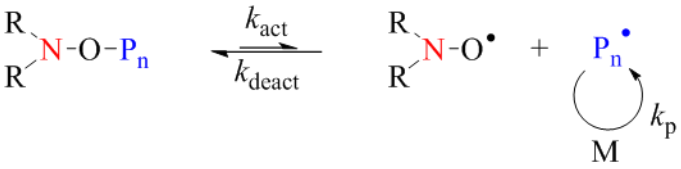

**Scheme 1.3** Schematic of the key activation/deactivation step by a nitroxide in NMP.

### 1.2.3.2 *Degenerative transfer*

Controlled radical polymerisation can also be achieved using a degenerative transfer mechanism, which differs from the persistent radical effect in that the active polymer radical is in equilibrium with a second dormant polymer chain, again with the aim of minimising radical-radical termination events. Notably, this mechanism is employed by the reversible addition-fragmentation chain transfer (RAFT) polymerisation process, the most recent of the radical methodologies.[20] In this process, the mechanism proceeds through the use of a thiocarbonyl chain transfer agent (CTA) containing a carefully selected R group and Z group (**Figure 1.2**).

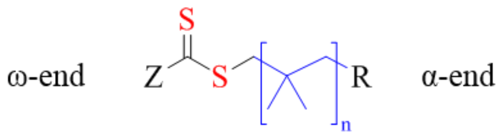

**Figure 1.2** Example of a RAFT polymer using a generic RAFT CTA, indicating the Z group at the ω-end and the R group at the α-end.

The thiocarbonyl CTA is used to form a radical intermediate from a reaction with an initiated polymer chain, which can subsequently fragment to produce a polymeric thiocarbonyl compound (macro-CTA) and a reinitiating group. Reinitiating groups can react with another monomer to generate a new polymer chain which can then undergo the same process, leading to eventual chain equilibrium when all of the CTA has reacted (**Scheme 1.4**).[20-22] This equilibrium process results in a majority of dormant chains, leaving few of the actively growing polymer chains and therefore a minimisation of termination events. Similar to ATRP and NMP, the mediating group is retained at the end of the polymer chain, in this case, the chain transfer agent. As such, RAFT polymerisation can also be used for the preparation of block copolymers.

Optimal choice of CTA is crucial to the success of a RAFT polymerisation, where a measured choice can yield polymers of predictable molecular weights and narrow dispersity whilst maintaining end group functionality. Both the R and Z groups of the CTA are important in determining the addition and fragmentations rates, which means that each must be tailored to the monomer used. The Z group needs to be stabilising enough to form the radical intermediate, but it must not be too stabilising such that the fragmentation will not occur. Its influence on the stability of the thiocarbonylthio intermediate depends strongly on its electron withdrawing or electron donating ability. In the equilibrium process, an electron withdrawing group will favour the formation of the intermediate, as this is more stabilised than the propagating radical.

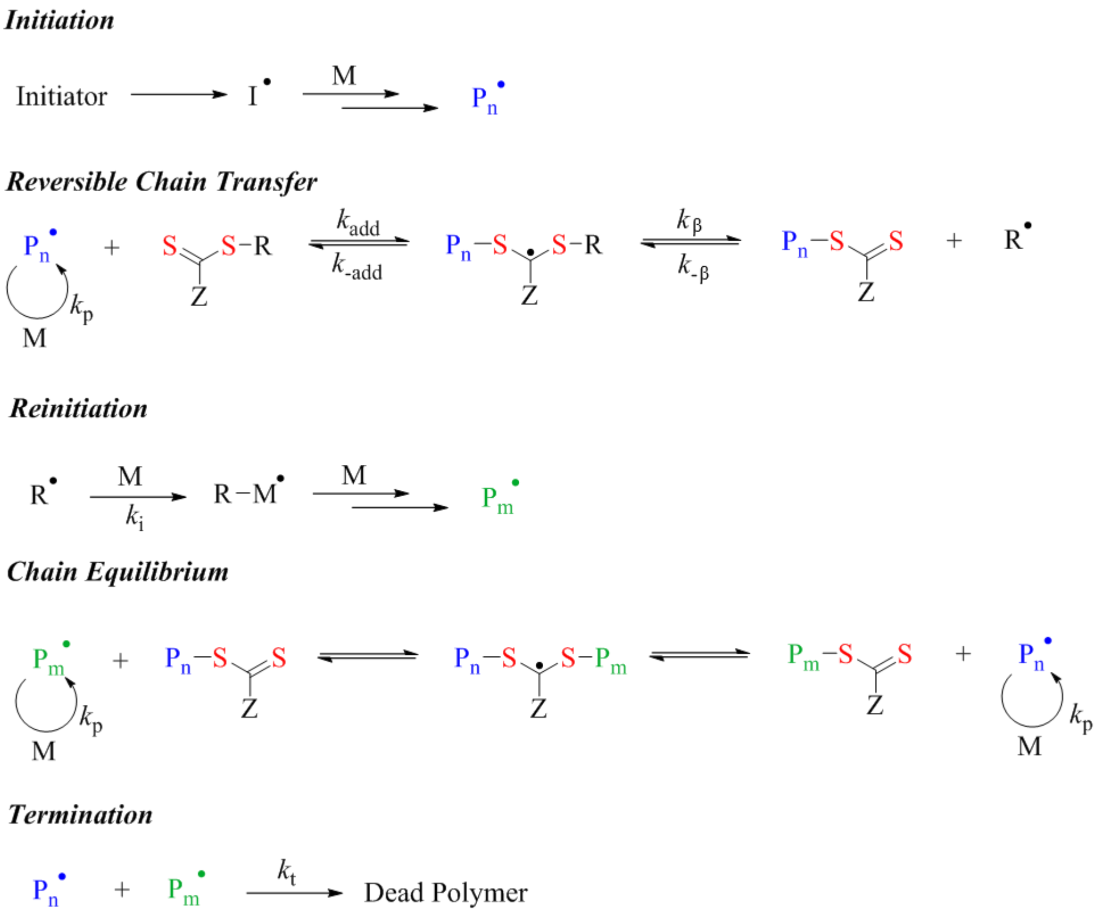
Initiation
Initiator
I•
M
Pn•
Reversible Chain Transfer
kadd
k-add
kβ
k-β
kp
M
S
S−R
Z
Pn−S
R•
Reinitiation
R•
M
ki
R−M•
Pm•
Chain Equilibrium
Pn−S
S−Pm
Pm−S
Termination
kt
Dead Polymer

**Scheme 1.4** Mechanism of RAFT polymerisation.

Equally, electron donating groups have the opposite effect, where the formation of the radical intermediate is not favoured. In varying the Z group, four main classes of CTA have been reported; dithioesters, dithiocarbamates, trithiocarbonates, and xanthates (**Figure 1.3**).

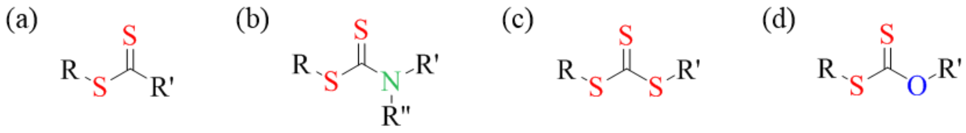
(a)
(b)
(c)
(d)
R
S
R'
N
R"
O

**Figure 1.3** Classes of chain transfer agent used in RAFT polymerisation; (a) dithioester, (b) dithiocarbamate, (c) trithiocarbonate and (d) xanthate.

In the design of chain transfer agents, general guidelines established by Moad and co-workers can be used to select the most appropriate Z group. In these guidelines, monomers can be classified into two groups; less activated monomers and more-activated monomers. Less activated monomers, for example, vinyl acetate (VAc), *N*-vinyl carbazole (NVC) and *N*-vinyl pyrrolidone (NVP), are poor homolytic leaving groups from the thiocarbonyl intermediate radical.[23] As such, a less active CTA, with a strongly electron donating Z group, is required to prevent inhibition of the polymerisation due to a build-up of the thiocarbonyl intermediate radical (**Figure 1.4**).

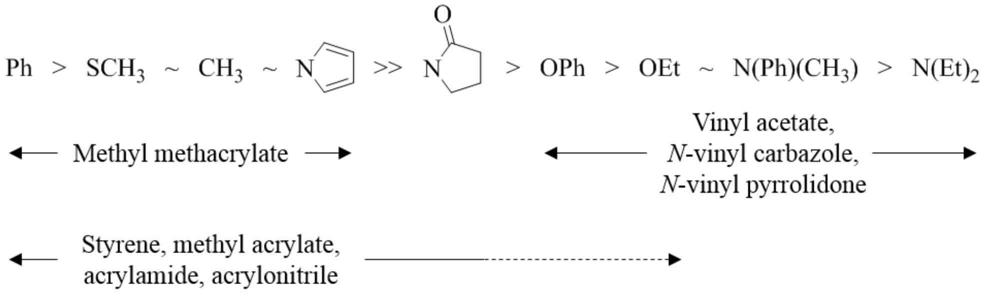
Ph > SCH3 ~ CH3 ~ N >> N > OPh > OEt ~ N(Ph)(CH3) > N(Et)2
O
Methyl methacrylate
Vinyl acetate, N-vinyl carbazole, N-vinyl pyrrolidone
Styrene, methyl acrylate, acrylamide, acrylonitrile

**Figure 1.4** General guidelines for RAFT agent Z group selection. Addition rates decrease from left to right (fragmentation rates increase). Dashed lines indicate partial control.[22]

More activated monomers, for example, methyl methacrylate (MMA), styrene (St), methyl acrylate (MA), acrylamide (AM) and acrylonitrile (AN), require a more active CTA with an electron withdrawing, or weakly electron donating, Z group. The resultant stabilised thiocarbonyl intermediate radical ensures sufficient propagation for this type of monomers. Similarly, the R group must act as an efficient homolytic leaving group from the intermediate radical, but it should also remain an effective initiating species for the monomer (**Figure 1.5**). Less activated monomers also benefit further from the use of an R group which is a good homolytic leaving group to promote efficient re-initiation.

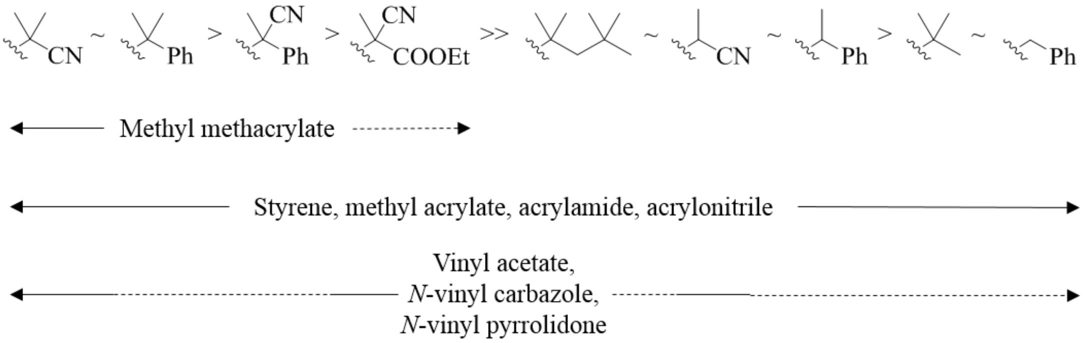
CN
Ph
CN
Ph
CN
COOEt
CN
Ph
Ph
~
>
>
>>
~
~
>
~
Methyl methacrylate
Styrene, methyl acrylate, acrylamide, acrylonitrile
Vinyl acetate,
N-vinyl carbazole,
N-vinyl pyrrolidone

**Figure 1.5** General guidelines for RAFT agent R group selection. Fragmentation rate decreases from left to right. Dashed lines indicate partial control.[22]

Arguably, RAFT polymerisation can be considered one of the most versatile and robust methods of polymerisation. Due to its high tolerance of functional groups, RAFT polymerisation has been successfully utilised with a wide range of functional monomers whilst maintaining good control.[24-27] However, end-functionalised polymers can easily be achieved not only by RAFT, using functional CTAs, but also by ATRP and NMP processes. Notably, RAFT can be carried out in a range of conditions, including aqueous media, and can be used to create a range of architectures including linear block copolymers,[28] star-shaped polymers,[29] hyperbranched polymers[30] and various higher order supramolecular structures.[31-33]

### *1.2.3.3 End group modification of RAFT polymers*

Commercially, one significant concern of RAFT polymers is that the presence of the labile C–S bond, that facilitates the polymerisation mechanism, results in an inherent reactivity of the polymer and the possibility of decomposition into malodourous sulfurcontaining materials. However, one novel feature of this technique is the ease with which the thiocarbonate at the ω-end of the polymer may be modified post-polymerisation.[34] Indeed, there is interest in not only introducing extra functional groups at the ω-end of the polymer chain, but also in conjugating biomolecules to, for example, introduce a stimulus in the form of a responsive RAFT polymer.[35]

One of the most common methods of end group modification is the use of a primary or secondary amine acting as a nucleophile to convert a thiocarbonylthio group into a thiol which can undergo a thiol-ene click reaction with a Michael acceptor (**Scheme 1.5**). Recently, the reduction of a trithiocarbonate and subsequent reaction with an acrylate has been developed as a one-pot procedure, where > 90% functionalisation was shown for a range of acrylates.[36] The exclusion of oxygen from this modification process is vital, as thiols can easily form disulfides, resulting in unwanted higher molecular weight species. As such, a reducing agent, such as tris(2-carboxyethyl)phosphine hydrochloride (TCEP.HCl), is often used to help prevent disulfide bridging.[37]

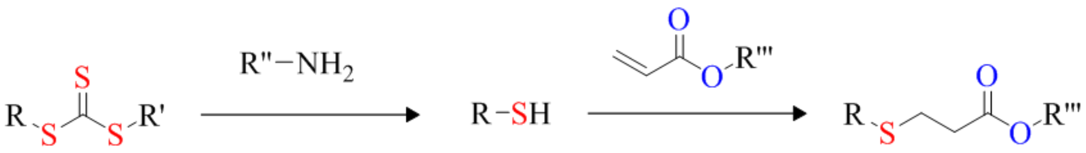

**Scheme 1.5** Schematic of a typical end group modification process of a trithiocarbonate with an acrylate.

One method for complete desulfurisation of a RAFT polymer is *via* radical-induced end group removal, where an initiating radical species can react with the thiocarbonyl group of a CTA to produce an intermediate radical. The polymeric radical can then react with a hydrogen donor, for example, a hypophosphite salt, to leave the polymer with a terminal hydrogen, or the initiating radical species if it is used in excess.[38]

### *1.2.4 Ring-opening polymerisation*

Ring-opening polymerisation (ROP) is a form of chain-growth polymerisation, where the active chain end reacts with a cyclic monomer by opening its ring system and reforms the active chain end at the terminal end of the opened monomer. ROP has been denoted as one of the most versatile methods for the production of biopolymers as well as playing an important role in the industrial synthesis of polymers on a large scale.

#### *1.2.4.1 Poly(L-lactide)*

Poly(lactide) (PLA) is an aliphatic polyester derived from renewable resources, such as corn starch, cassava roots and sugarcane, which can be synthesised using ROP.[39, 40] Due to its outstanding biodegradability, biocompatibility and low toxicity, it has become one of the most widely used bioplastics in the world.[41] As such, PLA has attracted significant interest in biomedical and pharmaceutical research as a potential candidate for tissue engineering and drug delivery treatments.[42]

The composition of PLA can take several forms depending on the tacticity of the cyclic monomer used. The four stereoisomers of lactide include; enantiopure L-lactide with two *S*-stereocentres, enantiopure D-lactide with two *R*-stereocentres, racemic D,L-lactide and *meso*-lactide with one *S*-stereocentre and one *R*-stereocentre. The two enantiopure isomers can form semi-crystalline polymers and can, therefore, be utilised in crystallisation-driven assembly processes.[43]

PLA can be prepared by two main methods; first developed was the polycondensation reaction from lactic acid.[44] However, this method does not provide high degrees of control, and high molecular weights can only be obtained with elevated temperatures, low pressures and long reaction times.[45]

In comparison, the ROP of lactide offers high conversions and narrow dispersities (*ca.* < 1.2).[46] Various catalysts have been studied for the ROP of lactide, including metal-based systems such as the widely used tin (II) octanoate catalyst.[47, 48] However, such catalysts have been shown to undergo undesirable transesterification processes, leading to broad molecular weight distributions. In 2005, Dove and co-workers reported the ROP of L-lactide using a metal-free thiourea/(-)-sparteine-based organocatalytic system (**Figure 1.6**) which gave very low dispersities (< 1.1) and minimal transesterification of the polymer backbone.[49, 50] In this process, the cyclic ester monomer and alcohol initiator are activated by hydrogen bonding interactions, which increases the electrophilicity of the lactide carbonyl and the nucleophilicity of the alcohol initiator. Furthermore, it was found that the thiourea molecule has increased recognition for the ester of the cyclic lactide monomer over the ester of the linear polymer, thus reducing the probability of attack of the propagating alcohol on the already formed PLA chain and rendering a lower dispersity.

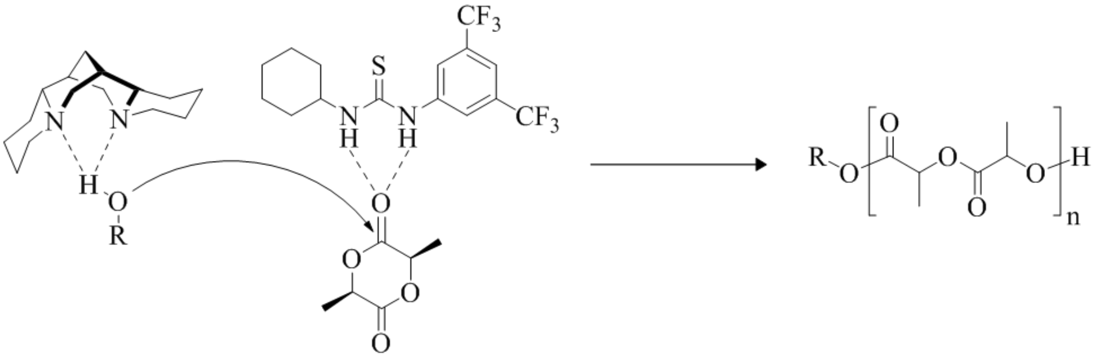

**Figure 1.6** Ring-opening polymerisation of L-lactide using a thiourea/(-)-sparteine organocatalytic system.

### *1.2.4.2 Poly(ε-caprolactone)*

Poly(ε-caprolactone) (PCL) is another example of a biodegradable polyester which has attracted significant interest in a range of fields including tissue engineering[51-53] and drug delivery.[54, 55] The ROP of ε-caprolactone can proceed using a range of different catalysts, including metal-based, organic or enzymatic systems.[56] Of particular interest is an organocatalytic approach, as described by Kakuchi and co-workers,[57] using diphenyl phosphate (DPP) due to its commercial availability, low toxicity and chemical stability.[58] An activated monomer mechanism was assumed, where DPP induces electrophilicity of the ε-caprolactone carbonyl to promote attack by an alcohol initiator (**Figure 1.7**). The reaction proceeded at room temperature, showing negligible transesterification of the polymer and very low dispersities (< 1.1).[57]

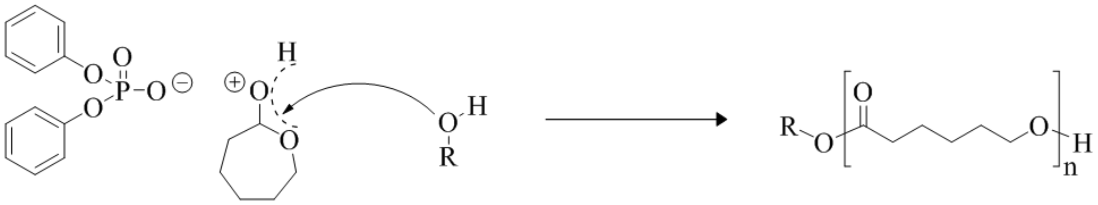

**Figure 1.7** Ring-opening polymerisation of ε-caprolactone using DPP as a catalyst.

## *1.3 Solution self-assembly of amphiphilic block copolymers*

Amphiphilic block copolymers, composed of a solvophilic block and a solvophobic block, can spontaneously self-assemble in selective solvents, where the solvent is selective for one of the blocks in the copolymer. For example, in a hydrophilic solvent, block copolymer chains can autonomously self-assemble to form a core-corona micellar structure, where the core is composed of the hydrophobic block, and the corona is composed of the hydrophilic block. Such an assembly is driven by the solvophobic effect in order to minimise energetically unfavourable interactions between the solvophobic core-forming block and the solvophilic solvent as well as entropically unfavourable ordering of the solvent.[59, 60]

### *1.3.1 Particle morphology*

The morphology of the micellar structure depends on several factors: the interfacial tension between the core-forming block and the solvent; the stretching of the core-forming block; and the repulsive interactions of the corona-forming block. Any modifications to polymer composition and self-assembly conditions, including temperature, solvent and salt concentration, can affect these factors and thus the resultant morphology of the self-assembled structure.

Manipulating the ratio of the core and corona blocks has led to the formation of a range of structures including spherical,[61] vesicular[62] and cylindrical[63] morphologies. A dimensionless packing parameter, $p$, can be used to predict the most likely morphology of block copolymers using the influence of molecular curvature. As a general guide, spherical micelles are formed when $p \leq ⅓$, cylindrical micelles are formed when $⅓ < p \leq ½$, and vesicles or bilayers are formed when $½ < p \leq 1$ (**Figure 1.8**).[59] As such, spherical micelles, occupying the smallest packing parameter range, as stated above, represent the most commonly used assembly morphology and, therefore, the most widely studied.

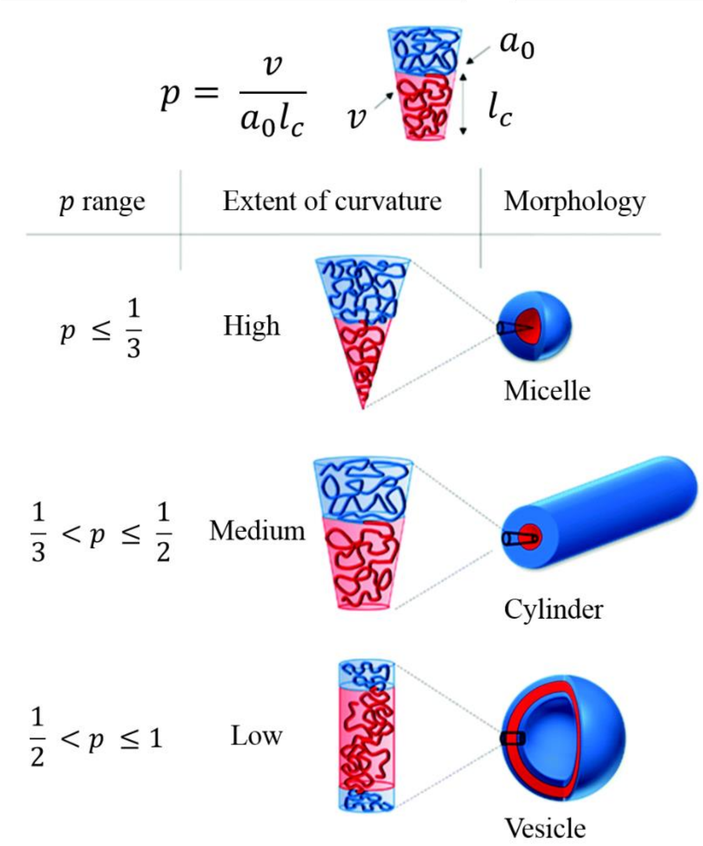
$p = \frac{v}{a_0 l_c}$
$a_0$
$v$
$l_c$
$p$ range
Extent of curvature
Morphology
$p \leq \frac{1}{3}$
High
Micelle
$\frac{1}{3} < p \leq \frac{1}{2}$
Medium
Cylinder
$\frac{1}{2} < p \leq 1$
Low
Vesicle

**Figure 1.8** Different morphologies obtained by targeting different packing parameters in a hydrophilic solvent, where $v$ is the volume of the hydrophobic block, $l_c$ is the length of the hydrophobic block and $a_0$ is the optimal area of the interface. Structures in red represent hydrophobic blocks and structures in blue represent hydrophilic blocks. [64]

Vesicular morphologies, occupying the largest packing parameter range exhibit a bilayer structure, where the hydrophobic block resides between hydrophilic chains to produce a hydrophilic core and a hydrophilic corona in a hydrophilic solvent. In terms of application, this type of structure allows for the encapsulation of water-soluble guest molecules in hydrophilic media.[59]

Access to cylindrical morphologies through altering block composition is clearly more difficult due to the narrow window theorised by packing parameter calculations. The self-assemblies often result in mixed morphologies with spherical or vesicular contaminants, rendering this pure cylindrical phase much more difficult to access. This represents a significant challenge, particularly due to the fact that cylindrical morphologies exhibit great potential in many biomedical applications. Attributed to their anisotropic nature, cylindrical nanoparticles have been shown to not only exhibit better cell uptake rates in comparison to their spherical counterparts, but undergo much longer *in vivo* circulation times on increasing cylinder length.[64-71]

### *1.3.2 Particle self-assembly methods*

Polymer assemblies following packing parameter rules can generally be obtained by direct dissolution or solvent-switch methodologies. Direct dissolution describes a simple approach of adding a selective solvent for the corona block directly to the polymer, causing assembly of a micellar structure. However, in a solvent-switch process, the selective solvent is slowly added to a solution of the polymer dissolved in a good solvent for both blocks. The resultant micelle assembly is then retained after removal of the good solvent. Although the assembly of cylindrical particles has been achieved through these methods, they can often result in the formation of multiple morphologies.[60]

However, a number of alternative approaches have been successfully utilised to target pure cylindrical phases. Polymerisation-induced self-assembly (PISA) presents one approach where, for example, a water-soluble monomer such as 2-hydroxypropyl methacrylate (HPMA) can be polymerised, using a water-soluble macro-CTA, to form a water-insoluble block and thus assemble during the polymerisation process. Several morphologies, including spheres, cylinders, vesicles and multi-lamellar vesicles have been reported during this process.[72-75] For example, Armes and co-workers showed the formation of pure phase spheres, worms and vesicles using poly(glycerol monomethacrylate) (PGMA)-*b*-PHPMA diblock copolymers using different block copolymer compositions and solid contents (**Figure 1.9**).[72] However, despite the formation of pure cylindrical phases, PISA tends to show a lack of control over the dimensions of the cylinders formed, limiting access to nanoparticles of controlled aspect ratio. Given the biological importance of elongated particles, the ability to target such high aspect ratio particles is key.

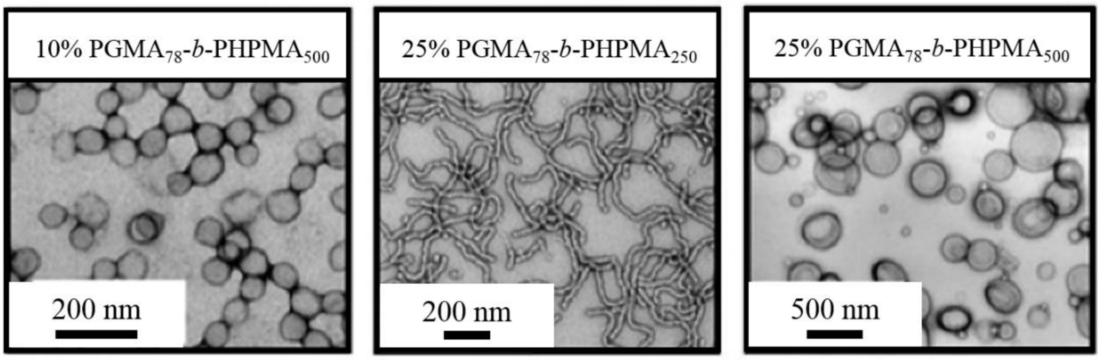
10% $PGMA_{78}$-*b*-$PHPMA_{500}$
200 nm
25% $PGMA_{78}$-*b*-$PHPMA_{250}$
200 nm
25% $PGMA_{78}$-*b*-$PHPMA_{500}$
500 nm

**Figure 1.9** TEM micrographs of PGMA-*b*-PHPMA pure phase spheres, worms and vesicles prepared using PISA, where the phases are obtained using different block ratios or solids contents as stated.[72]

Arguably, the most successful method in accessing cylindrical morphologies of controlled length to date is the exploitation of polymer crystallisation. Such a process requires the use of semi-crystalline polymers for one or more of the blocks.

## 1.4 Crystallisation-driven self-assembly

### 1.4.1 Polymer crystallisation

When polymers crystallise, they often form two-dimensional lamella which are much thinner than the length of the extended polymer chain. Keller first accounted for this by proposing a model for the formation of polymer single crystals, where long polymer chains exhibit a regular folding pattern oriented perpendicular to the lamella plane.[76] The model describes how the inherent long chain structure of polymers, even those which are monodisperse, can never fully crystallise due to the connectivity of the chain at the edges of the folds, rendering a semi-crystalline nature (**Figure 1.10**).

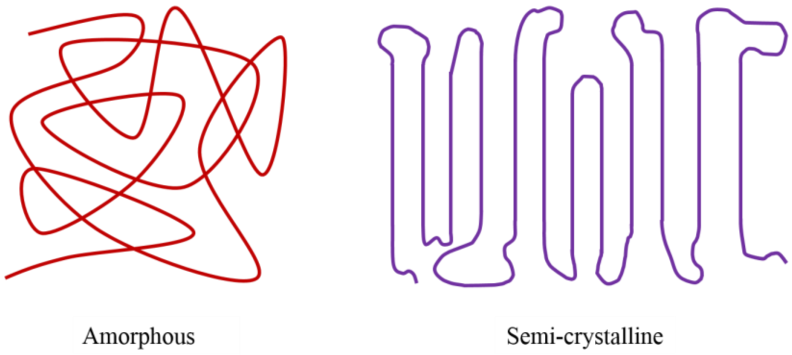

**Figure 1.10** Comparison of a random amorphous polymer chain with a regularly folded semi-crystalline polymer chain.

It is important to first note the effects of dispersity of the polymer chain, which hinders the study of crystallisation. The excess length of a polymer chain after completing chain folds may be left uncrystallised.[77] Therefore, ideally, polymers of very low dispersity should be used to study crystallisation.[78]

### *1.4.2 Chain-folding of crystalline-core micelles*

Vilgis and Halperin used a chain-folding model to propose the assembly of diblock copolymers into crystalline-core micelles.[79] In this model, the insoluble crystalline block undergoes chain-folding with a sharp interface excluding the other block from the crystal, forming the soluble amorphous upper and lower layers (**Figure 1.11**). The number of chain folds is associated with the distribution of the corona polymer chains on the crystal surface, as described by the tethering density (number of chains per unit area of surface). [80, 81]

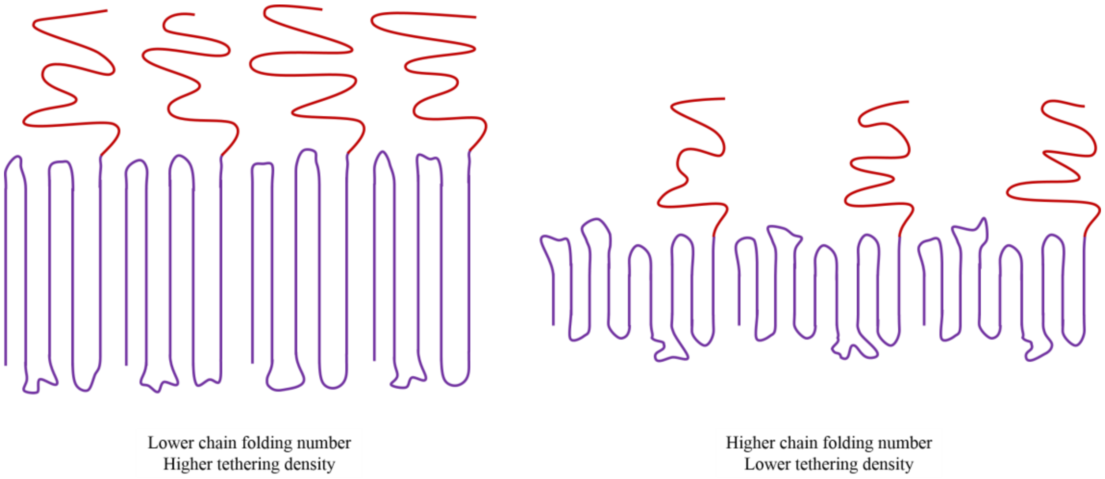

**Figure 1.11** High and low tethering density of diblock copolymers with a semi-crystalline core block given by low and high chain folding numbers, respectively. Corona chains are only shown on one side for clarity.

### *1.4.3 Mechanisms for solution crystallisation of diblock copolymers*

The process through which diblock copolymers with a crystallisable core block can undergo crystallisation to form nanostructures, termed crystallisation-driven self-assembly (CDSA), can proceed through a number of key mechanisms; self-nucleation or thermal crystallisation, living crystallisation, self-seeding and processes involving morphological transitions.[82, 83]

### 1.4.3.1 *Self-nucleation/thermal crystallisation*

Generally, in a self-nucleation process, the polymer is dissolved in a selective solvent at relatively high temperatures, often above the melting temperature of the crystalline core block. The solution is then cooled down to different crystallisation temperatures, where lowering the temperature reduces the solvent quality for the crystallisable core-forming block. This self-assembly method is reversible, i.e. heating above the melting temperature again destroys the crystal structure and reverts the polymer to an amorphous state (**Scheme 1.6**).

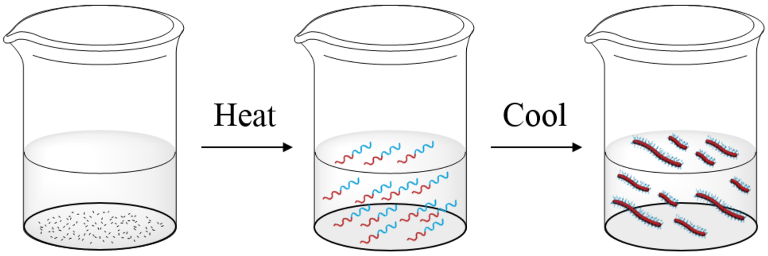

**Scheme 1.6** A typical self-nucleation process, where a polymer is heated to form molecularly dissolved unimers and cooled to form assembled structures.

Previously, the O'Reilly group have studied the assembly of poly(L-lactide) (PLLA)-containing block copolymers by heating above the glass transition temperature of PLLA, to soften the polymer, to yield well-defined cylindrical micelles of controlled dimensions using various corona blocks.[43, 84] The length and width of the cylinders could be tuned by altering block composition, where the least hydrophilic corona led to the longest cylinders.[85] Various other biorelevant crystalline blocks have also been studied and used to show that block copolymer composition,[86-88] temperature[89-91] and solvent quality[92] can effect morphology.

### *1.4.3.2 Living crystallisation*

Living crystallisation describes the growth of crystalline micelles achieved *via* an epitaxial growth mechanism on addition of molecularly dissolved polymer unimers to pre-formed crystalline seeds. The ends of the crystalline seeds remain active to the addition of these unimers to produce well-defined lengths and morphologies of the structures formed (**Scheme 1.7**).

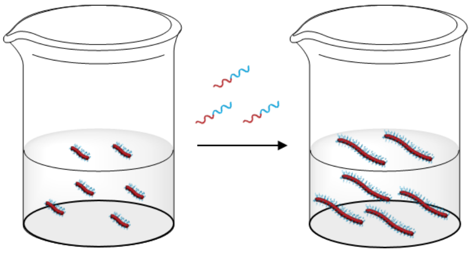

**Scheme 1.7** A typical epitaxial growth process, where molecularly dissolved unimers are added to pre-formed crystalline seeds to grow the assembled structures.

Although few reports of biodegradable polymers have been reported,[93] this technique has been studied extensively by Winnik, Manners and co-workers with poly(ferrocenyldimethylsilane) (PFS) block copolymers for the preparation of a wide range of nanostructures including cylinder[94-97] and platelet morphologies.[98-101] For example, PFS-*b*-poly(dimethylsiloxane) (PDMS) diblock copolymers have been shown to undergo CDSA to form cylindrical nanoparticles in *n*-hexane, a selective solvent for PFS.[102, 103] Cylinders of controlled length were achieved by addition of a controlled amount of unimer, which added to both ends of the structure *via* epitaxial growth. As such, the length of the cylinder formed could be targeted by consideration of the pre-formed cylinder seed-to-unimer ratio.

By addition of alternative unimers containing a PFS core-forming block, it was also shown that further functionality could be added to the coronal block to form cylindrical multi-block micelles (**Figure 1.12a**).[96, 104] Indeed, more complex morphologies have also been demonstrated using this concept, including branched micelles,[105] multi-armed micelles and scarf-shaped architectures consisting of plate-like structures with attached cylindrical tassels of controlled length (**Figure 1.12b**).[106, 107]

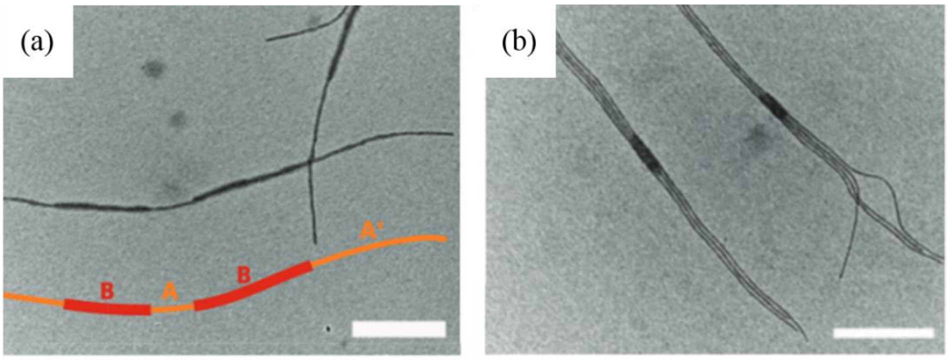

**Figure 1.12** TEM micrographs of crystalline PFS (a) cylindrical multi-blocks and (b) scarf-like structures. Scale bar = 500 nm.

#### *1.4.3.3 Self-seeding*

A self-seeding process circumvents nucleation, a process which is often problematic for polymers due to slow kinetics. This technique originates from the fundamental properties of polymer crystals in that they consist of regions of different chain folds. On heating, the different folded sections melt at different temperatures, simultaneously giving regions that are molten and regions that are crystalline. Melting such samples results in the initial melting of the least ordered parts, followed by melting of the most ordered parts on increasing temperature, independent of the heating time.

In self-seeding experiments, crystals regrow from a melt state, where melting takes place until only a few remnants of pre-existing crystals remain. These then act as seeds on subsequent cooling for further crystallisation. These particular seeds are all derived from a previously formed single crystal and thus will produce replicas of the same crystalline structure (**Scheme 1.8**).[108]

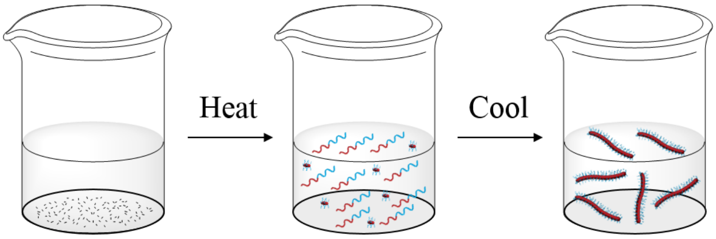

**Scheme 1.8** A typical self-seeding process, where a polymer is heated until few crystalline regions remain and cooled to form assembled structures.

This self-seeding technique has also been used successfully with diblock copolymers containing a PFS core-forming block,[109] as well as other polymers including poly(3-hexylthiophene)[110] and poly(ethylene oxide).[108] A solvent-induced self-seeding approach has also been demonstrated by Manners and co-workers, who showed that a good solvent can be exploited to perform self-seeding as opposed to temperature. For example, the addition of a small amount of THF to a solution of PFS-containing diblock copolymer seed micelles caused largely unimer formation, where only a few crystalline seeds remained. Upon evaporation of the THF, cylindrical micelles of controlled length were formed.[109]

### 1.4.3.4 *Morphological transitions*

Though crystallisation of the core drives the micellar structure, factors affecting the solubility of the corona block, such as a change in solvent or temperature, can cause reorganisation, leading to morphological transitions (**Scheme 1.9**).

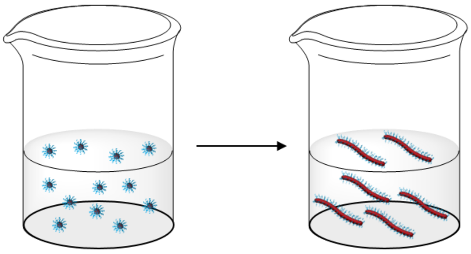

**Scheme 1.9** An example of a morphological transition, where a change in conditions allows a change from spherical to cylindrical assembled structures.

Previously, the O'Reilly group showed a sphere-to-cylinder transition using PLLA-*b*-PAA block copolymers. Spherical micelles were shown to slowly crystallise into seeds that further nucleated cylinder growth, however a large dispersity in cylinder length was observed.[111]

He and co-workers showed that sphere-to-cylinder and sphere-to-lamellae transformations of PCL-*b*-PEO block copolymer micelles could be induced by the addition of an inorganic salt to a solution of preformed crystalline spherical micelles.[112, 113] It was also shown that the conformation of the PEO block could be altered by pH in aqueous solution, where the soluble PEO corona could form hydrogen bonds with water molecules.[114] At high pH, the hydrogen bonds were partially destroyed, leading to reduced PEO chain solubility and aggregation of the corona. Thus, the tethering density was reduced and the PCL core was more exposed, leading to a transition from spherical micelles to higher order structures with less interfacial curvature.

## *1.4.4 Observable features of polymer crystals*

### *1.4.4.1 Polymer crystal habit*

Polymer single crystals possess very different external shapes, also known as the polymer crystal habit.[115] The habit of a single crystal is generally a good indicator of the symmetry of the underlying crystal structure. In general, tetragonal unit cells give rise to square crystals, hexagonal unit cells give rise to hexagonal crystals, and orthorhombic unit cells give rise to lozenge-shaped crystals. Unusually shaped crystals can be achieved for more complex structures, for example, triangular crystals have been reported for racemic stereocomplexes of poly(L-lactide) (PLLA) and poly(D-lactide) (PDLA) which crystallises in a trigonal unit cell structure.[116-118]

The formation of anisotropic crystals implies that the growth rate along one direction is faster than the others. Therefore, the nucleation barrier for crystallisation is different on different crystallographic planes. As such, a change in crystallisation conditions, such as solvent or temperature, to overcome the nucleation barrier may lead to different crystal habits.

### *1.4.4.2 Multilayer crystals*

In some instances, remaining segments on the top and bottom of the crystal can act as nuclei for the growth of a second lamella layer from polymers diffusing on top of the first layer. As such, a single polymer chain can easily co-crystallise into two separate neighbouring crystals when its chain length is long enough, with the secondary lamella exhibiting the same orientation as the first layer.[115] These so-called molecular ties are thus considered to connect lamellae to form multilayer crystals (**Figure 1.13**).[119] In dilute solution, polymer chains are generally less entangled, and, therefore, the probability that the chain could be incorporated in more than one crystal is much lower when compared to concentrated solutions.

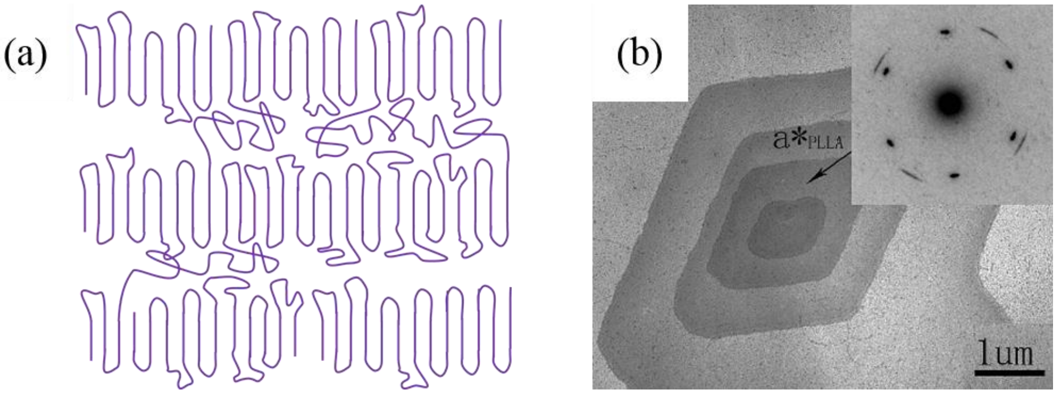

**Figure 1.13** (a) Amorphous molecular ties connecting lamellae to form multilayer crystals. (b) TEM micrograph of a PLLA crystal prepared by Chen and co-workers showing multi-layers.[120]

### *1.4.4.3 Edge and screw dislocations*

Defects in the growth of polymer single crystals can give rise to the spreading of crystallinity to form multiple crystal layers, where crystal growth in one layer can initiate growth in an adjacent layer. The most common reported defects include edge dislocation and screw dislocation mechanisms. An edge dislocation can occur at the boundary or adjacent to a hole in the crystal, allowing alignment in adjacent layers. A screw dislocation leads to staggered crystal growth which can be observed as many layered spiral overgrowths, where all of the layers are one single crystal connected by the defect (**Figure 1.14**).[121]

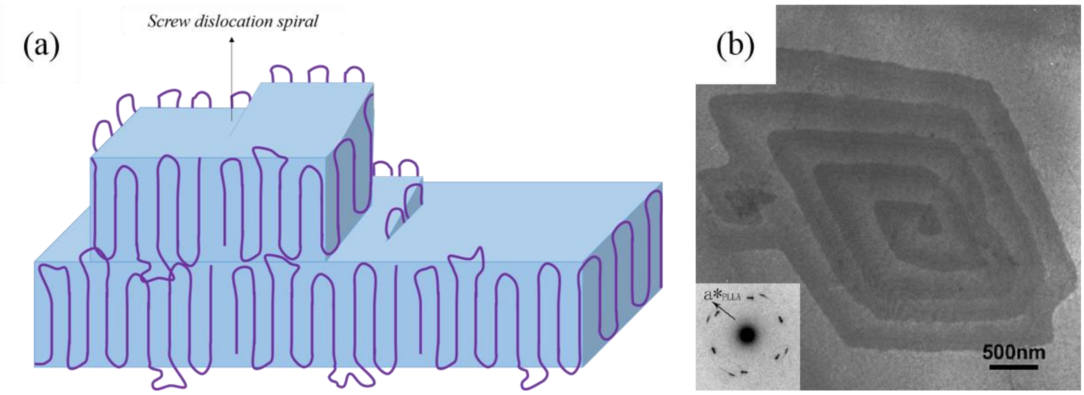
(a)
Screw dislocation spiral
(b)
a*PLLA
500nm

**Figure 1.14** (a) Multi-layer crystal showing a screw dislocation defect, where the crystal continues to spiral upward. (b) TEM micrograph of a PLLA crystal prepared by Chen and co-workers showing the screw dislocation defect.[120]

## *1.5 Analysis of nanoparticles*

Self-assembly of nanostructures can form a wide array of morphologies and dimensions, which can range from simple spherical micelles to extremely complex structures with multiple levels of hierarchical structure. Thus, it is important to accurately characterise the structures formed using multiple techniques to confirm size and morphology, as well as to recognise the limitations of such techniques when unconventional morphologies are studied.

Although standard polymer analysis techniques, for example, nuclear magnetic resonance (NMR) spectroscopy and size exclusion chromatography (SEC), are used to analyse the prepared polymers, much of the work discussed herein focusses on analysing the morphology of the particles prepared from the same polymer. As such, techniques used to analyse particle assemblies are key to this work.

The most common methods of particle analysis are scattering techniques and microscopy. Typically, the solution analysis of a scattering experiment fundamentally has greater statistical relevance when measuring particle properties. However, considering the array of unconventional morphologies studied herein, a focus has been placed particularly on microscopy methods due to the ability to directly visualise the particles formed and thus allow for ease of analysis. As such, care should be taken in microscopy to ensure that a representative population of particles are analysed.

A further concept considered throughout this work is the measure of a particle's surface charge in solution. As such, the relevance of zeta potential measurements is also discussed.

### 1.5.1 Transmission electron microscopy

Transmission electron microscopy (TEM) can be used to image individual particles at the nanoscale level. As conventional light microscopes are limited by the wavelength of light, a TEM microscope uses the much lower wavelength of electrons to access high resolution images. In TEM, a beam of electrons is focussed using electromagnetic lenses and transmitted through a specimen under vacuum to form an image.

The need for a vacuum environment can be problematic when imaging any particles suspended in liquid. As such, the most common methods of imaging require particles to be dried to a substrate or imaged at cryogenic temperatures (cryo-TEM).

Dry state TEM involves depositing a particle solution onto a thin substrate, followed by removal of the solvent. It is important to note that all particles are likely to be affected during this drying process, which can cause changes in stability, size and morphology.[122] In particular, the solvated corona of block copolymers nanostructures collapses in the dry state, often leading to substantially smaller particles sizes in comparison to those observed by analysis using solution methodologies. Furthermore, drying of suspended structures exposes particles to the surface tension of the solvent, and so the retracting liquid may sweep the particles into clusters which can misleadingly appear as aggregates or stacking patterns in a dry state TEM image.[123] These drawbacks can be avoided with the use of cryo-TEM, which involves rapid vitrification of the deposited particle solution on a thin substrate. Although extremely useful in imaging frozen particles in solution, there are a number of practical disadvantages of cryo-TEM, including cost and the extensive time needed to analyse samples. Furthermore, due to the frozen nature of the samples, a build-up of ice crystals can often prevent clear image collection.[123, 124]

Image contrast in TEM arises from the mass-thickness contrast, where thicker or more electron dense materials scatter more electrons and thus appear darker. Ideally, the particles must scatter to a much greater extent than the substrate to achieve an appropriate contrast for imaging. This is often difficult to achieve, where the typical size of a block copolymer nanostructure often approaches the *ca.* 40 nm thickness of a typical TEM substrate. Recently, thin graphene oxide substrates have been successfully used to image block copolymer nanostructures due to their nearly electron transparent nature.[125] However, a more cost-effective approach in enhancing contrast is the use of negative staining, where a heavy metal stain is applied to bind selectively to the substrate.[126] The heavy metal scatters more electrons than the particles, and thus appears much darker in comparison. Occasionally, the affinity of the stain for the particle in comparison to the substrate can result in positive staining, where the particles appear darker than the substrate (**Figure 1.15**).[126] Positive staining, or staining with low contrast, can also be observed on different regions of the same TEM substrate. In general, this can be attributed to the inherent poor stain coverage in some regions as a result of the stain drying process.

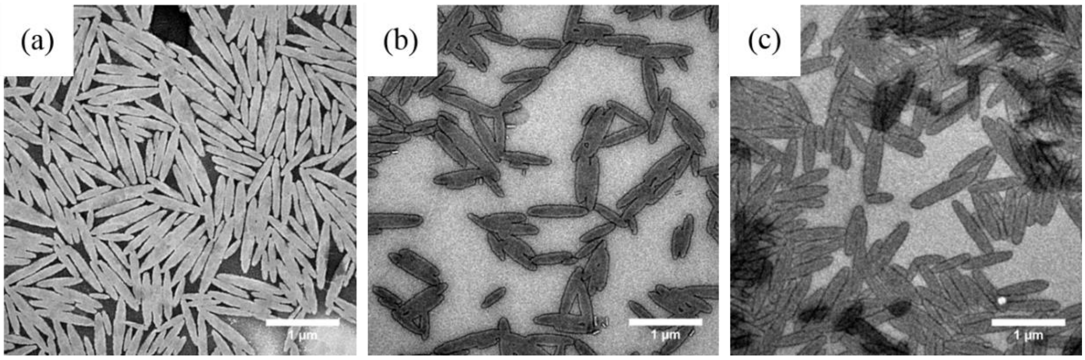

**Figure 1.15** TEM micrographs of poly(ε-caprolactone)-based nanostructures stained using uranyl actate (1 wt. % in 18.2 MΩ·cm water) showing (a) negative stain, (b) positive stain and (c) excess positive staining.

The most commonly used heavy metal stains include uranyl acetate, phosphotungstic acid, ruthenium tetroxide, osmium tetroxide and ammonium molybdate. For any given sample, it is often a good idea to screen several stains and preparation methods to obtain the best possible image. For example, an insufficient amount of stain will not produce an image with adequate contrast, whereas an excess of stain will result in a lack of penetration of the electron beam. Furthermore, the use of stains is well known to obscure information about the internal structure of particles as well as lead to the presence of misleading artefacts on a TEM substrate.[122, 123]

### 1.5.2 *Atomic force microscopy*

Atomic force microscopy (AFM) can be used to image the surface of sample. A cantilever with a very sharp tip is used to scan over a sample surface. As the tip approaches the surface, the attractive forces between the tip and the surface influences the deflection of the cantilever. An incident beam is reflected from the flat surface of the cantilever onto a position sensitive photodetector such that any deflection in the cantilever causes a change in the position of the reflected beam on the detector. The position of the beam is, therefore, proportional to the deflection of the cantilever and thus the topology of the sample.[127]

In contact mode, the tip is dragged across the surface. Generally, a feedback loop is used to control the height of the tip above the surface, thus maintaining a constant laser position to generate an accurate topographical map of the surface features. Generally, the lateral force exerted on the sample can be high, leading to sample damage or movement of loose objects. Imaging is also heavily influenced by frictional and adhesive forces,[128] for example, the adhesive meniscus force of a liquid droplet can influence deflection of the cantilever which can, in turn, distort images.[129]

In tapping mode, lateral forces are avoided by the cantilever oscillating on the surface such that the tip only touches the surface for short periods of time. The cantilever oscillates at its resonant frequency with a high amplitude when not in contact with the surface, where the amplitude of the oscillation is kept constant using a feedback loop. As the tip approaches the surface, a change in oscillation amplitude at each intermittent contact is used to generate a map of surface features. In general, tapping mode is expected to avoid adhesive forces as well as damage to the sample, and is, therefore, used solely throughout this work.[127]

While very high resolution in the vertical direction can be achieved, it should be noted that all AFM measurements are limited in the lateral direction by the size of the tip used due to convolution effects (**Figure 1.16**).[130] Similarly to TEM, dry state AFM also encounters difficulties in the particle drying process, which can lead to changes in size and morphology, as previously discussed.

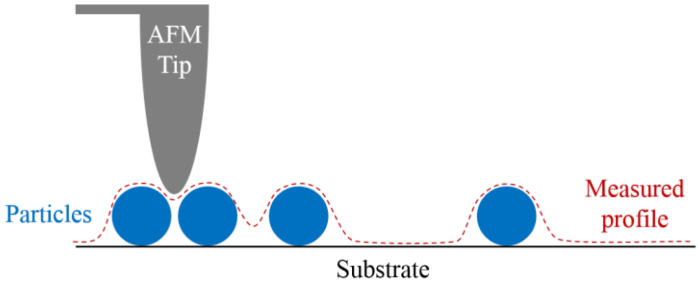

**Figure 1.16** Diagram of AFM convolution effects, where the size of the tip causes particles to appear larger in size, but has no noted effect on particle height in the measured profile.

### 1.5.3 Scattering techniques

Scattering techniques can be used to provide complementary information on particle analysis in a non-destructive manner. The most common techniques include dynamic light scattering (DLS),[131] static light scattering (SLS),[132] small-angle X-ray scattering (SAXS)[133] and small-angle neutron scattering (SANS).[134] Typically, a source of radiation is directed towards a sample, which interacts with the particles and causes a change in trajectory i.e. scattering, which is detected at a particular angle. The recorded data can provide information about the size and shape of the particles, as well as its molecular weight. Although statistically significant data is achieved, the presence of multiple populations or unconventional structures can be problematic in such averaged results.[135]

Both X-rays and neutrons have much smaller wavelengths, and so SAXS and SANS are ideal for smaller particles on the nanometre scale. DLS and SLS can be effectively used to monitor particles up to *ca.* 1 µm, however, the scale of a few microns, as is typical for particles used in this work, approaches the limit of these techniques.[136] As such, scattering is not the main analytical technique in this work, and is thus not discussed in further detail.

### 1.5.4 Zeta potential

Zeta potential, or $\zeta$-potential, can describe both the surface charge and the stability of a particle in suspension.[137] This parameter can be explained by the surface charge of a particle which can grant a high electrostatic potential at the surface, thus affecting the liquid medium surrounding the particle. Theoretically, this can be considered to occupy two layers which move with the particle in solution. For a cationic particle, the first inner layer, termed the Stern layer, is where oppositely charged anionic ions are strongly bound to the surface. The second layer forms an outer, more diffuse region, where anionic ions are attracted by the cationic particle, but repelled by the Stern layer and are therefore less strongly associated to the particle. The edge of this diffuse layer describes a theoretical boundary where the cationic charge of the particle is screened by the surrounding anionic counter ions in equilibrium with the ions in solution. The electrostatic potential at this boundary is considered the $\zeta$-potential.[137]

As a theoretical boundary, $\zeta$-potential cannot be measured directly. However, under an applied voltage, the electrophoretic mobility of a particle in solution can be calculated from its electrophoretic velocity and related to its $\zeta$-potential using theoretical models.[138] Electrophoretic mobility, $\mu_e$, is given by:

$$\mu_e = \frac{v_e}{E}$$

where $v_e$ is the electrophoretic velocity and $E$ is the electric field strength. Smoluchowski theory is the most commonly used method in reporting $\zeta$-potential as its validity extends to dispersed particles of any shape and concentration.[139] As such, $\zeta$-potential can be approximated by:

$$\zeta = \frac{\mu_e \eta}{\varepsilon_r \varepsilon_0}$$

where $\varepsilon_r$ is the dielectric constant of the solvent, $\varepsilon_0$ is the permittivity of free space and $\eta$ is the dynamic viscosity of the solvent. The model does not account for the Stern and diffuse layers, i.e. the distance over which the charge is shielded by ions in solution, and thus is only valid when the particle radius is much greater than this length.[140]

In aqueous media, the pH of the solution is one of the most important factors that affects its $\zeta$-potential.[138] For a cationic particle, the charge will be neutralised at high pH, and thus exhibit a near zero $\zeta$-potential, which may be interpreted as a low stability. Therefore, it is important to measure the $\zeta$-potential of cationic particles at a low pH to indicate not only charge but a measure of stability, where a $\zeta$-potential value of approximately + 30 mV or higher indicates a relatively stable particle. Similarly, a value of approximately – 30 mV or lower indicates a relatively stable anionic particle (**Figure 1.17**).

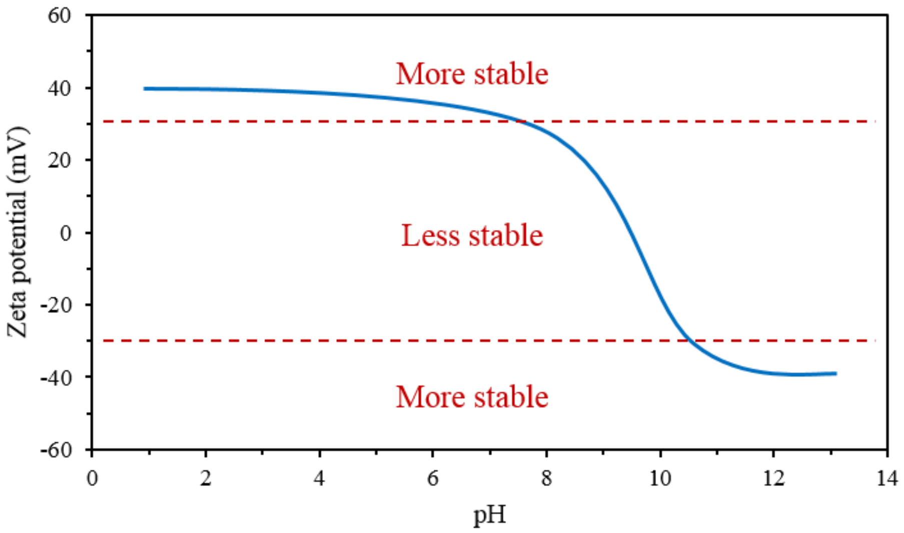

**Figure 1.17** Graph showing how zeta potential can vary with pH, indicating how the desired pH of more stable particles can be identified by the magnitude of zeta potential measurements.

## *1.6 Summary*

The theme of morphology is key to this work, and so several concepts used to achieve different morphologies of polymer nanoparticles have been introduced. Initially, various methods of polymerisation were presented, with a particular focus on RAFT polymerisation as the method utilised in this work. The use of different chain transfer agents and methods of end-group modification were also highlighted. Following this, the conventional method for the solution self-assembly of block copolymers was briefly discussed, emphasising that a difference in block ratio is essential in achieving different morphologies using the same block copolymer. To overcome this limitation, the concept of polymer crystallisation has been described as a method of preparing different morphologies. The general theory of polymer crystallisation has also been briefly introduced with an overview of the main methods of crystallisation-driven self-assembly of diblock copolymers with a crystallisable core block. Finally, a short analysis of the methods used to characterise particle morphology is given, demonstrating the key techniques used throughout this thesis.

## 1.7 References

1. G. Pasparakis, N. Krasnogor, L. Cronin, B. G. Davis and C. Alexander, *Chem. Soc. Rev.*, 2010, **39**, 286-300.
2. C. Chen, R. A. Wylie, D. Klinger and L. A. Connal, *Chem. Mater.*, 2017, **29**, 1918-1945.
3. J.-M. Williford, J. L. Santos, R. Shyam and H.-Q. Mao, *Biomater. Sci.*, 2015, **3**, 894-907.
4. N. Daum, C. Tscheka, A. Neumeyer and M. Schneider, *Wiley Interdiscp. Rev. Nanomed. Nanobiotechnol.*, 2012, **4**, 52-65.
5. J. Rodriguez-Hernandez, F. Chécot, Y. Gnanou and S. Lecommandoux, *Prog. Polym. Sci.*, 2005, **30**, 691-724.
6. K. Matyjaszewski, *Science*, 2011, **333**, 1104-1105.
7. G. Moad, E. Rizzardo and S. H. Thang, *Acc. Chem. Res.*, 2008, **41**, 1133-1142.
8. A. D. Jenkins, R. G. Jones and G. Moad, *Pure Appl. Chem.*, 2009, **82**, 483-491.
9. M. Szwarc, *Nature*, 1956, **178**, 1168-1169.
10. C. J. Hawker and K. L. Wooley, *Science*, 2005, **309**, 1200-1205.
11. P. C. Hiemenz and T. P. Lodge, *Polymer Chemistry*, CRC press, Second edn., 2007.
12. D. J. Keddie, *Chem. Soc. Rev.*, 2014, **43**, 496-505.
13. K. Matyjaszewski and J. Xia, *Chem. Rev.*, 2001, **101**, 2921-2990.
14. C. J. Hawker, A. W. Bosman and E. Harth, *Chem. Rev.*, 2001, **101**, 3661-3688.
15. W. A. Braunecker and K. Matyjaszewski, *Prog. Polym. Sci.*, 2007, **32**, 93-146.
16. J. Xia, S. G. Gaynor and K. Matyjaszewski, *Macromolecules*, 1998, **31**, 5958-5959.
17. J.-S. Wang and K. Matyjaszewski, *J. Am. Chem. Soc.*, 1995, **117**, 5614-5615.
18. M. Kato, M. Kamigaito, M. Sawamoto and T. Higashimura, *Macromolecules*, 1995, **28**, 1721-1723.
19. A. Tardy, V. Delplace, D. Siri, C. Lefay, S. Harrisson, B. d. F. A. Pereira, L. Charles, D. Gigmes, J. Nicolas and Y. Guillaneuf, *Polym. Chem.*, 2013, **4**, 4776-4787.
20. J. Chiefari, Y. Chong, F. Ercole, J. Krstina, J. Jeffery, T. P. Le, R. T. Mayadunne, G. F. Meijs, C. L. Moad and G. Moad, *Macromolecules*, 1998, **31**, 5559-5562.

21. G. Moad, E. Rizzardo and S. H. Thang, *Aust. J. Chem.*, 2005, **58**, 379-410.
22. G. Moad, E. Rizzardo and S. H. Thang, *Polymer*, 2008, **49**, 1079-1131.
23. A. Postma, T. P. Davis, G. Li, G. Moad and M. S. O'Shea, *Macromolecules*, 2006, **39**, 5307-5318.
24. S. Perrier and P. Takolpuckdee, *J. Polym. Sci. Part A: Polym. Chem.*, 2005, **43**, 5347-5393.
25. C. Barner-Kowollik and S. Perrier, *J. Polym. Sci. Part A: Polym. Chem.*, 2008, **46**, 5715-5723.
26. E. Rizzardo, M. Chen, B. Chong, G. Moad, M. Skidmore and S. H. Thang, *Macromol. Symp.*, 2007, **248**, 104-116.
27. G. Moad, E. Rizzardo and S. H. Thang, *Aust. J. Chem.*, 2012, **65**, 985-1076.
28. A. M. Bivigou-Koumba, J. Kristen, A. Laschewsky, P. Müller-Buschbaum and C. M. Papadakis, *Macromol. Chem. Phys.*, 2009, **210**, 565-578.
29. J. F. Quinn, R. P. Chaplin and T. P. Davis, *J. Polym. Sci. Part A: Polym. Chem.*, 2002, **40**, 2956-2966.
30. J. Xu, L. Tao, J. Liu, V. Bulmus and T. P. Davis, *Macromolecules*, 2009, **42**, 6893-6901.
31. J. Bernard, F. Lortie and B. Fenet, *Macromol. Rapid Comm.*, 2009, **30**, 83-88.
32. M. H. Stenzel, *Chem. Commun.*, 2008, 3486-3503.
33. M. H. Stenzel, *Macromol. Rapid Comm.*, 2009, **30**, 1603-1624.
34. H. Willcock and R. K. O'Reilly, *Polym. Chem.*, 2010, **1**, 149-157.
35. A. S. Hoffman and P. S. Stayton, 2004.
36. J. M. Spruell, B. A. Levy, A. Sutherland, W. R. Dichtel, J. Y. Cheng, J. F. Stoddart and A. Nelson, *J. Polym. Sci. Part A: Polym. Chem.*, 2009, **47**, 346-356.
37. C. W. Scales, A. J. Convertine and C. L. McCormick, *Biomacromolecules*, 2006, **7**, 1389-1392.
38. Y. K. Chong, G. Moad, E. Rizzardo and S. H. Thang, *Macromolecules*, 2007, **40**, 4446-4455.
39. B. J. O'Keefe, M. A. Hillmyer and W. B. Tolman, *J. Chem. Soc., Dalton Trans.*, 2001, 2215-2224.
40. K. S. Anderson, K. M. Schreck and M. A. Hillmyer, *Polym. Rev.*, 2008, **48**, 85-108.

41. K. E. Uhrich, S. M. Cannizzaro, R. S. Langer and K. M. Shakesheff, *Chem. Rev.*, 1999, **99**, 3181-3198.

42. J. M. Becker, R. J. Pounder and A. P. Dove, *Macromol. Rapid Commun.*, 2010, **31**, 1923-1937.

43. N. Petzetakis, A. P. Dove and R. K. O'Reilly, *Chem. Sci.*, 2011, **2**, 955-960.

44. D. Garlotta, *J. Polym. Environ.*, 2001, **9**, 63-84.

45. T. Maharana, B. Mohanty and Y. Negi, *Prog. Polym. Sci.*, 2009, **34**, 99-124.

46. O. Dechy-Cabaret, B. Martin-Vaca and D. Bourissou, *Chem. Rev.*, 2004, **104**, 6147-6176.

47. A. Kowalski, A. Duda and S. Penczek, *Macromolecules*, 2000, **33**, 689-695.

48. A. Gupta and V. Kumar, *Eur. Polym. J.*, 2007, **43**, 4053-4074.

49. A. P. Dove, R. C. Pratt, B. G. Lohmeijer, R. M. Waymouth and J. L. Hedrick, *J. Am. Chem. Soc.*, 2005, **127**, 13798-13799.

50. A. P. Dove, *ACS Macro Lett.*, 2012, **1**, 1409-1412.

51. M. Jenkins, K. Harrison, M. Silva, M. Whitaker, K. Shakesheff and S. Howdle, *Eur. Polym. J.*, 2006, **42**, 3145-3151.

52. J. Pena, T. Corrales, I. Izquierdo-Barba, A. L. Doadrio and M. Vallet-Regí, *Polym. Degrad. Stab.*, 2006, **91**, 1424-1432.

53. D. W. Hutmacher, T. Schantz, I. Zein, K. W. Ng, S. H. Teoh and K. C. Tan, *J. Biomed. Mater. Res.*, 2001, **55**, 203-216.

54. D. Chen, J. Bei and S. Wang, *Polym. Degrad. Stab.*, 2000, **67**, 455-459.

55. V. Sinha, K. Bansal, R. Kaushik, R. Kumria and A. Trehan, *Int. J. Pharm.*, 2004, **278**, 1-23.

56. M. Labet and W. Thielemans, *Chem. Soc. Rev.*, 2009, **38**, 3484-3504.

57. K. Makiguchi, T. Satoh and T. Kakuchi, *Macromolecules*, 2011, **44**, 1999-2005.

58. F. Krasovec and J. Jan, *J. Croat. Chem. Acta*, 1963, **35**, 183-193.

59. A. Blanazs, S. P. Armes and A. J. Ryan, *Macromol. Rapid Commun.*, 2009, **30**, 267-277.

60. Y. Mai and A. Eisenberg, *Chem. Soc. Rev.*, 2012, **41**, 5969-5985.

61. P. Bhargava, J. X. Zheng, P. Li, R. P. Quirk, F. W. Harris and S. Z. Cheng, *Macromolecules*, 2006, **39**, 4880-4888.

62. L. Zhang and A. Eisenberg, *Science*, 1995, **268**, 1728-1731.

63. C.-K. Chen, S.-C. Lin, R.-M. Ho, Y.-W. Chiang and B. Lotz, *Macromolecules*, 2010, **43**, 7752-7758.
64. K. E. Doncom, L. D. Blackman, D. B. Wright, M. I. Gibson and R. K. O'Reilly, *Chem. Soc. Rev.*, 2017, **46**, 4119-4134.
65. S. E. A. Gratton, P. A. Ropp, P. D. Pohlhaus, J. C. Luft, V. J. Madden, M. E. Napier and J. M. DeSimone, *Proc. Natl. Acad. Sci.*, 2008, **105**, 11613-11618.
66. X. Liu, F. Wu, Y. Tian, M. Wu, Q. Zhou, S. Jiang and Z. Niu, *Sci. Rep.*, 2016, **6**, 24567.
67. V. Raeesi, L. Y. T. Chou and W. C. W. Chan, *Adv. Mater.*, 2016, **28**, 8511-8518.
68. M. Caldorera-Moore, N. Guimard, L. Shi and K. Roy, *Expert Opin. Drug Deliv.*, 2010, **7**, 479-495.
69. Y. Geng, P. Dalhaimer, S. Cai, R. Tsai, M. Tewari, T. Minko and D. E. Discher, *Nat. Nanotechnol.*, 2007, **2**, 249-255.
70. R. Toy, P. M. Peiris, K. B. Ghaghada and E. Karathanasis, *Nanomedicine*, 2014, **9**, 121-134.
71. X. Huang, X. Teng, D. Chen, F. Tang and J. He, *Biomaterials*, 2010, **31**, 438-448.
72. N. J. Warren and S. P. Armes, *J. Am. Chem. Soc.*, 2014, **136**, 10174-10185.
73. M. J. Derry, L. A. Fielding and S. P. Armes, *Prog. Polym. Sci.*, 2016, **52**, 1-18.
74. N. J. Warren, O. O. Mykhaylyk, D. Mahmood, A. J. Ryan and S. P. Armes, *J. Am. Chem. Soc.*, 2014, **136**, 1023-1033.
75. L. A. Fielding, J. A. Lane, M. J. Derry, O. O. Mykhaylyk and S. P. Armes, *J. Am. Chem. Soc.*, 2014, **136**, 5790-5798.
76. A. Keller, *Philos. Mag.*, 1957, **2**, 1171-1175.
77. G. Ungar and X.-b. Zeng, *Chem. Rev.*, 2001, **101**, 4157-4188.
78. R. F. Sekerka, *J. Cryst. Growth*, 1993, **128**, 1-12.
79. T. Vilgis and A. Halperin, *Macromolecules*, 1991, **24**, 2090-2095.
80. J. X. Zheng, H. Xiong, W. Y. Chen, K. Lee, R. M. Van Horn, R. P. Quirk, B. Lotz, E. L. Thomas, A.-C. Shi and S. Z. D. Cheng, *Macromolecules*, 2006, **39**, 641-650.
81. E. K. Lin and A. P. Gast, *Macromolecules*, 1996, **29**, 4432-4441.
82. J. J. Crassous, P. Schurtenberger, M. Ballauff and A. M. Mihut, *Polymer*, 2015, **62**, A1-A13.

83. J. Schmelz, F. H. Schacher and H. Schmalz, *Soft Matter*, 2013, **9**, 2101-2107.

84. A. Pitto-Barry, N. Kirby, A. P. Dove and R. K. O'Reilly, *Polym. Chem.*, 2014, **5**, 1427-1436.

85. L. Sun, N. Petzetakis, A. Pitto-Barry, T. L. Schiller, N. Kirby, D. J. Keddie, B. J. Boyd, R. K. O'Reilly and A. P. Dove, *Macromolecules*, 2013, **46**, 9074-9082.

86. A. M. Mihut, J. J. Crassous, H. Schmalz, M. Drechsler and M. Ballauff, *Soft Matter*, 2012, **8**, 3163-3173.

87. L. Yin, T. P. Lodge and M. A. Hillmyer, *Macromolecules*, 2012, **45**, 9460-9467.

88. L. Yin and M. A. Hillmyer, *Macromolecules*, 2011, **44**, 3021-3028.

89. Z. X. Du, J. T. Xu and Z. Q. Fan, *Macromol. Rapid Commun.*, 2008, **29**, 467-471.

90. A. M. Mihut, A. Chiche, M. Drechsler, H. Schmalz, E. Di Cola, G. Krausch and M. Ballauff, *Soft Matter*, 2009, **5**, 208-213.

91. A. M. Mihut, J. J. Crassous, H. Schmalz and M. Ballauff, *Colloid Polym. Sci.*, 2010, **288**, 573-578.

92. M. Su, H. Huang, X. Ma, Q. Wang and Z. Su, *Macromol. Rapid Commun.*, 2013, **34**, 1067-1071.

93. W.-N. He, B. Zhou, J.-T. Xu, B.-Y. Du and Z.-Q. Fan, *Macromolecules*, 2012, **45**, 9768-9778.

94. S. K. Patra, R. Ahmed, G. R. Whittell, D. J. Lunn, E. L. Dunphy, M. A. Winnik and I. Manners, *J. Am. Chem. Soc.*, 2011, **133**, 8842-8845.

95. J. Schmelz, A. E. Schedl, C. Steinlein, I. Manners and H. Schmalz, *J. Am. Chem. Soc.*, 2012, **134**, 14217-14225.

96. X. Wang, G. Guerin, H. Wang, Y. Wang, I. Manners and M. A. Winnik, *Science*, 2007, **317**, 644-647.

97. A. Nazemi, C. E. Boott, D. J. Lunn, J. Gwyther, D. W. Hayward, R. M. Richardson, M. A. Winnik and I. Manners, *J. Am. Chem. Soc.*, 2016, **138**, 4484-4493.

98. S. F. Mohd Yusoff, M.-S. Hsiao, F. H. Schacher, M. A. Winnik and I. Manners, *Macromolecules*, 2012, **45**, 3883-3891.

99. A. Presa Soto, J. B. Gilroy, M. A. Winnik and I. Manners, *Angew. Chem. Int. Ed.*, 2010, **49**, 8220-8223.

100. G. Molev, Y. Lu, K. S. Kim, I. C. Majdalani, G. Guerin, S. Petrov, G. Walker, I. Manners and M. A. Winnik, *Macromolecules*, 2014, **47**, 2604-2615.
101. L. Cao, I. Manners and M. A. Winnik, *Macromolecules*, 2002, **35**, 8258-8260.
102. J. Raez, R. Barjovanu, J. A. Massey, M. A. Winnik and I. Manners, *Angew. Chem. Int. Ed.*, 2000, **39**, 3862-3865.
103. J. A. Massey, K. Temple, L. Cao, Y. Rharbi, J. Raez, M. A. Winnik and I. Manners, *J. Am. Chem. Soc.*, 2000, **122**, 11577-11584.
104. F. He, T. Gädt, I. Manners and M. A. Winnik, *J. Am. Chem. Soc.*, 2011, **133**, 9095-9103.
105. H. Qiu, V. A. Du, M. A. Winnik and I. Manners, *J. Am. Chem. Soc.*, 2013, **135**, 17739-17742.
106. T. Gädt, N. S. Ieong, G. Cambridge, M. A. Winnik and I. Manners, *Nat. Mater.*, 2009, **8**, 144-150.
107. H. Qiu, G. Cambridge, M. A. Winnik and I. Manners, *J. Am. Chem. Soc.*, 2013, **135**, 12180-12183.
108. J. Xu, Y. Ma, W. Hu, M. Rehahn and G. Reiter, *Nat. Mater.*, 2009, **8**, 348-353.
109. J. Qian, Y. Lu, A. Chia, M. Zhang, P. A. Rupar, N. Gunari, G. C. Walker, G. Cambridge, F. He and G. Guerin, *ACS Nano*, 2013, **7**, 3754-3766.
110. J. Qian, X. Li, D. J. Lunn, J. Gwyther, Z. M. Hudson, E. Kynaston, P. A. Rupar, M. A. Winnik and I. Manners, *J. Am. Chem. Soc*, 2014, **136**, 4121-4124.
111. N. Petzetakis, D. Walker, A. P. Dove and R. K. O'Reilly, *Soft Matter*, 2012, **8**, 7408-7414.
112. W. N. He, J. T. Xu, B. Y. Du, Z. Q. Fan and X. Wang, *Macromol. Chem. Phys.*, 2010, **211**, 1909-1916.
113. Z.-X. Du, J.-T. Xu and Z.-Q. Fan, *Macromolecules*, 2007, **40**, 7633-7637.
114. W. N. He, J. T. Xu, B. Y. Du, Z. Q. Fan and F. L. Sun, *Macromol. Chem. Phys.*, 2012, **213**, 952-964.
115. S. Z. Cheng and B. Lotz, *Phil. Trans. R. Soc. Lond. A*, 2003, **361**, 517-537.
116. D. Brizzolara, H.-J. Cantow, K. Diederichs, E. Keller and A. J. Domb, *Macromolecules*, 1996, **29**, 191-197.
117. T. Okihara, M. Tsuji, A. Kawaguchi, K.-I. Katayama, H. Tsuji, S.-H. Hyon and Y. Ikada, *J. Macromol. Sci. B Phys.*, 1991, **30**, 119-140.
118. L. Cartier, T. Okihara and B. Lotz, *Macromolecules*, 1997, **30**, 6313-6322.

119. D. Bassett, A. Keller and S. Mitsuhashi, *J. Polym. Sci. A Gen. Pap.*, 1963, **1**, 763-788.
120. J. Yang, T. Zhao, Y. Zhou, L. Liu, G. Li, E. Zhou and X. Chen, *Macromolecules*, 2007, **40**, 2791-2797.
121. S. Hong, W. J. MacKnight, T. P. Russell and S. P. Gido, *Macromolecules*, 2001, **34**, 2876-2883.
122. Y. Talmon, *J. Colloid Interface Sci.*, 1983, **93**, 366-382.
123. H. Friedrich, P. M. Frederik, G. de With and N. A. Sommerdijk, *Angew. Chem. Int. Ed.*, 2010, **49**, 7850-7858.
124. J. Dubochet, M. Adrian, J.-J. Chang, J.-C. Homo, J. Lepault, A. W. McDowall and P. Schultz, *Q. Rev. Biophys.*, 1988, **21**, 129-228.
125. J. P. Patterson, A. M. Sanchez, N. Petzetakis, T. P. Smart, T. H. Epps III, I. Portman, N. R. Wilson and R. K. O'Reilly, *Soft Matter*, 2012, **8**, 3322-3328.
126. M. R. Libera and R. F. Egerton, *Polym. Rev.*, 2010, **50**, 321-339.
127. P. Eaton and P. West, *Atomic force microscopy*, Oxford University Press, 2010.
128. H.-J. Butt, B. Cappella and M. Kappl, *Surf. Sci. Rep.*, 2005, **59**, 1-152.
129. V. J. Morris, A. R. Kirby and A. P. Gunning, *Atomic force microscopy for biologists*, World Scientific, 1999.
130. F. J. Giessibl, *Rev. Modern Phys.*, 2003, **75**, 949.
131. W. Brown, *Dynamic light scattering: the method and some applications*, Oxford University Press, USA, 1993.
132. W. Brown, *Light scattering: principles and development*, Oxford University Press, 1996.
133. R.-J. Roe, *Methods of X-ray and neutron scattering in polymer science*, Oxford University Press on Demand, 2000.
134. J. S. Higgins and H. Benoît, *Polymers and neutron scattering*, Clarendon Press Oxford, 1994.
135. W. Schärtl, *Light scattering from polymer solutions and nanoparticle dispersions*, Springer Science & Business Media, 2007.
136. J. P. Patterson, M. P. Robin, C. Chassenieux, O. Colombani and R. K. O'Reilly, *Chem. Soc. Rev.*, 2014, **43**, 2412-2425.
137. R. J. Hunter, *Zeta potential in colloid science: principles and applications*, Academic Press, 2013.
138. B. J. Kirby and E. F. Hasselbrink, *Electrophoresis*, 2004, **25**, 187-202.

139. A. Sze, D. Erickson, L. Ren and D. Li, *J. Colloid Interface Sci.*, 2003, **261**, 402-410.

140. Malvern, *Zetasizer Nano Series Tech. Note. MRK654*, 2011.

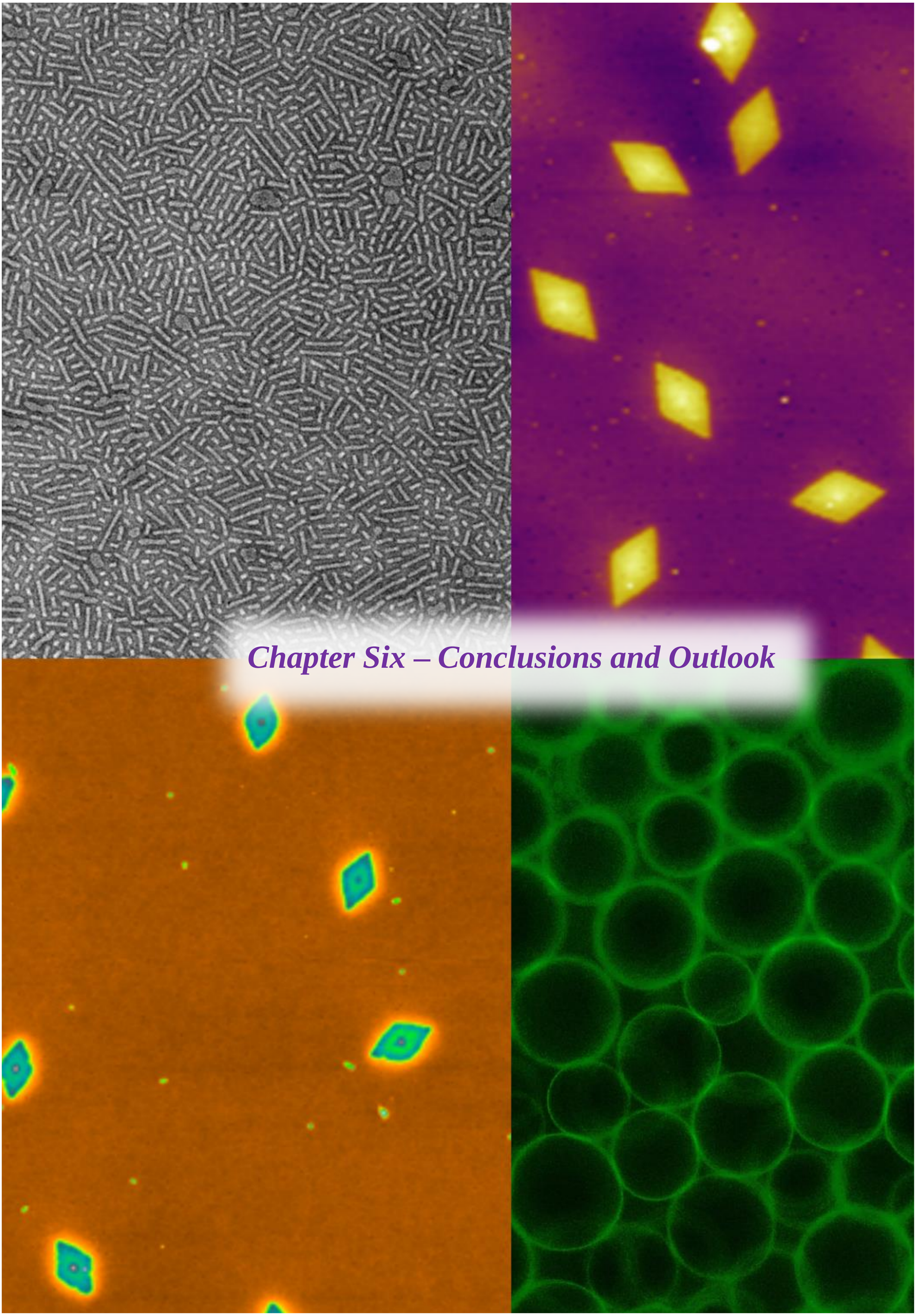

# Chapter Six – Conclusions and Outlook

## *6.1 Summary*

The main focus of this thesis has been the solution crystallisation of degradable amphiphilic diblock copolymers containing one crystallisable solvophobic block. In particular, interest has been placed on the range of morphologies and sizes that can be obtained with these polymers using a crystallisation-driven self-assembly (CDSA) methodology. Both the preparation of these crystalline nanostructures of controlled dimensions and their application within secondary materials has been investigated, showing the ease of use and versatility of the crystallisation process and the potential utility of such materials.

## *6.2 Principal conclusions*

### *6.2.1 Solubility-controlled crystallisation*

The theme of block copolymer solubility is prevalent throughout this work and is utilised repeatedly to control crystallisation processes. Largely, this is due to the discovery of the formation of diamond-shaped platelets from the single phase solution assembly of poly(L-lactide) (PLLA) diblock copolymers. This work has demonstrated not only the ease of preparing such materials, but the use of Log$P_{\text{oct}}$ analysis as a technique for solvent selection in the presented self-assemblies. With further study and optimisation, such a method has the potential to be developed as a universal *ab initio* screening process for a wide array of block copolymers, allowing ease of access to polymer nanostructures, due to the simplicity of the methods described, and a much greater efficiency in polymer solution self-assembly research.

Indeed, consideration of this aspect has led to the highly controlled size of PLLA-*b*-poly(*N*,*N*-dimethylaminoethyl methacrylate) platelets, which could be tuned by simple adjustments of the solvent used for self-assembly without any modifications to the chemistry of the copolymer or its block ratios. This process has, therefore, provided a platform to develop a range of materials, some of which have been considered in this work, including Pickering emulsifiers, gel adhesives and nanocomposites for hydrogel reinforcement. The potential for such versatile nanostructures extends beyond the scope of this thesis, where much interest has been placed on using elongated or platelet-like nanoparticles in nanomedical applications due to their altered interactions with cells.

The efficiency of this process has also been demonstrated with the self-assembly of poly(ε-caprolactone) (PCL) amphiphilic block copolymers for the formation of crystalline platelets and cylindrical nanostructures of highly controlled dimensions. In particular, consideration of solvent solubility in comparison to polymer solubility directed the preparation of a novel polymer to allow crystallisation in both alcoholic and aqueous media. Such epitaxial crystallisation in water represents a critical advance in the preparation of precision nanostructures and is crucial to their translation into biological fields, for example, within tissue engineering and drug delivery applications.

### *6.2.2 The importance of nanoparticle shape*

Given the spherical, cylindrical and platelet morphologies at hand, several studies into particle shape of these nanoparticles have been considered in detail, including their influence in hydrogel nanocomposites and Pickering emulsifiers.

The shape of nanoparticles has been shown to play a key role in the definition of the resultant properties of calcium-alginate hydrogels as well as in the strength of adhesion when the nanoparticles solutions are used as a glue. Hydrogels with platelet-shaped nanocomposites showed an enhanced resistance to breaking under strain in comparison to those with spherical nanocomposites, increasing the strength of the gels whilst maintaining self-healing behaviour. Platelet morphologies were also shown to provide improved adhesive properties over spherical constructs, suggesting the attractive possibility of improving calcium-alginate hydrogel performance both *in vivo* and also of adopting them as a method for self-repairing adhesive joints.

Similar platelets were also considered as Pickering emulsifiers in comparison to conventionally used spherical particles. Indeed, it was shown that the high surface area of platelet morphologies, when using the same weight percentage of emulsifier, allows for much improved stabilisation of water-water interfaces.

### 6.2.3 *The importance of nanoparticle size*

The greatest improvement over water-water interfacial stabilisation was achieved using platelet nanoparticles of a greater size, suggesting both shape and size as key attributes for such applications.

Indeed, it was proposed that the improved stabilisation of water-in-water emulsions was due to the large surface area of the platelets which exhibits greater adsorption properties and a larger barrier towards rotation of such large particles. This emulsion stability trend was observed across a range of coronal chemistries, highlighting both size and shape for the design of effective interfacial stabilizers.

Nanoparticle size was also considered extensively for PCL block copolymers in the preparation of cylindrical micelles of controlled length through an epitaxial growth mechanism. It was also shown that epitaxial growth to prepare cylinders of extended length resulted in the formation of biocompatible hydrogel materials.

## *6.3 Outlook*

As the most prominent theme of this work, crystallisation-driven self-assembly of amphiphilic block copolymers has been investigated for the formation of controlled 1D cylindrical and 2D platelet morphologies. In particular, given the high interest in 2D inorganic materials, the ability to readily access and control the assembly of polymers into 2D organic platelets through a simple assembly process provides a platform to develop a range of new materials. Further research, especially for poly(L-lactide) block copolymers, will investigate an epitaxial growth mechanism to allow for greater control over their dimensions. This approach should allow for the growth of polymer nanostructures without the increase in temperature required in the self-nucleation step. Further investigations into solvent composition and/or temperature to allow this epitaxial growth process to occur will be needed.

It is also expected that future work in this area of research will target a third dimension, allowing for orthogonal growth of polymer nanostructures to create even more complex functional materials. Such an approach will allow not only the length and width of particles to be controlled, but also the height of the corona layer. Potential research in this area may seek to exploit the presence of the chain transfer agent at the terminus of the polymer corona chains which have the ability to polymerise further after formation of the crystalline nanostructures. It is predicted that mild conditions will be required so as to allow polymerisation without any adverse effects on the crystalline structure. The presence of the chain transfer agent may also be utilised as a handle to functionalise the nanoobjects for further application.

Finally, an underlying theme of this work is the use of biocompatible materials, in particular, poly(L-lactide), poly(ε-caprolactone) and alginate hydrogels, which have been targeted due to their significant potential for use in a wide range of biorelevant applications including tissue engineering and drug delivery. Despite this, biocompatibility studies have not been considered to a great extent in this work, and so further studies with such polymers must monitor their compatibility for future use in biorelevant applications.